Homogeneous and Heterogeneous Resonators in Ultrahigh-Field MRI

Von der Fakultät für Ingenieurwissenschaften
Abteilung Elektrotechnik und Informationstechnik
der Universität Duisburg-Essen

zur Erlangung des akademischen Grades

Doktor der Ingenieurwissenschaften

genehmigte Dissertation

von

Kyoung-Nam Kim, M.Sc.
aus
Hongseong-gun, Chungcheongnam-do, Süd-Korea

1. Gutachter: Prof. Dr.-Ing. Klaus Solbach
2. Gutachter: Prof. Dr. rer. nat. Dr. med. Johannes Bernarding
Tag der mündlichen Prüfung: 07.11.2011

To my mother, my wife (Myungjin), and my children (Taeyun and Dohyun)

Table of Contents

Table of Contents 2

Acknowledgments 5

Abstract 6

Kurzfassung 7

List of Abbreviations 8

List of Symbols 10

List of Figures 13

1 INTRODUCTION 16
1.1 Objectives 16
1.2 Organization of the Thesis 19

2 BACKGROUND 20
2.1 Nuclear Magnetic Resonance (NMR) Basics 20
2.1.1 Angular Momentum of the Proton Spin 20
2.1.2 Magnetization Vector 21
2.1.3 External Magnetic Fields 22
2.1.4 Spin-Lattice and Spin-Spin Relaxation 23
2.1.5 Bloch Equation 25
2.1.6 Signal Excitation and Detection 25
2.2 Basic Electromagnetic Theory 26
2.2.1 Maxwell's Equations 26
2.2.2 Faraday's Law of Induction 27
2.2.3 Biot–Savart Law 28
2.2.4 Polarization 29
2.3 Basic Radiofrequency (RF) Coils 30
2.3.1 RF Transmit and Receive Coils 30
2.3.2 Homogeneous Resonators 31
2.3.2.1 Saddle-Shaped Resonator 31
2.3.2.2 Alderman–Grant Resonator 31
2.3.2.3 Birdcage Resonator 32
2.3.2.4 Transmission Line Resonator 33
2.3.3 Heterogeneous Resonators 35
2.3.3.1 Basic Surface Coil 35

2.3.3.2 Phased Array Coil 36

3 7 T SINGLE-CHANNEL TX/RX COILS 38
3.1 Motivation 38
3.2 Material and Methods 39
3.2.1 System Hardware 39
3.2.2 Design of Circular Polarized RF Coils 40
3.2.3 Quadrature Hybrid Coupler and PIN Diode Switches 42
3.2.4 Phantom Studies 45
3.2.4.1 SNR Maps 45
3.2.4.2 Mean SNR Measurement 46
3.2.4.3 Signal Homogeneity 46
3.2.4.4 Maps of Effective Flip Angle 46
3.2.4.5 Measurement of Averaged Effective Flip Angle Value 47
3.2.5 Human Brain Studies 48
3.2.5.1 Image Localization 48
3.2.5.2 Signal Intensity Profiles 49
3.2.5.3 Mean SNR Measurement 49
3.3 Results 50
3.3.1 Electrical Characteristics 50
3.3.1.1 Circular Polarized Volume Coils 50
3.3.1.2 Tx/Rx switches and Quadrature Hybrid Coupler 51
3.3.2 SNR Maps 52
3.3.3 Mean SNR Measurement 54
3.3.4 Signal Intensity Profiles 54
3.3.5 Signal Homogeneity in Two-Dimensional Image 56
3.3.6 Maps of Effective Flip Angle 57
3.3.7 Measurement of Averaged Effective Flip Angle Value 58

4 7 T MULTI-CHANNEL TRANSMIT ARRAYS 60
4.1 Motivation 60
4.2 Material and Methods 61
4.2.1 Performance of the Parallel Transmit using FDTD Simulations 61
4.2.2 System Hardware 64
4.2.2.1 Configuration of Parallel Transmit System 64
4.2.2.3 Variable Power Combiner using Butler Matrices 65
4.2.3 Geometry Modeling and Magnetic Field Simulation 66
4.2.3.1 Eight-Element Array using the Biot–Savart approach 66
4.2.3.2 EM Simulation using CST MWS 68
4.2.4 SAR Calculation using CST MWS 69
4.2.5 Design of RF Coils and Circuitry 70
4.2.5.1 Multi-channel Tx Arrays 70
4.2.5.2 Design of Power Divider, T/R Switches, and Phase Shifter 71

4.2.6 Phantom Studies 76
4.2.6.1 Maps of Effective Flip Angle 77
4.2.6.2 SNR Maps and Mean SNR measurement 78
4.2.6.3 Signal Intensity Profiles 78
4.3 Results 79
4.3.1 Simulation of Magnetic Field 79
4.3.1.1 Magnetic Field Creation Using Biot–Savart's Law 81
4.3.1.2 EM Simulation using CST MWS 83
4.3.1.3 SAR Calculation using CST MWS 85
4.3.2 Electrical Characteristics 85
4.3.2.1 Multiple Transmit Coil Arrays 85
4.3.2.2 RF Circuitry for Transmit Coil Arrays 86
4.3.3 Assembled RF Coil and Circuitry 90
4.3.4 Maps of Effective Flip Angle 92
4.3.5 SNR Maps 95
4.3.6 Signal Intensity Profiles 96
4.3.7 Mean SNR Measurement and Specific Ratio 97

5 CONCLUSIONS AND FUTURE WORK 98
5.1 Conclusion and Discussion 98
5.1.1 7 T Single-channel Tx/Rx Coils 98
5.1.2 7 T Multi-channel Transmit Array Coils 100
5.2 Suggestion for Future Work 101

Bibliography 102

Acknowledgments

Pursuing a Ph.D. project is often teamwork, and although it will not be enough to express my gratitude in mere words, I want to express my thanks to all the people who have helped me.

First, I give my sincere thanks to my esteemed supervisor, Prof. Dr. rer. nat. Dr. med. Johannes Bernarding, the head of the Department of Biometry and Medical Informatics, Otto-von-Guericke-University of Magdeburg. His steady understanding, encouragement, and personal guidance helped to finish the present thesis.

I also express my deep appreciation to Prof. Dr. Zang-Hee Cho, the director of the Neuroscience Research Institute (NRI) at Gachon University of Medicine and Sciences, Korea. He accepted me as his research assistant at NRI, and during that period he offered me a great deal of advice, was a patient supervisor, and always guided me in the right direction. During this work, the basis of the present dissertation was set.

Special thanks are also given to Dipl.-Ing. Tim Herrmann for his steady valuable advice and friendly help. I am also very grateful to Dipl.-Ing. Johannes Mallow for his essential assistance, the constructive criticism, and his excellent advice for the electromagnetic field simulation of this study. The discussions in the group and the support in the experiments have been very helpful for this study.

I would also like to thank Prof. Dr.-Ing. Klaus Solbach from the Faculty of Engineering (University Duisburg-Essen) for constructive discussions and the help in finishing the Dissertation. I also acknowledge the support from the 7T teams in Magdeburg (Dr. Jörg Stadler) and Essen (Dr. Andreas Bitz) that allowed the successful evaluation of the RF coils.

I am very grateful to my mother. Her firm and kindhearted personality gave me the strength to be steadfast and never bend to difficulties. Last but not least, I am greatly indebted to my devoted wife Myungjin and my two sons Taeyun and Dohyun. Their love and support without any complaint or regret let me complete this work.

The financial support of the Otto-von-Guericke-University of Magdeburg, the Gachon university of medical and science and the German Ministry of Research (BMBF) are gratefully acknowledged.

Magdeburg, Germany Kyoung-Nam, Kim

17.06.2011

Abstract

The main objective of this study was to construct, to improve and to evaluate the performance of different radiofrequency (RF) coils for ultrahigh-field (UHF) at 7T magnetic resonance imaging (MRI) with respect to signal-to-noise ratio (SNR), B_1 homogeneity, and effective flip angle (FA) maps. Best magnetic resonance (MR) images are obtained if RF coils fulfill the two fundamental requirements: the B_1 field in the excited volume respective region of interest (ROI) has to be homogeneous while the received SNR has to be as high as possible. However, the major problems associated at UHF conditions are amplified imaging artifacts, the shortened transversal relaxation times of tissue, the inhomogeneous B_1 field in the ROI, and the increased absorption of RF energy. Although all RF coils in UHF MRI intrinsically generate inhomogeneous B_1 fields due to the dielectric effect rather than the RF coil geometry, each RF coil may exhibit special characteristics, which makes them optimized for special MRI applications. They should therefore be designed according to the desired field of operation to obtain optimal performance MRI.

The developed UHF RF coils were categorized according to their architecture, i.e., into homogeneous and heterogeneous coils. Four homogeneous transmit/receive (Tx/Rx) circular polarized (CP) volume coils - hybrid birdcage (HBC), hybrid spiral birdcage (HSBC), dual Helmholtz (DH), and slotted tube (ST) - were constructed, compared and evaluated at a magnetic field strength of 7T. An evaluation procedure for comparing the B_1 field inhomogeneity and SNR is proposed. In particular, B_1 excitation inhomogeneity has to be considered and compared between the different RF coils to improve the differences in the contrast and the spatially varying image signal in the ROI.

Heterogeneous coils such as surface coils are usually much smaller than homogeneous coils. They are located nearer the object and hence usually have higher SNR because they receive higher signal from the ROI. However, they have a relatively poor B_1 field homogeneity, and thus, they are mainly utilized as Rx-only coils. In an additional stage, a 16 element parallel Tx (pTx) coil was designed, constructed and evaluated for use as a head-array. The RF coil was connected to a 16 × 16 Butler matrix network operated by an eight-channel parallel Tx system to investigate the improvement of the B_1 excitation. The transmit profiles were evaluated for various clockwise CP modes with respect to homogeneity. Compared to the CP coil architectures the 16 element pTx coil provides much more potential to improve excitation characteristics.

Kurzfassung

Das Hauptziel dieser Arbeit war die Konstruktion, Evaluierung und Verbesserung verschiedener Hochfrequenz (HF) Spulen für Ultra-Hochfeld (UHF) Magnetresonanztomographie (MRT) bei 7T unter Berücksichtigung des Signal-zu-Rauschabstands (SNR), der B_1 Homogenität und des effektiven Flip-Winkels (FA). Die besten MR-Bilder erhält man, wenn zwei fundamentale Bedingungen erfüllt sind: das B_1 Feld im angeregten Volumen bzw. im betrachteten Bereich (ROI) sollte möglichst homogen und die SNR im Empfangsfall möglichst hoch sein. Dennoch kommt es unter Hochfeld-Bedingungen oft zu verstärkten Bildartefakten durch verkürzte transversale Relaxationszeiten im Gewebe, B_1-Feldinhomogenitäten in der ROI und einer erhöhten Energieabsorption im untersuchten Objekt. Obwohl alle HF-Spulen eher durch dielektrische Effekte als durch die Spulengeometrie ein inhomogenes B_1-Feld generieren, kann jede Spule spezielle Charakteristiken aufweisen, so dass sie für spezielle Anwendungen optimiert werden kann. Um die gewünschte Feldverteilung zu erhalten, sollte das Design der Spule entsprechend angepasst werden. Die entwickelten UHF HF Spulen unterscheidet man nach homogenen und heterogenen Spulentypen. Es wurden 4 zirkular polarisierte Sende/Empfangsspulen - Hybrid Birdcage (HBC), Hybrid spiral Birdcage (HSBC), dual Helmholtz (DH) und slotted tube (ST) - konstruiert, verglichen und mit Hilfe eines 7T MRT-Systems evaluiert. Für den Vergleich verschiedener Spulen hinsichtlich SNR und B_1-Feld wird in dieser Arbeit ein Konzept vorgeschlagen. Für den Vergleich und zur Verbesserung der Kontrastdifferenzen und des örtlich variierenden Bildsignals müssen insbesondere die B_1-Feldinhomogenitäten betrachtet und für die verschiedenen Spulen verglichen werden.

Heterogene Spulen wie Oberflächenspulen sind gewöhnlich deutlich kleiner als homogene Spulen und sind nahe am Objekt lokalisiert. Daher haben sie in der Regel ein höheres SNR. Andererseits haben sie eine relativ schlechte B_1-Feldhomogenität und werden daher in der Regel als reine Empfangsspulen genutzt. In einem weiteren Abschnitt wurde eine 16 Element Parallel-Transmit (pTx) Spule entwickelt, gebaut und evaluiert, mit der Zielstellung, sie als Kopfspule einzusetzen. Die Spule wurde mittels einer 16 × 16 Butler-Matrix an ein 8 Kanal Parallel-Transmit-System angeschlossen, um die Butler-Matrix anzusteuern und die Optimierung der B_1 Anregung zu untersuchen. Die Transmit Profile wurden evaluiert für verschiedene CP Moden im Uhrzeigersinn hinsichtlich ihrer Homogenität. Verglichen mit der CP Spulenarchitektur besitzt die 16-Element-pTx-Spule ein höheres Potential bei der Verbesserung der Anregungscharakteristik.

List of Abbreviations

Abbreviation	Meaning
Radio Frequency	RF
Ultrahigh-Field	UHF
Signal-to-Noise Ratio	SNR
Flip Angle	FA
Region of Interest	ROI
Magnetic Resonance Imaging	MRI
Transmit/Receive	Tx/Rx
Circular Polarization	CP
Hybrid Birdcage	HBC
Hybrid Spiral Birdcage	HSBC
Dual Helmholtz	DH
Slotted Tube	ST
Parallel Transmit	pTx
Nuclear Magnetic Resonance	NMR
High-Field	HF
Blood Oxygenation Level Dependent	BOLD
Free Induction Decay	FID
Functional Magnetic Resonance Imaging	fMRI
Parallel Imaging	PI
Transverse Electromagnetic	TEM
Standard Deviation	SD
Electromotive Force	EMF
Field of View	FOV
Analog to Digital Converter	ADC
End-Ring	ER
Alternating Current	AC
Direct Current	DC
Band-Rejection Filter	BRF
Low-Pass Filter	LPF

Gradient Recalled Echo	GRE
Repetition Time	TR
Echo Time	TE
Signal Intensity	SI
National Electrical Manufactures Association	NEMA
Stimulated Echo	STE
Spin Echo	SE
Magnetization Prepared Rapid Acquisition	MPRAGE
Inversion Time	TI
Anterior Commissure	AC
Posterior Commissure	PC
Left-Right	L-R
Superior-Inferior	S-I
Short Open Load Through	SOLT
Anterior-Posterior	A-P
Linear Polarized	LP
Sensitivity Encoding	SENSE
Specific Absorption Ratio	SAR
Electromagnetic	EM
Finite Difference Time Domain	FDTD
Perfectly Matched Layer	PML
Computer Simulation Technology Microwave Studio	CST MWS
Food and Drug Administration	FDA
Continuous Waveform	CW
Velocity Factor	VF
Actual Flip Angle Imaging	AFI
Fast Low Angle Shot	FLASH
Vector Network Analyzer	N.A.
Arbitrary Unit	a.u.

List of Symbols

Symbol	Meaning
$\vec{B}_0$	Main Magnetic Field
$\vec{B}_1$	Magnetic Field by RF Coil
$\vec{\mu}$	Magnetic Moment Vector
ω_0	Angular Frequency
γ	Gyromagnetic Ratio
I_s	Spin Quantum Number
$\vec{J}$	Angular Momentum Vector
$\hbar$	Planck's Constant
$\vec{M}$	Magnetization
$\vec{M}_0$	Equilibrium Magnetization
M_p	Parallel Magnetization Component
M_t	Transverse Magnetization Component
M_z	Longitudinal Magnetization
M_{xy}	Transverse Magnetization
T_1	Spin-Lattice Relaxation Time
T_2	Spin-Spin Relaxation Time
$B_{1m}(t)$	Modulated Sinusoidal B_1 Signal
ω_c	Carrier Frequency of the RF Pulse
φ	Initial phase angle
$B_1^+(t)$	Clockwise Rotating B_1 Field
$B_1^-(t)$	Counterclockwise Rotating B_1 Field
Φ_c	Magnetic Flux through the RF Coil
$\vec{E}$	Electric Field Intensity

$\vec{H}$	Magnetic Field Intensity
$\vec{D}$	Electric Flux Density
$\vec{B}$	Magnetic Flux Density
ρ	Volume Charge Density
J	Electric Current Density
ε_0	Permittivity in the Vacuum
μ_0	Permeability in the Vacuum
ε_r	Relative Permittivity
$\rho^{'}$	Mass Density
Φ_s	Magnetic Flux through a Surface
I	Current
ϕ	Phase
ϕ_r	Relative Phase Angle
α	Flip Angle
τ	Time Duration of the Applied RF pulse
T	Temperature
Δf	Frequency Bandwidth
ΔD	Duty cycle
Z_0	Characteristic Impedance
Z_{in}	Input Impedance
Z_{out}	Output Impedance
ϕ_c	Angle between two conductor of RF Coil
ω_r	Resonant Frequency
β	Propagation Constant
Γ	Reflection Coefficient
σ	Conductivity
α_{eff}	Effective Flip Angle
α_{giv}	Given Flip Angle

L	Inductance
R	Resistance
C	Capacitance

List of Figures

Figure 2.1: Nuclei with nonzero magnetic dipole moment in microscopic magnets ...20
Figure 2.2: Distribution of nuclear magnetic moments by T_1 relaxation 22
Figure 2.3: Distribution of nuclear magnetic moments by T_2 relaxation 22
Figure 2.4: Relaxation curves of longitudinal magnetization 23
Figure 2.5: Relaxation curves of transverse magnetization 24
Figure 2.6: Closed contour and surface related to Faraday's law 27
Figure 2.7: Cylindrical coordinates for a single loop of wire along the z-axis 28
Figure 2.8: Coordinates of polarization 29
Figure 2.9: Geometry of the saddle coil 31
Figure 2.10: Current distribution of the Alderman–Grant resonator 32
Figure 2.11: Spatial representation of a low-pass 16-leg birdcage coil 32
Figure 2.12: Comparison of transmission line and lumped element circuit 33
Figure 2.13: Circuit models for TEM coil 34
Figure 2.14: Geometry of the basic surface coil 35
Figure 2.15: Normalized relative positioning of (a) circular and (b) square loops for reducing the mutual inductance 36
Figure 2.16: Isolation preamplifiers for reducing the mutual inductance 37
Figure 3.1: Pictorial representation of circular polarized volume coils 38
Figure 3.2: Block diagram of MRI system with 40
Figure 3.3: Geometry of the (a) DH coil is comprised of (b, c) two orthogonal Helmholtz coils 41
Figure 3.4: Quadrature driving mechanism 42
Figure 3.5: Basic circuit modeling of (a) Tx/Rx switches and (b) quadrature hybrid coupler 42
Figure 3.6: Circuit modeling of Tx/Rx switches and quadrature hybrid coupler 43
Figure 3.7: S-parameter of combined Tx/Rx switches and quadrature hybrid coupler .44
Figure 3.8: Plastic cylinder phantom (distilled water) 45
Figure 3.9: ROI definition for the mean SNR measurement in the phantom 46
Figure 3.10: Four different ROI (i–iv) for measuring the averaged FA value 48
Figure 3.11: ROI definition for the mean SNR measurement in the human brain 49
Figure 3.12: Four designed circular polarized volume coils 50

Figure 3.13: Reflection coefficient for each circular polarized volume coil 51
Figure 3.14: Designed Tx/Rx switches and quadrature hybrid coupler 52
Figure 3.15: SNR distribution of 16 cm diameter water cylinder phantom GRE images for four CP coils 53
Figure 3.16: SNR distributions of the human brain GRE images for four CP coils 53
Figure 3.17: B_1 signal intensity profiles of human brain for four CP volume coils 55
Figure 3.18: Relative ratio to the HBC coil for signal intensity 56
Figure 3.19: Effective FA maps for the α_{giv} (= 50°) in the (i) phantom and (ii) human brain 58
Figure 4.1: Eight-element transmit array modeled with FDTD 62
Figure 4.2: B_1 field distribution according to errors in amplitude and phase excitation of eight-element transmit array 63
Figure 4.3: Configuration of the multi-channel parallel RF transmit system 64
Figure 4.4: 16 × 16 Butler matrix for a 16-element transmit array 65
Figure 4.5: Block diagram of 8 × 8 and 16 × 16 Butler matrices for a 16-element Array 65
Figure 4.6: Single element coil consisting of 16-point functions 66
Figure 4.7: Top view of the counterclockwise eight-element transmit array 67
Figure 4.8: Geometric models of the (a) eight-element and (b) 16-element transmit arrays with CST MWS 68
Figure 4.9: Configuration of RF receive system 70
Figure 4.10: Capacitance of transmit arrays at 297.2 MHz 71
Figure 4.11: Schematic circuit of the Wilkinson power divider 72
Figure 4.12: Lumped element version of the Wilkinson power divider for circuit simulation 72
Figure 4.13: Frequency response of an equal-split Wilkinson power divider 73
Figure 4.14: RF and DC signal pathways of the Tx/Rx switching circuit 74
Figure 4.15: Phase difference through an external cable length 75
Figure 4.16: Different cable lengths of eight-element transmit array coil for CP mode..76
Figure 4.17: Spherical phantoms: (a) oil, (b) water, and (c) mixed sugar and water 76
Figure 4.18: Timing diagram of the AFI sequence 77
Figure 4.19: Individual B_1 field pattern of the eight-element transmit array 79
Figure 4.20: B_1 field pattern of a single element (No.1) 80
Figure 4.21: (a) Combined B_1 field distribution and (b) SI profiles of the eight-element

transmit array 80
Figure 4.22: B_1 field distribution according to variable horizontal length of 10-100 mm for single element (No.1) 81
Figure 4.23: SI profiles according to variable width for a single element 81
Figure 4.24: B_1 field distribution according to variable width of the element 82
Figure 4.25: (a) maximum value and SD value and (b) mean value and SD value of B_1 field created by variable horizontal width 83
Figure 4.26: Recalculated central axial B_1^+ maps of (a) 8-elemet and (b) 16-element transmit array 84
Figure 4.27: SAR distributions using transmit head-array coils 85
Figure 4.28: Geometry of transmit head-array coils 86
Figure 4.29: Image of the Wilkinson power splitter 86
Figure 4.30: Image of the lumped element Tx/Rx switches 87
Figure 4.31: Phase difference according to different lengths of the cable 89
Figure 4.32: Schematics of RF excitation with dedicated eight-driven pTx system for (a) eight-element and (b)16-element transmit head-arrays 90
Figure 4.33: RF circuitry for (a) eight-element and (b) 16-element transmit head arrays and enlarged parts of (b) are shown in the lower row 91
Figure 4.34: Sixteen individual FA maps for an oil phantom 92
Figure 4.35: Eight individual FA maps of oil phantom from the combined excitation of two elements using a 16-element transmit array 93
Figure 4.36: Combined FA maps of (a) 16-element transmit array, (b) eight-combined elements transmit array, (c) eight-element transmit array in the oil phantom 93
Figure 4.37: Sixteen individual FA maps of the water phantom 94
Figure 4.38: Combined FA maps of (a) 16-element transmit array, (b) eight-combined elements transmit array, (c) eight-element transmit array in the oil phantom 94
Figure 4.39: (a) GRE image and (b) FA maps for clockwise CP modes 95
Figure 4.40: FA measurement for clockwise CP modes 96
Figure 4.41: Signal Intensity Profiles for clockwise CP modes 96

1 INTRODUCTION

1.1 Objectives

MRI systems are widely used in medical diagnosis due to their ability to produce cross-sectional and three dimensional anatomic images in any direction in a nonhazardous method [1-5]. The MRI technique is based on the difference in relaxation times T_1 and T_2 not only between different tissues but also between normal and cancerous tissue [6, 7]. Due to a broad range of tissue properties, MRI is at the forefront of medical imaging systems [8]. Recently there is a trend towards ultrahigh-field MRI (7 T and higher) to increase the SNR and enhance the susceptibility contrast (e.g. T_2^* blood oxygenation level dependent (BOLD) MRI in functional imaging) [9-11]. The T_2^*-weighted imaging is sensitive to susceptibility effects caused by deoxyhemoglobin, iron concentration, and tissue microstructure [12]. On the other hand, increasing B_0 also raises specific problems such as increased RF energy absorption in the tissue, increased B_1 inhomogeneity generated by dielectric focusing effects [13, 14], and shortened T_2 relaxation in tissue.

In MRI, RF resonators are necessary for transmitting the RF signal to the sample and receiving the free induction decay (FID) signal from the sample. RF coils must have high sensitivity in the receiving mode and homogeneous transmit B_1 (B_1^+) in the volume of interest during the transmitting mode. Particularly, high B_1 sensitivity is required because the SNR of the MR image is directly related to the sensitivity of the RF coil. In standard clinical systems operating at 1.5T and 3T the RF coils most commonly used are variant types of the birdcage structure [15] and multiple-element Rx-only array [16]. Although gradient modes enable to improve the sensitivity in peripheral regions of the sample [17], imaging techniques using uniform modes in the birdcage configuration are favored for medical diagnostics field due to its widely uniform B_1 field distribution [18]. The multiple-element receive-only array and modifications are generally used for spine, cardiac, and whole-body imaging as well as specialized applications in brain imaging [19-22]. However, there are several challenges for RF coils in UHF MRI systems with frequencies of 300 MHz or higher used for brain imaging. Firstly, the inductance of the RF coil is constrained by the size of the human head [18]. Secondly, the amount of power loss increases with increasing frequency [23]. Lastly, radiation losses increase in proportion to the fourth power of the frequency and to the square of the RF coil area [24]. This is due to the phenomenon where the effective RF wavelength is shortened

by the permittivity of the sample positioned at the interior of the RF coil [25]. The shortened wavelength results in standing waves [26] inside the sample. As a result, using CP volume coils leads to an inhomogeneous B_1 field where the periphery of the image becomes hypo-intense while the center part of the image gets hyper-intense [27].

UHF RF coil design for brain imaging became feasible in recent years. Mostly, three major routes for RF coils are being pursued today. In older single-channel RF amplifier systems, single-channel transmit/receive (Tx/Rx) birdcage-based configurations are being utilized and developed for volume coverage of the human brain [28, 29]. Under the same operating system, multiple-element Rx-only array coils are also continually being developed due to the availability of multiple receiver channels [30, 31]. In driven multi-channel RF amplifier systems (i.e. parallel transmit (pTx) system [32]), transmit coil arrays techniques are proceeded steadily for substantially improving the B_1^+ homogeneity of MR instruments [33]. The main goal of this study was optimizing RF coil geometry to reach higher reception sensitivity and higher B_1 field homogeneity; in particular, B_1^+ homogeneity. Commonly used single-channel Tx/Rx circular polarized (CP) coils working as a homogeneous resonator in the UHF intrinsically generate inhomogeneous B_1 fields rather due to the dielectric effect [34, 35] than due to the RF coil geometry. There are differences in RF coil's performance between different RF coil architectures. Therefore, to decide which coil might be optimal for which application particular for brain imaging, more experimental data have to be provided. To compare the performance of CP volume coils, four types - HBC [15], HSBC [36], DH - based saddle coil [37], and ST - based Alderman-Grant coil [38] - were designed under the same dimensions and compared at a magnetic field strength of 7T in terms of SNR, signal homogeneity, and maps of effective flip angle (FA) in water phantom and *in-vivo* brain .

However, multiple-element arrays have many advantages. Besides high receive sensitivity and scan time reduction through reconstruction techniques [39-41], the robust software algorithms for parallel reconstruction methods offer fast MR imaging by reducing a part of the time consuming spatial phase encoding [42]. Coil arrays are often used for research applications in functional MRI (fMRI) and other head-related studies. However, whole brain imaging applications using multiple arrays in UHF are very limited; this is mainly due to the fact that these research systems currently do not have local whole body coils or detunable Tx-only coils. Many studies have been performed using multiple receive-only arrays with various kinds of complicated geometries [43-45] to obtain high B_1 receive sensitivity in the ROI. pTx systems are the latest development for optimizing 7T MRI. They allow transmitting multiple independent and simultaneous excitation pulses which improves B_1^+ homogeneity [46]

together with enhanced B_1 reception sensitivity and parallel imaging (PI) performance [33]. However, significant challenges in UHF still remain with regard to the design and implementation of RF coils for dedicated transmit channels and their integration into existing pTx systems [47]. Furthermore, increasing the number of array elements [48] has been suggested to achieve homogeneous B_1 transmit and high B_1 reception sensitivity. Most transmit head-arrays at 7T were basically designed [49] as eight separate channels for transmission and reception using variant cylindrical geometry. In addition, strip-line [50-52] or hybrid transverse electromagnetic (TEM) and loop elements [53] were used in the coil structure. However, the biggest benefit of loop elements is the ability to minimize inductive interactions between elements. The presented study wanted to focus on this fact: designing and constructing a 16-element transmit head-array with lumped element component and to evaluate the RF coil in terms of SNR and effective FA under the condition of a maximum of eight-channel pTx. The coil was aimed to work as a Tx/Rx head-array for a 7T MRI system. In order to access different CP modes simultaneously, Butler matrix networks designed and manufactured by the group of Solbach et al. [54] should be used for excitation of the most important phase modes of the coil array. Another goal was to examine which and how much modes would be most useful. It was hypothized that using the CP^{+}_{1} (first-order clockwise CP) mode as the dominant mode would be necessary to get a homogeneous image; the remaining other CP modes might be less important [55, 56]. For comparison the transmit profiles and specific ratio using mean value and standard deviation (SD) had to be used to evaluate the homogeneity and sensitivity. The 16-element transmit head-array coil was connected to a 16 x 16 Butler matrix and an eight-channel pre-power combiner and hence operated by an eight-channel pTx system to excite the coil array in a 7T whole-body MRI system

In summary, the study had the following goals:

- Designing, constructing and evaluating four CP volume coils
    - Hybrid birdcage coil (HBC),
    - Hybrid spiral birdcage coil (HSBC)
    - Dual Helmholtz (DH) - based saddle coil
    - Slotted tube (ST) - based Alderman-Grant coil
- Designing, constructing and evaluating parallel transmit coils
    - 8 element transmit coil array
    - 16 element transmit coil array
- Developing the evaluation procedure

Since at the beginning of the study only few 7T RF coils were available that usually had very

restricted imaging qualities, this Dissertation wants to provide a significant progress towards optimized 7T imaging.

1.2 Organization of the Thesis

To provide an understanding of the basic background of MRI, the basics of electromagnetic theory and a concise foundation for the physics of NMR and MRI technology are presented in Chapter 2.1. The incorporation of both the classical Bloch equation and signal excitation and detection is explained through nuclear magnetization. The basic electromagnetic theory is introduced in Chapter 2.2. Chapter 2.2 describes the fundamental basic equations utilized for better understanding of the RF coil. The general principles of the properties of homogeneous and heterogeneous resonators are introduced together with the equivalent circuit and magnetic field in Chapter 2.3. A connection between the presented MRI theory and RF coil design is introduced in chapter 2. As described in Chapter 3, the CP volume coils for HBC, HSBC, DH, and ST coils were experimentally compared at a magnetic field strength of 7T. This was accomplished in a phantom and *in vivo* brain through a comparison of B_1 field homogeneity, B_1^+ homogeneity, and SNR for the same dimensions from the sets of data. Experimental images were obtained by using the developed quadrature hybrid coupler and output of a single-channel RF Tx system. This research was performed in the Neuroscience Research Institute (NRI), Korea and supported by the Bio R&D program through the Korea Science and Engineering Foundation funded by the Ministry of Education, Science and Technology (M10530010001-06N3001-00110). Chapter 4 covers the design for the 16-element transmit coil arrays, which were processed and evaluated in terms of FA distribution, SNR maps, and signal homogeneity. In particular, transmit profiles and specific ratios using the mean signal and SD value were compared. Simulations were performed through the Biot–Savart approximation and CST MWS, and experimental data were obtained with an eight-drive pTx system at 7T. This was compared with an eight-channel standard head-array with the same phantom. The different SNR maps of several clockwise CP modes and FA inhomogeneities were obtained from an additional 16 × 16 channel Butler matrix network and 8 × 8 pre-power combiner. This work was performed at Otto-von-Guericke-University Magdeburg and supported by a grant from Saxony-Anhalt (PJ-Nr. 507 and supported code: 3802208, Germany) and the Federal Ministry of Education and Research. Finally, Chapter 5 presents the conclusions that can be drawn from this study.

2 BACKGROUND

2.1 Nuclear Magnetic Resonance (NMR) Basics

2.1.1 Angular Momentum of the Proton Spin

The nuclear magnetic dipole moment $\vec{\mu}$ is represented by vector quantity [58], as shown in Figure 2.1.

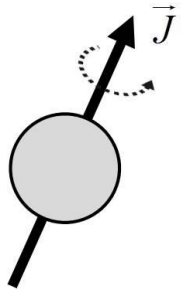

Figure 2.1: Nucleus with nonzero magnetic dipole moment in microscopic magnets

The nuclear magnetic moment $\vec{\mu}$ and spin angular momentum vector $\vec{J}$ are related, i.e.,

$$\vec{\mu} = \gamma \vec{J} \qquad [2.1]$$

where γ is the constant and called the gyromagnetic ratio. The γ depends on the nucleus and is 42.56 MHz/T for ^{1}H (Hydrogen) proton. The corresponding Larmor frequency ω_0 is approximately 297.2 MHz at 7T. The γ values for other nuclei are listed [58] in Table 2.1.

Table 2.1: Properties of NMR nuclei [58]

Nucleus	Spin	Relative Sensitivity	Gyromagnetic Ratio (MHz/T)
Hydrogen (^{1}H)	½	1.000	42.58
Fluorine (^{19}F)	½	0.870	40.05
Phosphorus (^{31}P)	½	0.093	11.26
Carbon (^{13}C)	½	0.016	10.71

The magnitude of $\vec{\mu}$ is represented by

$$\vec{\mu} = \gamma\hbar\sqrt{I_s(I_s+1)} \qquad [2.2]$$

where $\hbar$ is Planck's constant (6.6×10^{-34} Joule/sec) and I_s is the nuclear spin quantum number. The spin quantum number is 1/2 (= I_s) for ^{1}H, ^{13}C, ^{19}F, and ^{31}P nuclei and called a spin -1/2 system.

2.1.2 Magnetization Vector

The magnetization $\vec{M}$ is defined by parallel (M_p) and transverse (M_t) components through the external static magnetic flux density $\vec{B}_0$. Magnetization $\vec{M}$ is

$$\frac{d\vec{M}}{dt} = \gamma\vec{M}\times\vec{B}_0 \qquad [2.3]$$

where $\vec{M}$ is considered by protons as the $\vec{\mu}$ per unit volume (V) and defined by

$$\vec{M} = \frac{1}{V}\sum\vec{\mu}_i \qquad [2.4]$$

The M_p and M_t components of the $\vec{M}$ are $M_p = M_z$ and $\vec{M}_t = M_x x + M_y y$, respectively. The decoupled equations denoted as the cross product are given by

$$\begin{aligned}\frac{dM_z}{dt} &= 0,\\ \frac{d\vec{M}_t}{dt} &= \gamma\vec{M}_t\times\vec{B}_0\end{aligned} \qquad [2.5]$$

The difference in proton interaction depends on the decay parameter, which is related to the contrast in a given magnetic moment. The M_p and M_t components of $\vec{M}$ are due to different relaxations for the equilibrium state to the external $\vec{B}_0$.

2.1.3 External Magnetic Fields

When there is no external magnetic field, the net magnetization has the same direction as the B_0, and this is called equilibrium magnetization. However, under a static magnetic field, magnetization receives torque from the external field and nuclear precession at the Larmor frequency. If an excitation RF B_1 is applied at the Larmor frequency, magnetization is tipped down away from the z-direction to a certain degree. This is called the longitudinal magnetization M_z and is characterized by an exponential curve with time constant T_1 [59], as shown in Figure 2.2.

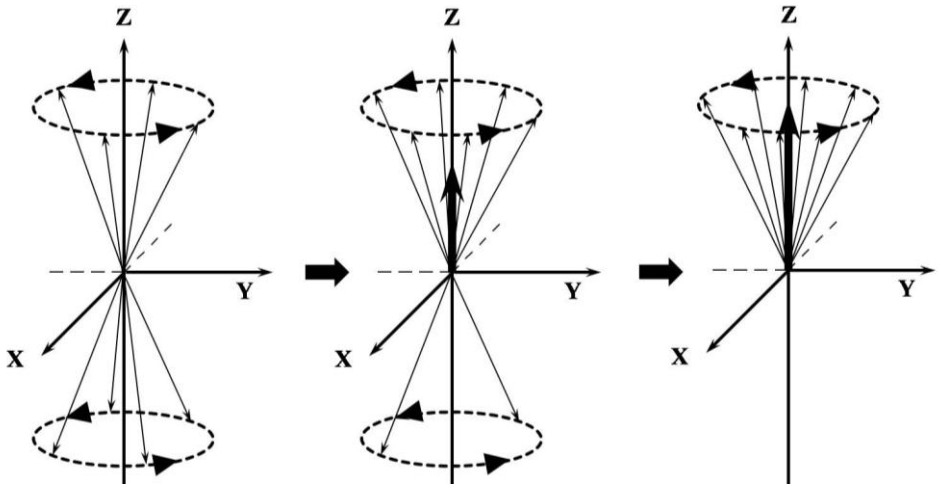

Figure 2.2: Distribution of nuclear magnetic moments by T_1 relaxation [59]

At the same time, the transverse magnetization M_t in the xy-plane (M_{xy}) decays by a constant T_2 [60], as shown in Figure 2.3.

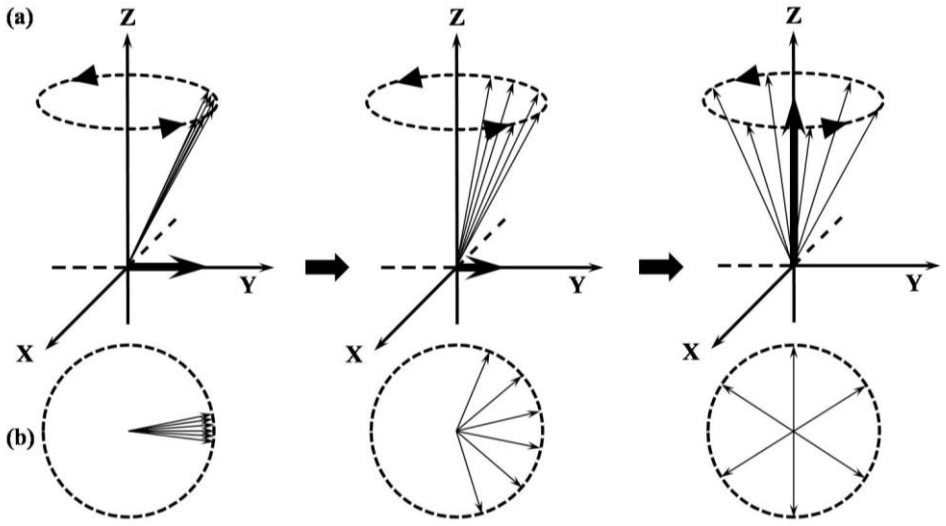

Figure 2.3: Distribution of nuclear magnetic moments by T_2 relaxation [60]

The spatial information of spatial resolution for subject was acquired through encoded techniques by Lauterbur et al. [4]. They introduced a new approach for gradient magnetic fields into the NMR and acquired MR images with small samples. The imaging techniques were based on back-projection methods. The next phase-encoding techniques using gradient magnetic techniques were introduced by Ernst et al. [61], who easily obtained MR images through Fourier transform.

2.1.4 Spin-Lattice and Spin-Spin Relaxation

The magnetization naturally tries to go into an equilibrium state; this phenomenon is called relaxation. The recovery along the longitudinal direction of magnetization according to equilibrium is called longitudinal relaxation, i.e., spin-lattice relaxation. Its behavior is defined by

$$\frac{dM_z}{dt} = -\frac{M_z - M_0}{T_1} \qquad [2.6]$$

This equation is solved by an exponential function

$$M_z(t) = M_0(1 - e^{-t/T_1}) \qquad [2.7]$$

where T_1 is the spin-lattice relaxation time constant of the sample. In general, T_1 is longer for high-strength magnetic fields compared to low fields. M_z takes a longer time [8] to perfectly recover until equilibrium. The behavior of longitudinal relaxation [62] is shown in Figure 2.4.

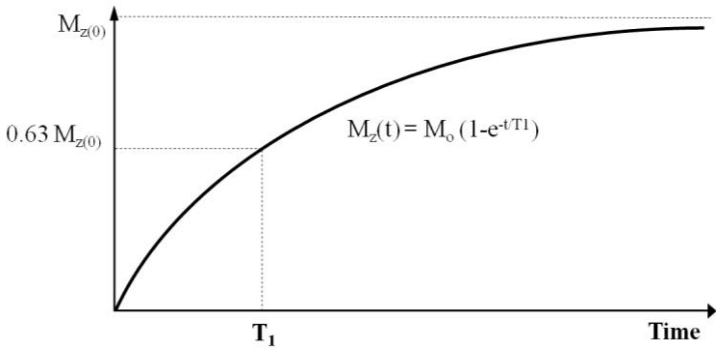

Figure 2.4: Relaxation curves of longitudinal magnetization [62]

The transverse magnetization also decays to zero with an exponential curve of T_2 at the same

time as longitudinal relaxation occurs. This is transverse or spin-spin relaxation. The behavior is described by

$$\frac{dM_{xy}}{dt} = -\frac{M_{xy}}{T_2} \qquad [2.8]$$

This is solved by an exponentially decaying function

$$M_{xy}(t) = M_0 e^{-t/T_2} \qquad [2.9]$$

The behavior of the decay of the transverse component [63] is shown in Figure 2.5

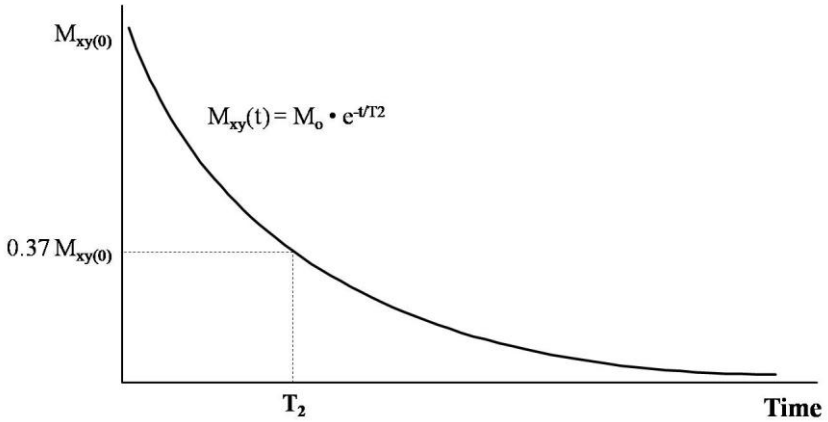

Figure 2.5: Relaxation curves of transverse magnetization [63]

where T_2 is the spin-spin time constant. In the MRI experiment, transverse magnetization is combined with both spin-spin interaction and B_0 inhomogeneity; as a result, a new combined time T_2^* was generated:

$$\frac{1}{T_2^*} = \frac{1}{T_2} + \frac{1}{T_2'} \qquad [2.10]$$

Pure T_2 decay is only a function of the complete interaction between spins and spins. T_2' is a factor for both B_0 inhomogeneity and subject dependence. The T_2^* will cause faster decaying signal intensity and affect image contrast

2.1.5 Bloch Equation

The behavior of magnetization $\overrightarrow{M}$ in the presence of an applied external static magnetic flux ($\vec{B}_0 = B_0\hat{z}$) is described by the Bloch equation [3]. It makes it easier to understand the behavior of nuclear magnetization. The general form is denoted as follows

$$\frac{d\overrightarrow{M}}{dt} = \gamma\overrightarrow{M} \times \vec{B}_0 + \frac{(M_0 - M_z)\hat{z}}{T_1} - \frac{(M_x\hat{x} - M_y\hat{y})}{T_2} \qquad [2.11]$$

The first term is the free precession without T_1 and T_2 effects. The next term is only the T_1 effect, and the last term is the T_2 effect. A simple equation is formed under the condition of no effect from T_1 and T_2.

$$\frac{d\overrightarrow{M}}{dt} = \gamma\overrightarrow{M} \times \vec{B}_0 \qquad [2.12]$$

This assumes that in terms of duration, the RF pulse is shorter than T_1 and T_2.

2.1.6 Signal Excitation and Detection

The excitation process establishes the phase coherence of magnetic moments. It is achieved by applying an external oscillating B_1 field to the spin system. B_1 is perpendicular to B_0 and rotated at an angular frequency. The $B_1(t)$ field can be rewritten through complex notation

$$\vec{B}_1(t) = \mathrm{Re}\left\{\vec{B}_{1m}(t)e^{-j(\omega_c t+\varphi)}\right\} \qquad [2.13]$$

where $B_{1m}(t)$ is a modulated sinusoidal signal. φ and ω_c is initial phase angle and carrier frequency of the RF pulse. There are two rotating fields: a clockwise rotating field called $B_1^+(t)$ and a counterclockwise rotating field called $B_1^-(t)$. The effective $B_1(t)$ field is generally used without the counterclockwise component [64] due to the negligible effect.

After excitation, the magnetization precesses at the Larmor frequency; the voltage signal can then be detected with a RF coil. The voltage signal can be picked up due to Faraday's law.

According to [65], the induced electromotive force (emf) can be calculated using the principle of reciprocity: if a unit current flows in the coil, a magnetic flux density $\vec{B}_{1r}$ at location $\vec{r}$ can be calculated depending on the geometry of the coil. The induced emf from magnetization $\vec{M}(\vec{r},t)$ in the sample volume V_s then is found after suitable normalization as

$$\text{emf} = \int_{sample} (\partial/\partial t)\{\vec{B}_{1r} \cdot \vec{M}(\vec{r},t)\} dV_s \qquad [2.14]$$

2.2 Basic Electromagnetic Theory

2.2.1 Maxwell's Equations

The behavior of electromagnetic fields can be found from Maxwell's equations [66]. $\vec{E}$ and $\vec{H}$ are the electric and magnetic field intensities. $\vec{D}$ and $\vec{B}$ are the electric and magnetic flux densities. The ρ and J are the volume charge density and electric current density, respectively.

$$\begin{aligned} \nabla \times \vec{E} &= -\frac{\partial \vec{B}}{\partial t} \\ \nabla \times \vec{H} &= \vec{J} + \frac{\partial \vec{D}}{\partial t} \\ \nabla \cdot \vec{D} &= \rho \\ \nabla \cdot \vec{B} &= 0 \end{aligned} \qquad [2.15]$$

The electrical and magnetic flux densities $\vec{D}$ and $\vec{B}$ are related to the field intensities $\vec{E}$ and $\vec{H}$. In a vacuum, $\vec{D}$ and $\vec{B}$ are

$$\begin{aligned} \vec{D} &= \varepsilon_0 \vec{E} \\ \vec{B} &= \mu_0 \vec{H} \end{aligned} \qquad [2.16]$$

where ε_0 and μ_0 are the permittivity and permeability of the vacuum; their numerical values are

$$\varepsilon_0 = 8.854 \times 10^{-12} F/m$$
$$\mu_0 = 4\pi \times 10^{-7} H/m \qquad [2.17]$$

The main point of Maxwell's equations is that time-varying magnetic fields give rise to electric fields. This is the basis of detection of the MRI signal.

2.2.2 Faraday's Law of Induction

In time-varying magnetic fields, $\vec{E}$ and $\vec{B}$ are coupled dependently. Time-varying $\vec{B}$ generates $\vec{E}$ from Equation [2.15]. Faraday's law [67] of induction is

$$\oint \vec{E} \cdot d\vec{\ell} = -\frac{d}{dt}\left(\int \vec{B} \cdot d\vec{S}\right) \qquad [2.18]$$

The magnetic flux Φ_s through a surface is defined as

$$\Phi_s = \int \vec{B} \cdot d\vec{S} \qquad [2.19]$$

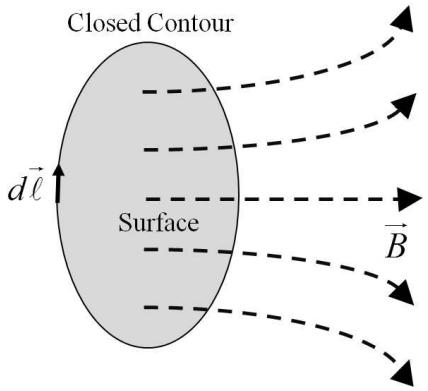

Figure 2.6: Closed contour and surface related to Faraday's law [67]

The emf or induced voltage across the ends of the wire is given by

$$emf = \oint \vec{E} \cdot d\vec{\ell} \qquad [2.20]$$

The $d\ell$ is a small section along the total length of the closed contour. A more familiar form

of Faraday's law is given by

$$emf = -\frac{d\Phi_s}{dt} \qquad [2.21]$$

A time-varying magnetic flux through a loop of wire or any circuit generates voltage. The time-varying magnetic flux associated with the precessing magnetization induces a voltage in the MRI RF receive coil to give rise to the MRI signal.

2.2.3 Biot–Savart Law

The magnetic flux in a circular loop with current I and coil diameter d_c that is coaxial with the z-axis can be calculated by the Biot–Savart law [68], as shown in Figure 2.7.

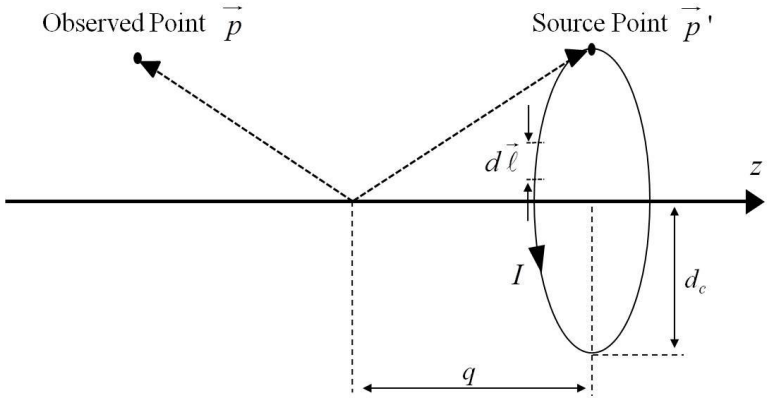

Figure 2.7: Cylindrical coordinates for a single loop of wire along the z-axis [69]

Figure 2.7 shows the cylindrical coordinates used to describe the magnetic flux from a single loop of wire along the z-axis, where r is distance from the observed point and θ is angle between observed point and z-axis. The coordinates refer to the observation point. For thin wires, the formula can be found as

$$\vec{B}(\vec{x}) = \frac{\mu_0}{4\pi}\oint \frac{Id\vec{\ell}\times(\vec{P}-\vec{P}')}{\left|\vec{P}-\vec{P}'\right|^3} \qquad [2.22]$$

where I is the current in the wire and $d\vec{\ell}$ is the vector differential along the current path.

$\left|\vec{p}-\vec{p}'\right|$ is the distance between the wire and the points of observation.

2.2.4 Polarization

The polarization of an electromagnetic wave is defined as the direction of the electrical field vector. An electromagnetic wave is basically composed of two orthogonal components (E_x, E_y) with perpendicular propagation. The two components in circular polarization have equal magnitude and are 90° out of phase. In the plane of an electromagnetic wave traveling with time course *t* in the *z*-direction, the two orthogonal components [70] are as shown in Figure 2.8.

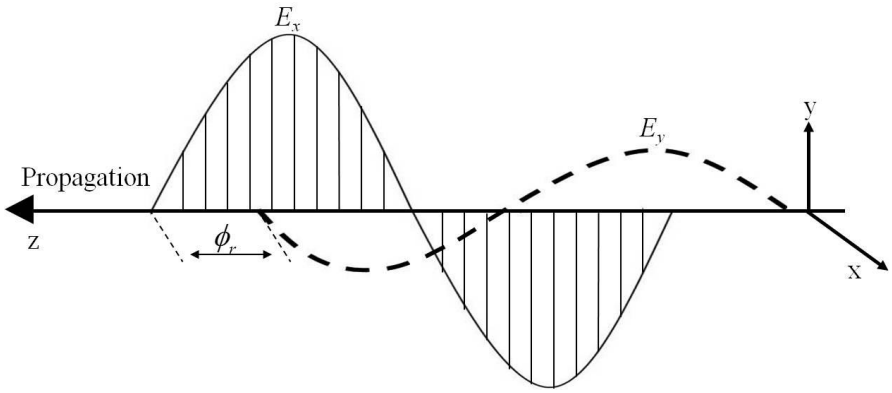

Figure 2.8: Coordinates of polarization [70]

where ϕ_r is the relative phase angle between $\vec{E}_x$ and $\vec{E}_y$. The composite electric field vector $\vec{E}(t)$ rotates with angular frequency in the *xy*-plane. $\vec{E}_x$ and $\vec{E}_y$ are simplified into

$$\frac{\vec{E}_x^2}{A^2}+\frac{\vec{E}_y^2}{B^2}-2\cos\phi_r\frac{\vec{E}_x\vec{E}_y}{AB}=\sin^2\phi_r \qquad [2.23]$$

If they have equal amplitudes (A = B) and a phase difference of 90° ($\phi_r=\pm\pi/2$), this is circular polarization. If they have different amplitudes (A ≠ B) and the phase difference is still $\phi_r=\pm\pi/2$, we get an elliptical polarization in the *x*,*y*-plane. The set of $\phi_r=0$ or $\phi_r=\pi$ means linear polarization.

2.3 Basic Radiofrequency (RF) Coils

2.3.1 RF Transmit and Receive Coils

The RF coil in MRI is used for excitation of the magnetization and to receive the signal from the excited spins. The most important issue for RF coils is quadrature excitation and detection. This coil provides a $\sqrt{2}$ increase in B_1 reception sensitivity and homogeneous RF excitation compared to a linear excitation and detection coil [71, 72]. The B_1 homogeneity of the RF transmit coil corresponds to the flip angle (FA) α of magnetization. FA is determined by the applied B_1 field and is given by

$$\alpha = \gamma B_1 \tau \qquad [2.24]$$

where τ is a finite time interval of the applied RF pulse. The magnitude of B_1 is determined by square root of the power delivered by the RF amplifier. The B_1 sensitivity of the MRI signal depends on the RF receiver coil. The signal of an MRI experiment is accompanied by noise. The noise of the coil is based on thermodynamic principles [16] and is given by

$$\text{Noise voltage} = \sqrt{4kT\Delta fR} \qquad [2.25]$$

where T is the temperature of the coil, Δf is the bandwidth of the MR experiment, and R is the resistance of the coil. Finally, the SNR [16] can be measured as

$$\text{SNR} = \frac{\omega_0^{7/4} B_1}{\sqrt{4kT\Delta fR}} \qquad [2.26]$$

This is due to the increase in SNR is obtained by increasing the frequency and proximity of the RF coil position to the ROI and by decreasing the temperature of the coil, bandwidth, and noise of the sample, coil, and electronics.

2.3.2 Homogeneous Resonators

2.3.2.1 Saddle-Shaped Resonator

The saddle coil and its modified versions are widely used in many applications as RF [73] and gradient coils [74]. Two separated longitudinal current wires are connected in a series path and driven by the same source of current *I*/2 [75], as shown in Figure 2.9.

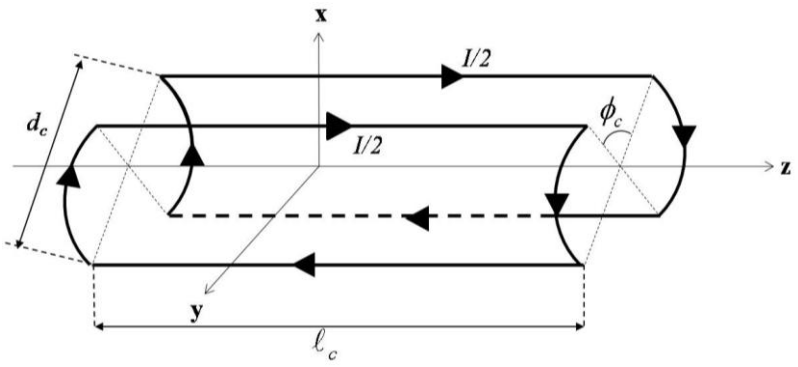

Figure 2.9: Geometry of the saddle coil [75]

where ϕ_c is the angle between the separated closed loop. ℓ_c and d_c are the length and diameter of the coil cylinder. The best B_1 homogeneity is obtained by a ϕ_c of 60°. The B_1 field amplitude depends on the coil length and applied current and is inversely proportional to the coil diameter. The B_1 amplitude is maximum for an infinite coil length. However, in practice, it has a finite length with influence on the amplitude and homogeneity of the B_1 field. Finally, the optimum length ratio (diameter to the length: d_c / ℓ_c) is 1.41 for the maximum B_1 amplitude and 1.66 for the maximum B_1 homogeneity [5, 75].

2.3.2.2 Alderman–Grant Resonator

The Alderman–Grant resonator [38] was proposed to reduce the heating of a sample coming from the created electric field generated by higher coil impedance. It was designed with two H-shaped surfaces made of wider copper foil instead of thin wire and based on the earlier designs of the slotted tube resonator [75], as shown in Figure 2.10.

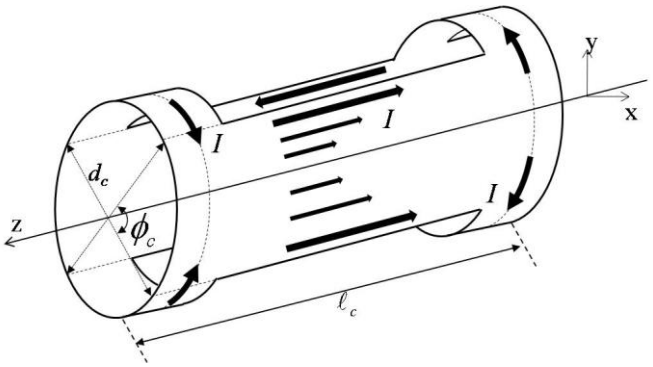

Figure 2.10: Current distribution of the Alderman–Grant resonator [75]

where ϕ_c is the angle between two conductors. The best B_1 homogeneity for the coil is obtained by angle ϕ_c of 85° for the coil diameter d_c. The B_1 amplitude depends on the applied current and special ratio of the coil length to diameter (ℓ_c / d_c). The selected ratio for the best B_1 field homogeneity is between 1 and 1.5 [75].

2.3.2.3 **Birdcage Resonator**

The birdcage resonator [15] provides an improvement for higher frequency applications [76] as shown in Figure 2.11.

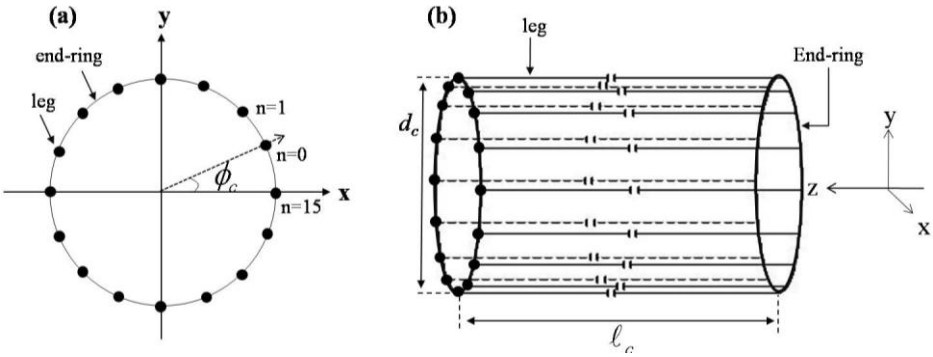

Figure 2.11: Spatial representation of a low-pass 16-leg birdcage coil [15]

The birdcage is based on network segments. Several network segments are excited by a current source. At a particular frequency, standing waves are generated by constructive interference of the wave; this is called the dominant mode, uniform mode, or birdcage mode. High B_1 field homogeneity and sensitivity are created by cosine current distribution in the dominant mode as compared to other modes. In general, birdcage coil is operated with

quadrature mode, by superposing two linear polarized RF fields with the same amplitude and 90° out of phase.

The coil legs *n* are positioned (in Figure 2.11-a) equally on the cylinder d_c and ℓ_c are the diameter and length (in Figure 2.11-b), respectively, of the coil. ϕ_c is the phase and is defined by the driving mode of the birdcage coil. The B_1 field along the y-axis at the center of the birdcage coil [75] is given by

$$B_1 \propto \frac{2\mu_0 I \ell_c}{\pi d \sqrt{\ell_c^2 + d_c^2}} \qquad [2.27]$$

2.3.2.4 **Transmission Line Resonator**

The TEM resonator is based on using a transmission line as a coaxial cavity resonator as shown in Figure 2.12-b.

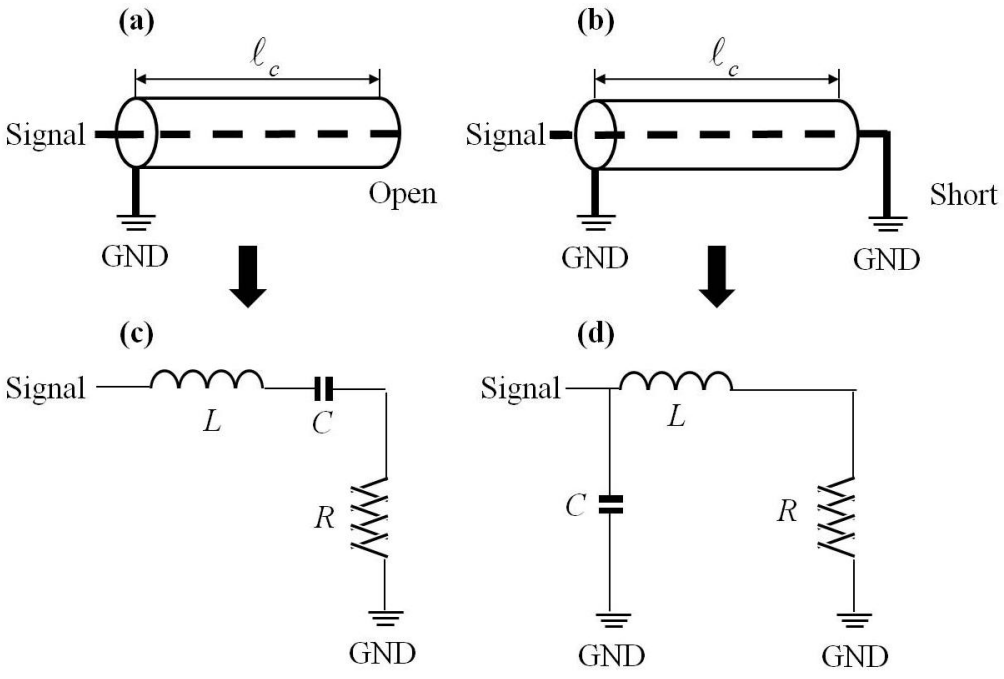

Figure 2.12: Comparison of transmission line and lumped element circuit [77]

The TEM coil is described as a resonator with a capacitive open-ended coaxial line element and designed with a largely inductive coaxial line shorted on both sides. The open-ended and short-ended quarter wave transmissions are modeled with a series resistance, inductance, and

capacitance (*R*, *L*, and *C*) in the resonator [77]. The GND (in Figure 2.12) is ground which is adapted to zero-voltage reference level. Input impedance Z_{in} of a series *RLC* resonant circuit (Figure 2.12-c) is

$$Z_{in} = R + j\omega_r L - j(1/\omega_r C) \quad [2.28]$$

where ω_r is resonant frequency in circuit. Z_{in} of an open-ended quarter wave line (Figure 2.12-b) is

$$Z_{in} = -jZ_0 \cot \beta \ell_c \quad [2.29]$$

where β and ℓ_c are the propagation constant and electrical length of the transmission line, respectively. The TEM resonator can be modeled as a lumped element low-pass filter (LPF, Figure 2.13-b) circuit [77], as shown in Figure 2.13.

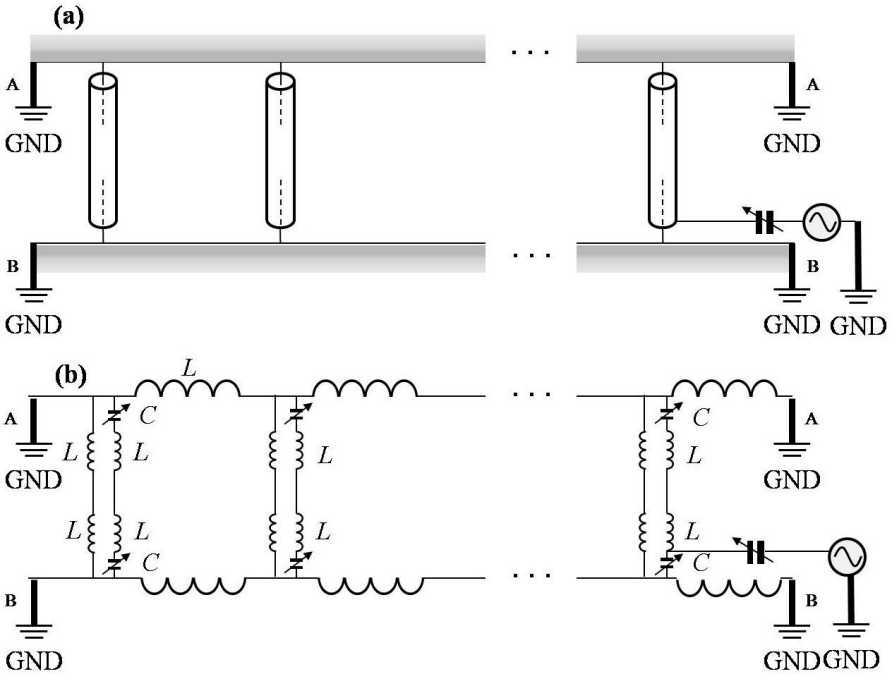

Figure 2.13: Circuit models for TEM coil [76]

The open-ended quarter wave line takes the role of capacitor ($j/\omega C$). The short-ended quarter wave line is similar to the inductance ($j\omega L$). The input impedance of the short-ended quarter wave transmission line is

$$Z_{in} = jZ_0 \tan \beta \ell_c \quad [2.30]$$

Z_0 is the characteristic impedance as defined by the ratio *b/a*

$$Z_0 = (\sqrt{\mu / 2\pi\varepsilon_r}) \ln(b/a) \quad [2.31]$$

where ε_r is relative permittivity and *b/a* is the ratio of the diameters for the outer and inner conductors of the transmission line.

2.3.3 Heterogeneous Resonators

2.3.3.1 Basic Surface Coil

A surface coil has high B_1 sensitivity compared to other volume coils due to the small size of the RF coil and high filling factor. Surface coils are generally used as receive-only types for receiving the B_1 signal efficiently in extended field of view (FOV). When used with a single loop of wire, magnetic flux components are generated in two directions - radial (B_{radial}) and axial (B_{axial}) [8] - as shown in Figure 2.14.

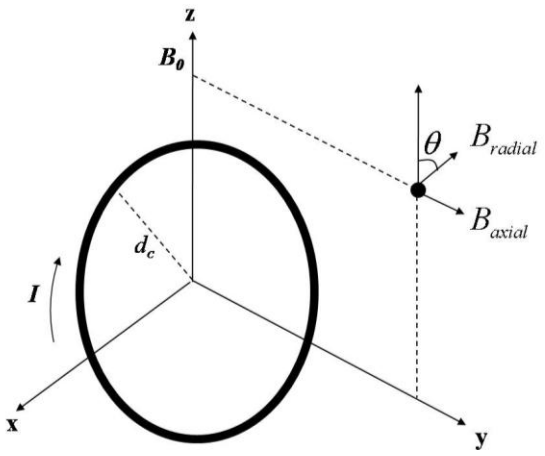

Figure 2.14: Geometry of the basic surface coil [8]

where d_c is the coil diameter. A static magnetic flux B_0 is assumed and aligned along the *z*-direction. The B_1 field along the *y*-direction can be expressed by

$$B_y = B_{axial} = \frac{\mu_0 I \cdot d_c^{\,2}}{2(d_c^{\,2} + y^2)^{3/2}} \qquad [2.32]$$

2.3.3.2 **Phased Array Coil**

The phased array in MR was introduced and described by Roemer et al. [16]. It consists of an assembly of multiple surface coils. Its benefits include a highly sensitive B_1 signal and an extended FOV from the covered small region of a sample. Each received NMR signal of the phased array coil is separately demodulated and digitized by a converter according to the number of receiver channels of the MRI system. Because the receive signal is not sensitive enough from a single RF coil element. Low signals and noisy signals are weighted by special coefficients independently. The weighted signal is rearranged to alternate by a phase shifter. In the array coil, inductive mutual coupling has been considered for receiving the high sensitivity B_1 field. In order to reduce the interference for mutual coupling between surface coils, many methods have been suggested. A well-known method to reduce the inductive coupling between adjacent coils is relative positioning [16, 78] as shown in Figure 2.15.

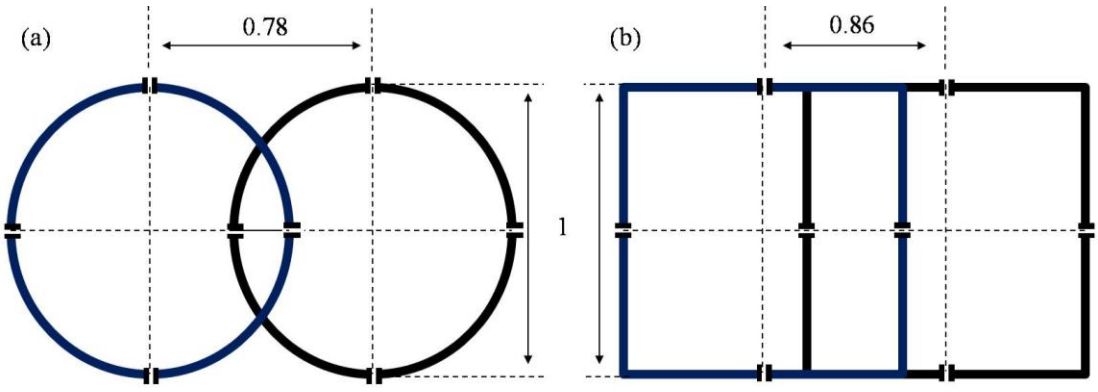

Figure 2.15: Normalized relative positioning of (a) circular and (b) square loops for reducing the mutual inductance [16]

The inductive coupling depends on the distance between each planar coil. The optimized overlapping distance between two planar coils is determined by the relative ratio of the diameter and distance from the centers of the two coils. The optimized ratio is 1/0.78 (diameter/distance) for circular loops (Figure 2.15-a) and 1/0.86 (length of square/distance) for square loops (Figure 2.15-b). Overlapping the adjacent coils perfectly does not solve the mutual inductance problem since a small significant coupling still exists between distant coils

(i.e., second- and third-nearest neighboring coils). This mutual interaction can be reduced by connecting the coils to low-input impedance preamplifiers with impedance transformation networks [16], as shown in Figure 2.16.

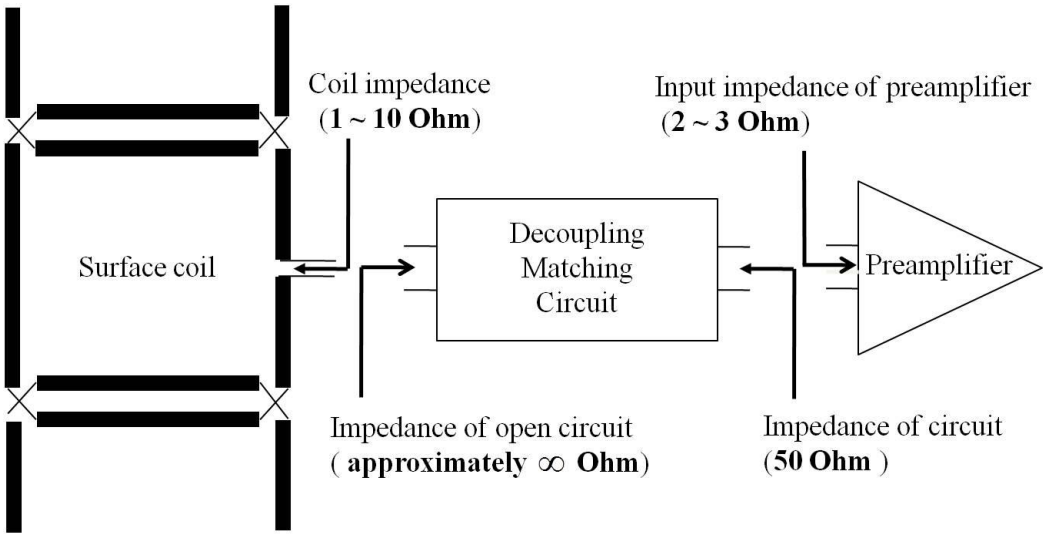

Figure 2.16: Isolation preamplifiers for reducing the mutual inductance [16]

If the input impedance of the preamplifiers is very small, there is no current flowing in the surface coils. The absence of a current in the coils does not create the magnetic coupling.

3 7T SINGLE CHANNEL TX/RX COILS

In this chapter, four CP RF coils and circuitry are described.

3.1 Motivation

The use of UHF MRI scanners has gained attention since they can theoretically provide images with a higher SNR [79, 80], enhanced T_2^* contrast [12], and increased dispersion of chemical shifts [81] proportional to the main magnetic field strength. However, the acquisition of *in-vivo* brain images, especially with the use of UHF MRI, faces some problems by operating at higher frequency, such as RF attenuation, asymmetric wave propagation, and phased delay in biological tissue [82, 83]. Therefore, B_1 field inhomogeneity is dominated by interactions between the RF coil and object as well as the fundamental dielectric resonance generated by a standing wave [26, 84]. It is difficult to develop RF coils that can be implemented for UHF MRI. The effective RF wavelength is shortened due to the permittivity and damped by the conductivity of objects [85]. In a UHF environment, a signal waveform may experience distortion where the original waveform cannot be maintained due to superposition with different phases [25]. In addition, crosstalk such as coupling increases as the frequency increases. Strangely, the non-substantial component of the coil acts as the substantial component, thus radiating more electromagnetic energy [25]. A HBC, HSBC, DH, and ST coils are well-known types of CP volume coils for MRI [86] and are shown in Figure 3.1.

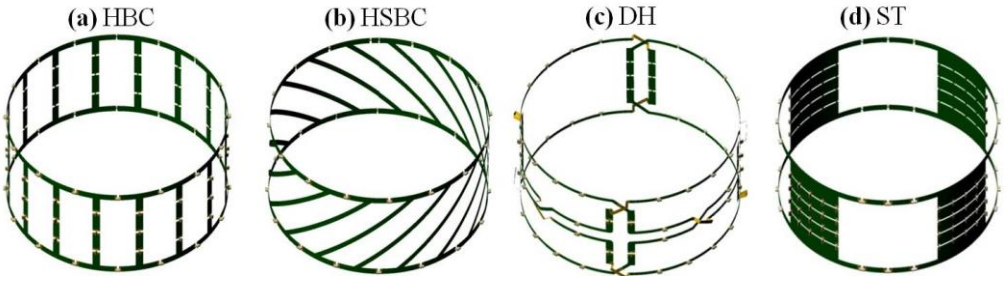

Figure 3.1: Pictorial representation of circular polarized volume coils

The HBC (Figure 3.1-a) is based on a lumped element delay line with two end rings (ERs). The current in the capacitors is also proportional to $\sin\theta$, where θ is the azimuth angle in cylindrical coordinates [87]. Apart from the structural difference between a traditional HBC [15] and an HSBC (Figure 3.1-b) where the leg conductors are angled instead of being

straight conductors along the main magnetic flux B_0, a major difference stems from the controllability of the B_1 field in variation of the current phase. For CP modes, the phase of the current in the coil legs is increased in steps from zero to 2π around the circumference of the RF coil [36]. The DH configuration (Figure 3.1-c) is based on a one-turn Helmholtz coil design and has eight conducting wire elements for the CP mode; it is constructed specifically to improve coil performance such as the SNR and B_1 homogeneity through the use of two one-turn Helmholtz forms [88]. The coil geometry consists of two coils with a rectangular shape for homogeneous B_1 field distribution due to the current passing through the conducting wire of coil. Each coil generates a B_1 field with different channels 90° out of phase used to allow coils to be operated in CP mode. The resultant RF magnetic flux is superposed as orthogonal B_1 components.

The ST configuration (Figure 3.1-d) is a simplified version of an inductive coupling structure based on the well-known design of Alderman-Grant coil [38]. The cylindrical coil has four copper foils symmetrical with respect to the B_0. The number of legs was designed and modified for CP operation in this study and must be optimized by an integral factor of four.

All CP volume coils in the UHF intrinsically generate an inhomogeneous B_1 field. Although there are slight differences in RF coil performance, experimental data must be provided to aid in coil selection, particularly for volume imaging and searching for local Tx-only coil to be used as the multi-channel array coil. In particular, B_1^+ inhomogeneity has to be considered to improve the contrast in chosen ROI in an MR image. The aim of this study was to compare lumped-element CP volume coils for the HBC, HSBC, DH, and ST coils at 7T in terms of SNR, signal homogeneity, and maps of the effective flip angle for the same coil dimensions.

3.2 Material and Methods

3.2.1 System Hardware

The 7T MRI system (Magnetom, Siemens, Germany) was composed of a 90 cm diameter bore superconducting magnet (Magnex Magnet Technology, Oxford, UK) connected to a Syngo console. The whole-body gradient coil had a diameter of 60 cm inside the magnet; it provided a maximum gradient strength of 40 mT m^{-1} s^{-1} in the Incheon (Republic of Korea) 7T MRI System and 70 mT m^{-1} s^{-1} in the Magdeburg (Germany) 7T MRI System. The RF amplifier system was a single-channel system, as shown in Figure 3.2.

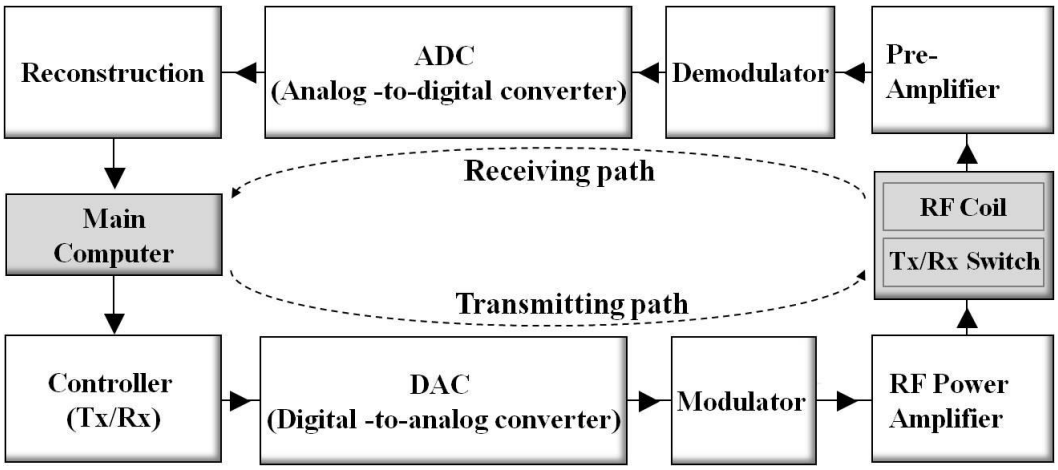

Figure 3.2: Block diagram of MRI system

For transmission, RF power amplifiers using a maximum of 1000 W for *in vivo* brain imaging were driven by local oscillators for oscillating magnetization. At a resonant frequency of 297.2 MHz, nuclear magnetization was tilted along the main magnetic flux B_0. The RF signal including information for imaging and a carrier signal of 297.2 MHz were modulated, and combined signals were amplified. For quadrature driving, the hybrid power splitter (90° phase shift) was controlled by the host computer for providing the CP mode. For receiving, the directions were reversed. The MR signal was reconstructed by the use of a demodulator and analog-to-digital converter (ADC). B_1 sensitivity mainly depended on the RF coil and preamplifier performance. In general, preamplifiers were designed with the cascade method to acquire higher B_1 sensitivity. The Tx/Rx switches in the middle part had the dual function of connecting the transmitting RF power amplifier and preamplifiers of the receiving components.

3.2.2 Design of Circular Polarized RF Coils

The HBC coil was composed of 16 legs and two ERs, both with a width of 10 mm for ^{1}H proton MR imaging at 297.2 MHz. Its dimensions were 150 mm in length, 300 mm in diameter around an acrylic cylinder. Each end-ring (ER) segment was treated as a rectangular strip with a width of 10 mm. The values of the tuning capacitor (C_T) used in the coil were 6.8 pF in the ERs and 3.9 pF in the four segmented legs. In addition, a balanced capacitor circuit for 50 Ohm impedance matching was adopted. The used matching capacitor (C_M) was 330 pF; the tuning-matching capacitor (C_{TM}) used approximately 4 pF for precise tuning. To operate in CP mode, the alternating current (AC) source was fed with two positions - one of the ERs and

90° out-of-phase of that - via a coaxial cable. The HSBC coil was constructed similar to the HBC coil except for a 45° angled leg. It also has a leg length of 212 mm with a structural increment of 62 mm relative to the HBC coil. The HSBC coil was tuned to 297.2 MHz by judicious selection of capacitor values ranging between 2.7 and 3.3 pF. The coil had a smaller capacitor value compared to the HBC coil due to the larger inductance value in the leg. The quadrature driving method was the same as that for the HBC coil; two feeding ports were separately positioned in the ERs 90° apart geometrically and electrically. The DH coil was designed for quadrature operation consisting of two nested orthogonal coils that generally have a rectangular shape. A DH geometrical layout (Figure 3.3-a) of each single Helmholtz coil (Figure 3.3-b, -c) spatially overlapped coil is displayed in Figure 3.3.

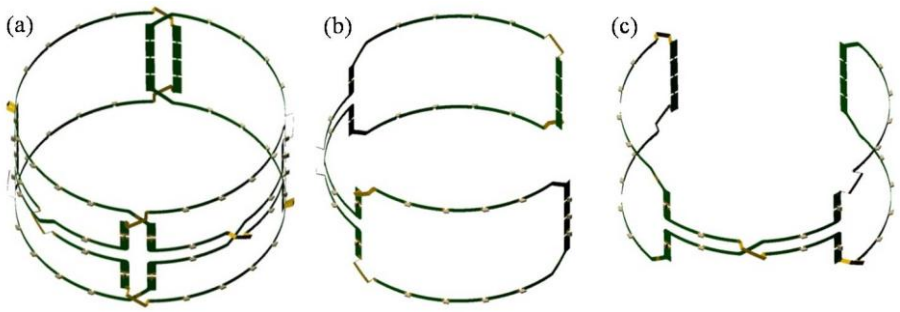

Figure 3.3: Geometry of the (a) DH coil is comprised of (b, c) two orthogonal Helmholtz coils

Each Helmholtz coil was soldered using a copper bridge 10 mm in height to preserve electrical isolation over the spatially intersected coils. Each Helmholtz coil provided one signal channel of two rectangular shapes 90° apart. There were four pairs of parallel conductors; each paired parallel conductor was composed of two small adjacent parallel conductors. Two small conductors were separated by 20 mm in distance, 5 mm in width and 10 mm in interval between parallel conductors functioning as a leg; this produced the B_1 field via the flow of AC. Moreover, in terms of B_1 field homogeneity, AC was fed in the cross-point situated at the midsection of the coil height along the same direction of the main magnetic flux B_0. Each leg had a total series tuning capacitance of approximately 4.7 pF distributed into three series capacitors. To optimize tuning frequency and impedance matching, the capacitances used were 4.7 pF for the ERs, 470 pF for C_M, and 7.8 pF for C_{TM}. The ST coil was based on an inductively coupled Alderman and Grant probe. The width of each of the four horizontal bands covered a radial distance of 40°. Therefore, the optimized window angle between the two conducting copper foils of the ST coil was 50° to maximize the B_1 field homogeneity. In addition, the ERs were 10 mm in width. The RF port was directly fed in the legs with AC for the CP mode. C_T used in the coil for ERs between legs connected via three

series was 8.2 pF. Each leg was distributed into four segments and contained five parallel 1.5 pF capacitors.

3.2.3 Quadrature Hybrid Coupler and PIN Diode Switches

For quadrature driving, RF power was split through a quadrature hybrid coupler and controlled by Tx/Rx switches. A developed coupler where the input is split into two RF signals of equal magnitudes and 90° out of phase ϕ [75] is shown in Figure 3.4.

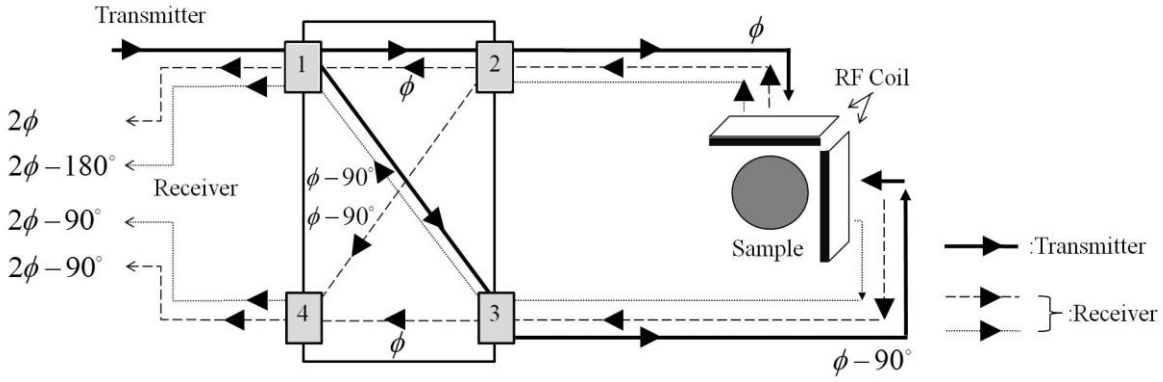

Figure 3.4: Quadrature driving mechanism [75]

For transmission, an RF power signal with the same amplitude and 90° out of phase was applied in the RF coil. However, for receiving from a symmetric sample and coil arrangement, a phase shift phenomenon was created in ports 1 and 4. In port 1, the two signals canceled out, and no signal leaked toward the transmit load. However, two quadrature signals in port 4 were summed up [75]. The Tx/Rx switches based on a PIN diode were designed as shown in Figure 3.5-a.

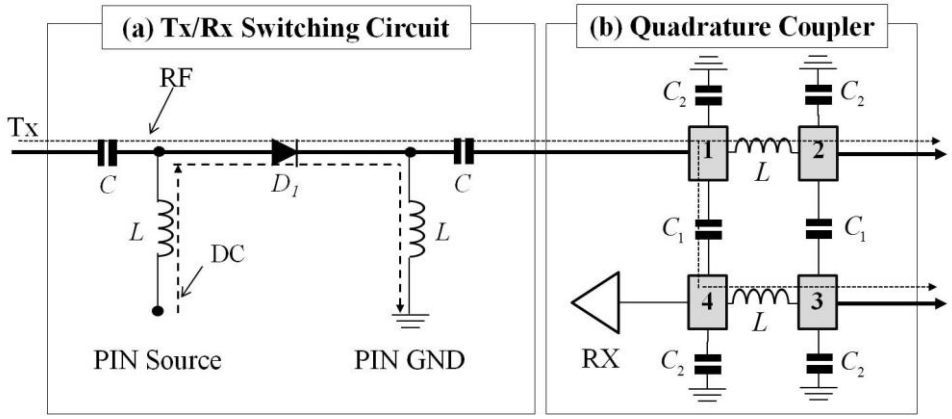

Figure 3.5: Basic circuit modeling of (a) Tx/Rx switches and (b) quadrature hybrid coupler

The purpose of the Tx/Rx switches is to control the Tx and Rx pathway and to protect the receiver system, especially the preamplifiers, from damage due to the high RF power of the transmit mode in MRI systems. The PIN diode of D_1 (in Figure 3.5-a) was put in the path between the transmit port of the RF amplifier and input port of the quadrature coupler. In transmit mode, a direct current (DC) bias was applied in the PIN diode. As a result, D_1 allowed RF power to flow to port 1 (in Figure 3.5-b) of the quadrature coupler. Figure 3.5-b shows the schematic of a quadrature hybrid coupler using lumped elements. When all ports were matched to 50 Ohm impedance, the power of the input port (port 1 in Figure 3.5-b) split equally-but 90° out of phase-to output ports 2 and 3. Port 4 was perfectly isolated from port 1 and connected to the preamplifier for amplifier the RF signals. The two capacitors C_1 and C_2, and inductance L (in Figure 3.5-b) of the quadrature coupler were calculated at the desired resonance frequency ω_r.

$$C_1 = 1/(\omega_r Z_0) \quad [3.1]$$

$$C_2 = (\sqrt{2}-1)/\omega_r Z_o \quad [3.2]$$

$$L = (Z_0\sqrt{2})2\omega_r \quad [3.3]$$

The Tx/Rx switches and quadrature hybrid coupler were optimized for this study and simulated using Ansoft Serenade v8.5, as shown in Figure 3.6.

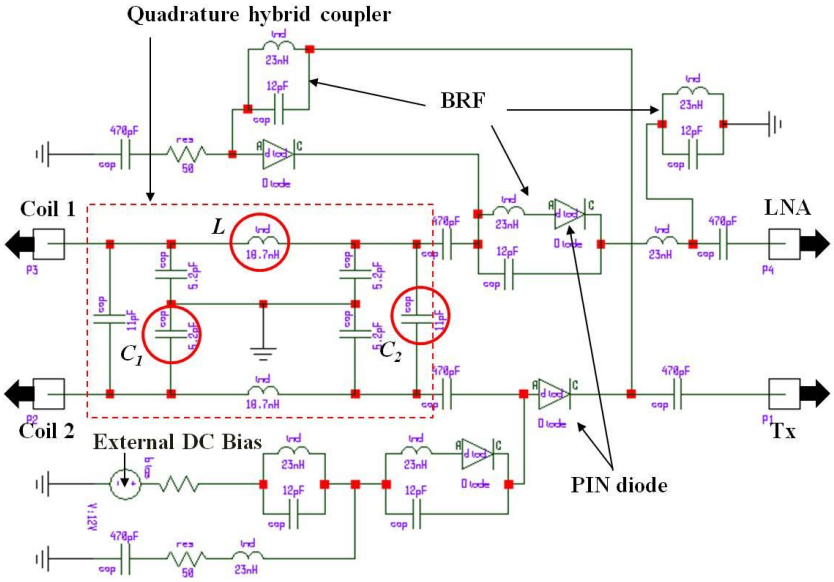

Figure 3.6: Circuit modeling of Tx/Rx switches and quadrature hybrid coupler

The figure is based on the calculated values of C_1, C_2, and L. In addition, the band-rejection filter (BRF), low-pass filter (LPF), higher capacitance for DC blocking, and RF choke for AC blocking were added. Note the PIN diodes in the Rx path which activate a BRF when bias current flows through both PIN diodes, thus blocking the Rx input from Tx power. Therefore, there was little difference between the optimized value using the circuit simulation program (C_1/C_2/L: 11 pF/4.4 pF/18.7 nH) and the calculated value from the equation (C_1/C_2/L: 10.6 pF/4.4 pF/18.7 nH).

Figure 3.7-a and Figure 3.7-b shows the reflection coefficients Γ for Ports 2 (P_2) and 3 (P_3) of the quadrature coupler (in Figure 3.6).

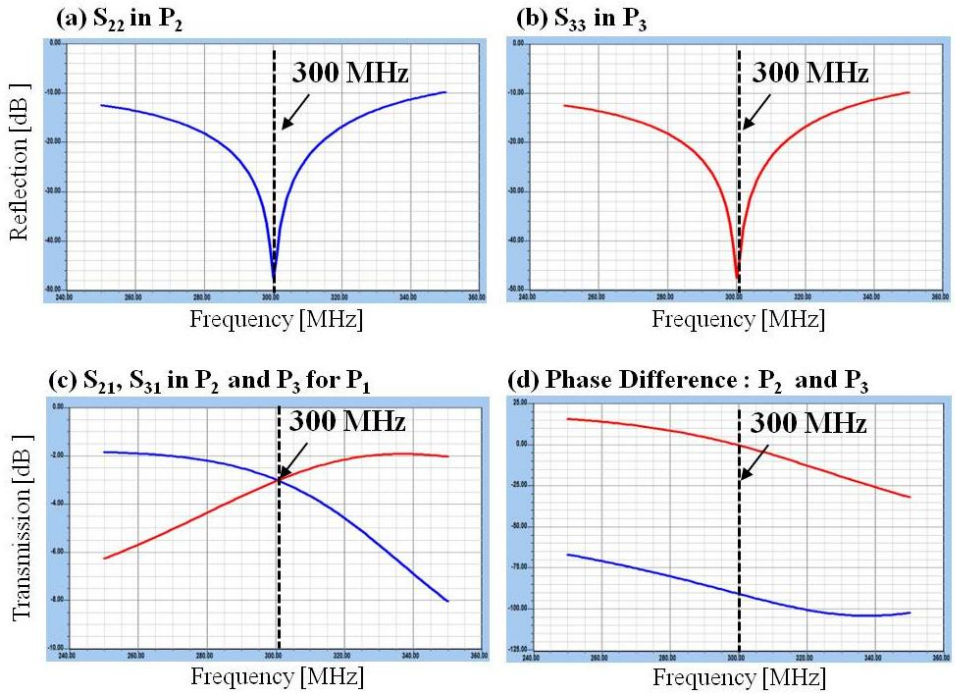

Figure 3.7: S-parameter of combined Tx/Rx switches and quadrature hybrid coupler

The reflection coefficient Γ is determined by

$$\Gamma = \frac{(Z_{in} - Z_0)}{(Z_{in} + Z_0)} \qquad [3.4]$$

where Z_{in} and Z_0 are the input and output impedance, respectively, of the circuit. The remaining reflection coefficients at P_2 and P_3 were approximately -50 dB for a central frequency of 300 MHz. The lumped element hybrid coupler provided a -3dB split with a 90° phase shift, as shown in Figure 3.7-c and Figure 3.7-d.

3.2.4 Phantom Studies

The plastic cylinder phantom (Siemens, Germany) used in this study was 160 mm in diameter, 380 mm in length, and 7300 mL in volume. The phantom was filled with a solution consisting of 1.24 g/L $NiSO_4 \times 6H_2O$ and 2.62 g/L NaCl per 1000 g H_20 (distilled water), as shown in Figure 3.8.

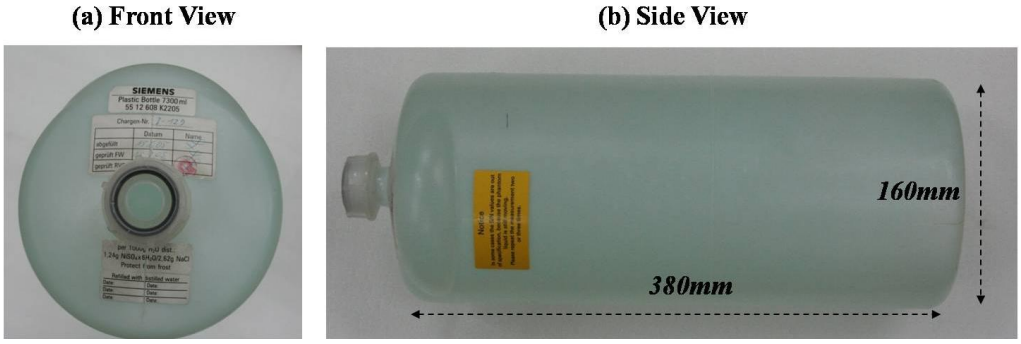

Figure 3.8: Plastic cylinder phantom (distilled water)

This phantom was chosen for its similar permittivity (ε_r = 50.5) and conductivity (σ = 0.657 S/m) relative to the human brain and to minimize the difference in tuning frequency and impedance relative to a loaded oil phantom. The phantom experiments were designed to evaluate coil performance in terms of B_1 signal homogeneity and SNR for each CP coil. All parameters were compared by T_2^* weighted MR contrast imaging based on a gradient recalled echo (GRE) sequence (repetition time (TR) / echo time (TE) / α = 400 ms/10 ms/20°, FOV = 256 mm × 256 mm, matrix size = 256 × 256, pixel bandwidth = 260 Hz, number of average = 1, acquisition time = 1 min 42 s, slice thickness = 3 mm, and central axial slices). The cylindrical distilled phantom and CP volume coil were positioned as close to the iso-center of the magnet bore as possible to allow the comparison study to be accurate as possible.

3.2.4.1 **SNR Maps**

The SNR maps of each coil were obtained for magnitude GRE images and compared with different color scale in the water phantom. The magnitude images used two bytes to store a 12-bit grayscale value (range from 0 to 4095) for each pixel. The maximum B_1 signal intensity (SI) was represented in red, and the minimum SI was represented in blue.

3.2.4.2 Mean SNR Measurement

The mean SNR was measured from an ROI covering the entire image in axial slices as shown in Figure 3.9. The SNR measurement was based on the specifications of the National Electrical Manufacturers Association (NEMA) [89]. The noise (σ_{noise}) was measured and averaged from the SD in four small background ROIs (BG_1–BG_4 in Figure 3.9); these were in each corner covering an area of 10 × 10 pixels and placed within ghost-free regions of the background outside of the image [90]. The mean SNR was computed as

$$\text{SNR} = 0.66 \times (\text{mean signal/average of noise region SD}) \quad [3.5]$$

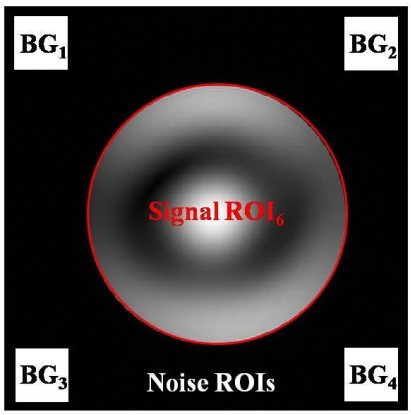

Figure 3.9: ROI definition for the mean SNR measurement in the phantom

3.2.4.3 Signal Homogeneity

For quantitative comparison of the B_1 field homogeneity, the number of pixels between the maximum B_1 SI and 66.6% below in the two-dimensional GRE images was counted and compared. The pixel-counting method of discarding the lowest 20% SI for the maximum B_1 SI was the same as that used for the contour profile.

3.2.4.4 Maps of Effective Flip Angle

To compare the FA maps, the B_1-map sequence was performed for all CP volume coils. Evaluating the B_1^+ homogeneity is essential. There are several B_1-map measurement methods

based on increasing FAs [91], signal ratio [92], and stimulated echoes (STE) [93]. The general approach is the double angle method (DAM) [94], which involves acquiring two different GRE or spin echo (SE) images from FAs α_1 and α_2.

$$\alpha(i,j) = \arccos\left(\frac{I_2(i,j)}{2I_1(i,j)}\right) \quad [3.6]$$

where $I_1(i,j)$ and $I_2(i,j)$ are the SI provided by different FAs in special pixel locations (i,j) of MR images 1 and 2. The α_2 was chosen to be approximately double the number for α_1. For accurate measurement, two MR images have to match the conditions of a long repetition time (TR $\geq 5T_1$) and short TE.

For a simpler FA measurement, the B_1-map sequence (WIP_397_B1MAP) was used as provided by the vendor (Siemens, Germany) for SE-type FA measurement [95], without the diffusion-weighted imaging. In this method, two refocusing pulses generate a SE and STE after slice selective excitation. The FA is defined as

$$\alpha = \arccos\left(\frac{A_{STE}}{A_{SE}} \cdot e^{TM/T_1} - 1\right) \quad [3.7]$$

where A_{STE} and A_{SE} is the amplitude of STE and SE. α is the local FA and T_1 is the local relaxation time. *TM* is the mixing time duration between the two refocusing pulses. The scan parameters of the B_1-map sequence are TR/ TE/ α = 1000 ms/ 14 ms/ 50°, FOV = 256 mm × 260 mm, matrix size = 256 × 256, pixel bandwidth = 260.4 Hz, acquisition time = 4 min 16 sec, slice thickness = 5 mm with single-slice axial, sagittal, and coronal imaging. The maps of effective FA α_{eff} for the given FA α_{giv} (= 50°) was provided for evaluation of the B_1^+ homogeneity.

3.2.4.5 **Measurement of Averaged Effective Flip Angle Value**

The averaged α_{eff} value for α_{giv} of 50° was measured and averaged in four different ROIs (*i*–*iv*) that covered the peripheral region referenced in the center region shown in Figure 3.10. The first ROI (*iv*) was chosen to cover the entire α_{eff} map; the second ROI (*iii*) corresponds to

50% of the pixel amount in the first ROI; the third ROI (*ii*) corresponds to 50% of the pixel amount in the second ROI; and the fourth ROI (*i*) corresponds to 25% of the pixel amount in the third ROI. In particular, for the sagittal and coronal images of the phantom, the ROI covering the entire α_{eff} map was chosen as the length of the RF coil corresponding to 150 mm.

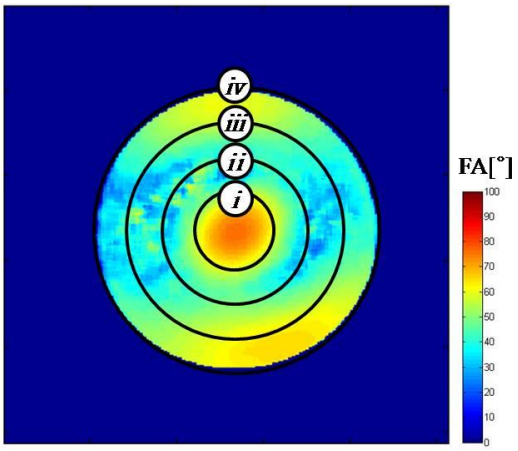

Figure 3.10: Four different ROI (i–iv) for measuring the averaged FA value

3.2.5 Human Brain Studies

All human subject studies were performed after a review by the human research committee on the subject. The SNR and effective FA maps were measured on GRE images of the human brain acquired with the same parameters as those used in the phantom study. In addition, for only the human brain study, a one-dimensional SI profile was performed to compare the B_1 homogeneity. The B_1 homogeneity range was defined by the measured pixels as the distance between the maximum B_1 SI and 66.6% below the maximum.

3.2.5.1 Image Localization

For accurate comparison of human brain images by elimination of the slice difference due to imaging position, a magnetization-prepared rapid acquisition with gradient echo (MPRAGE) two-dimensional sequence was utilized. Parameters included TR/TE/α = 4000 ms/2.77 ms/20°, inversion time (TI) = 1190 ms, FOV = 256 mm × 256 mm, matrix size = 512 × 512, pixel bandwidth = 470 Hz, acquisition time = 2 min 10 s, and slice thickness = 4 mm. An MPRAGE two-dimensional sagittal image was preferentially obtained. Subsequently, a GRE

axial image was acquired through the anterior commissure (AC) to posterior commissure (PC) center line. A GRE coronal image was acquired using an AC-PC line perpendicular to the GRE axial image. Finally, a GRE sagittal image was obtained with the longitudinal fissure of the GRE axial image.

3.2.5.2 **Signal Intensity Profiles**

In the human brain imaging, the B_1 field homogeneity was compared using one-dimensional SI profiles of axial slices along the left-right (L-R) direction and sagittal slices along the superior-inferior (S-I) direction for all CP coils. A smoothing method was adapted to define the one-dimensional profile for each coil by averaging ±10 pixels about a reference pixel.

3.2.5.3 **Mean SNR Measurement**

The average of the mean SNR values in ROIs in axial GRE images of the human brain was chosen [96] and measured with the same methods as those used for the phantom study for an ROI that covered the entire image (ROI_6 in Figure 3.11). In addition, each of the five ROIs (ROI_1–ROI_5 in Figure 3.11) with circular shapes corresponding to 1100 pixels was used for the human brain study only; these are shown in Figure 3.11.

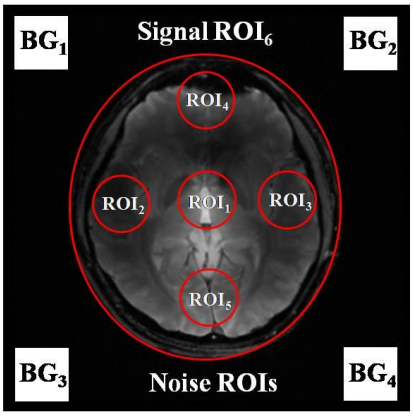

Figure 3.11: ROI definition for the mean SNR measurement in the human brain

3.3 Results

3.3.1 Electrical Characteristics

The designed CP volume coils, Tx/Rx switches, and quadrature coupler were measured and characterized by using a vector network analyzer (N.A., 8753ES, Agilent Technologies, Santa Clara, CA USA). Conventional short-open-load-through (SOLT) calibration was first performed to eliminate the effects of the cables.

3.3.1.1 Circular Polarized Volume Coils

All four CP coils used for performance comparison were manufactured; they are shown in Figure 3.12.

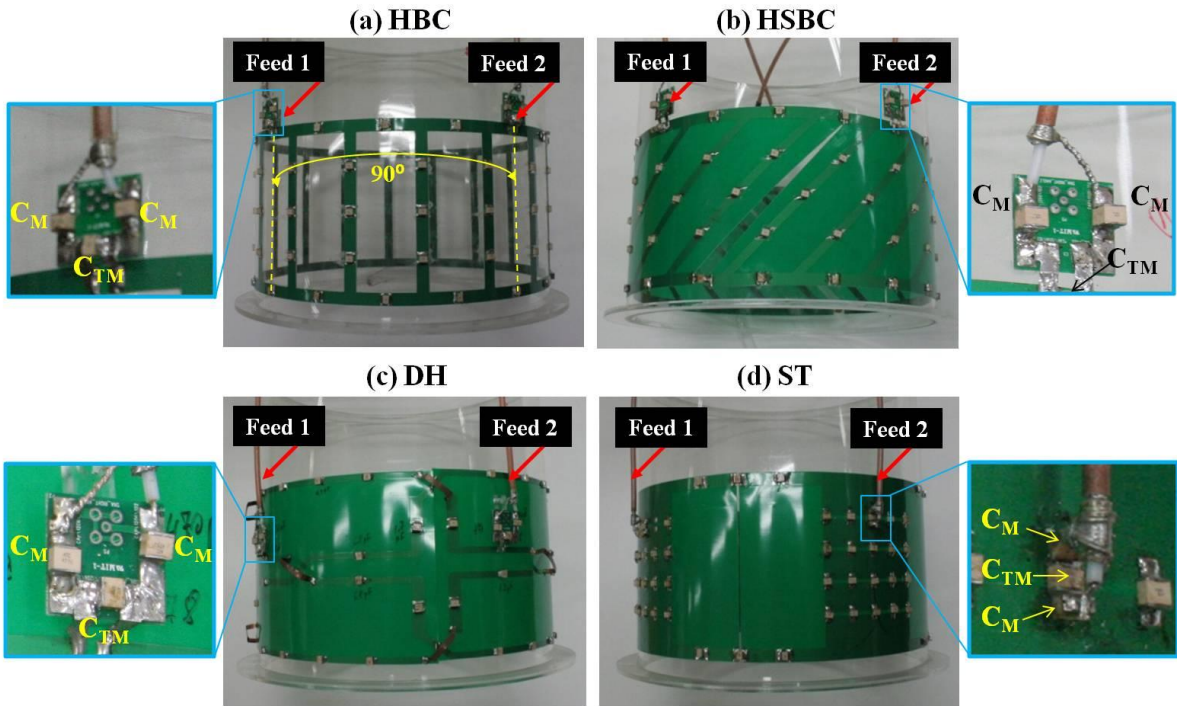

Figure 3.12: Four designed circular polarized volume coils

For quadrature driving, two 50 Ohm coaxial cables (RG 400/U bulk coaxial cable) in the two hybrid birdcage coils were attached at two points separated by 90° rotations as shown in Figure 3.12-a, b. The inner shield inductor of coaxial cable was attached to the C_T left side with the C_M. The outer signal conductor of coaxial cables was attached to the C_T right side

with the C_M. The DH coil was rigidly mounted offset precisely 90° relative to each Helmholtz as shown in Figure 3.12-c. The small mounted offset in the each Helmholtz leads to a strong inductive mutual coupling between the coils, thereby the reflection coefficient of the individual Helmholtz coil increase. The elements of the Dual Helmholtz coil overlap each other and are driven with a 90° phase difference. The cylindrical shaped ST coil has four fold symmetric legs with respect to its main magnetic direction and feed in two points separated by 90° for quadrature RF excitation and detection. Two electrically and geometrically orthogonal co-resonant modes was optimized using window angle of 50°. All coils were matched to 50 Ohm and tuned to 297.2 MHz while loaded with human head on a test bench using a N.A. The degree of isolation in each coil between the quadrature ports was greater than -20 dB, and the reflection coefficient was better than -25 dB, as shown in Figure 3.13.

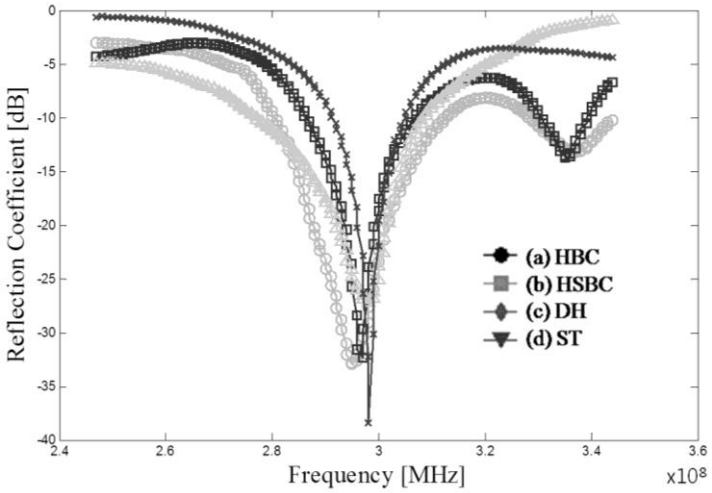

Figure 3.13: Reflection coefficient for each circular polarized volume coil (Figure 3.12)

3.3.1.2 **Tx/Rx switches and Quadrature Hybrid Coupler**

Figure 3.14 shows the assembled Tx/Rx switches and quadrature hybrid coupler using lumped elements; the coupler is based on simulated data for an electrical circuit. The observed return losses for the Tx port (P_1) of -27.63 dB and Rx port (P_4) of -34.14 dB were consistent with the specified - 30 dB return loss of the simulation. The isolation between ports 1 and 4 at 297.2 MHz was around -19 dB, and the transmissions in the through (P_{21}) and coupling (P_{31}) paths were around -3.18 and -2.91 dB, respectively.

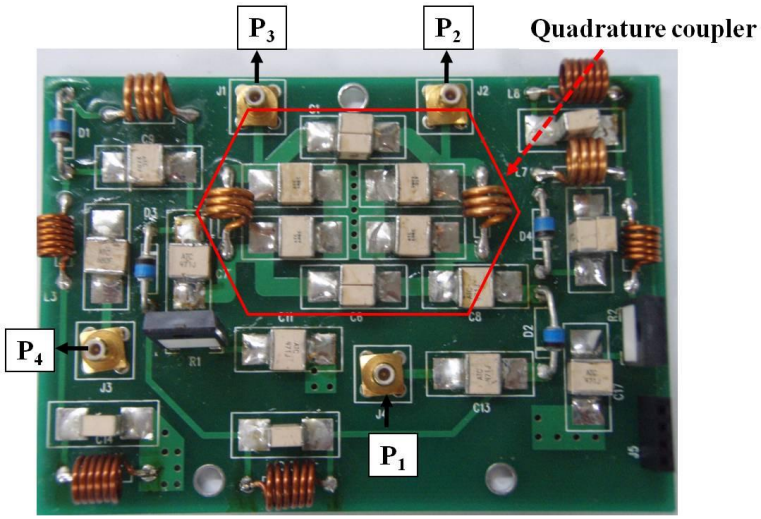

Figure 3.14: Designed Tx/Rx switches and quadrature hybrid coupler

In the RF transmit case, power was split from port 1 equally and distributed at a 90° phase difference to ports 2 and 3. No power was coupled to port 4. The isolation and directivity was approximately -20 dB at the center frequency of 297.2 MHz. Several other characteristics of quad hybrids were measured as shown in Table 3.1.

Table 3.1: Characteristics of the assembled circuit (Figure 3.14)

Mode	Measurement
Tx Reflection (S_{11})	-27.63 dB
Rx Reflection (S_{44})	-34.14 dB
Reflection Coefficient (S_{22})	-29.29 dB
Reflection Coefficient (S_{33})	-27.04 dB
Transmission (S_{21}) in Through Path	-3.18 dB
Transmission (S_{31}) in Coupling Path	-2.91 dB
Phase difference between Port 2 and 3 for Port 1	0.15° (89.14°, 88.99°)
Isolation (S_{14}) between Port 1 and 4	-18.97 dB

3.3.2 SNR Maps

The SNR maps of the phantom derived from GRE images for the HBC, HSBC, DH, and ST coils and their comparison with a color map are shown in Figure 3.15. All SNR maps were obtained for all magnitude images and are illustrated to show the difference in terms of color scale. The HSBC coil (Figure 3.15-b) displayed a similar B_1 field distribution as that of the

HBC coil (Figure 3.15-a). The peripheral region in an axial slice obtained with the DH (Figure 3.15-c) and ST coils (Figure 3.15-d) displayed a widely distributed green region representing roughly 50% of the maximum B_1 SI as compared to the HBC and HSBC coils.

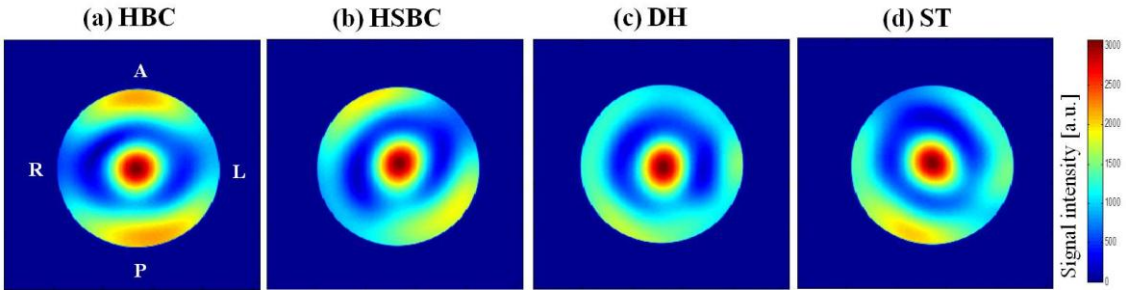

Figure 3.15: SNR distribution of 16 cm diameter water cylinder phantom GRE images for four CP coils

All four coils displayed similar B_1 field distributions focused only in the center along the A-P and L-R directions. However, the HBC and HSBC coils had a more definite B_1 SI in the outermost region relative to the DH and ST coils. In contrast, the HBC and HSBC coils displayed less prominent B_1 SI in the peripheral regions excluding the center.

The B_1 field distribution of the human brain was evaluated for the HBC, HSBC, DH, and ST coils using the same methods as those for the phantom study; the results are shown in Figure 3.16.

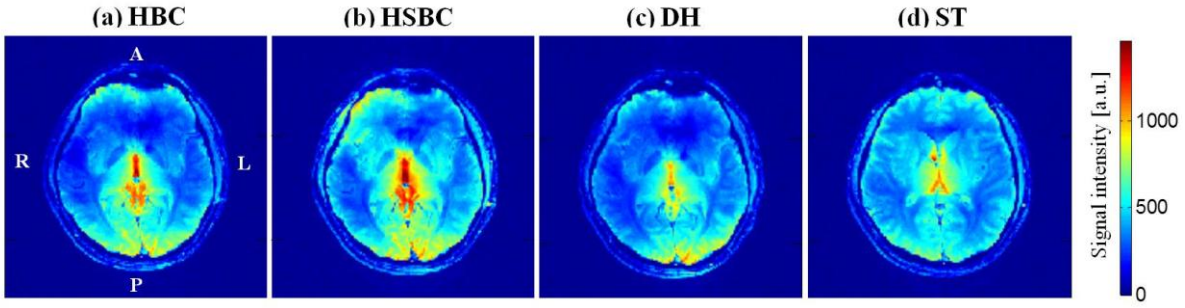

Figure 3.16: SNR distributions of the human brain GRE images for four CP coils

The maximum B_1 transmit and receive signal intensity (SI) was represented in red, and the minimum SI was represented in black. The ST coil (Figure 3.16-d) shows higher SNR in the peripheral region of the human brain compared to the other three coils. On the axial slice, the SNR distribution for the ST coil was distributed with more homogeneity from the center region. In particular, along the A-P direction, the HBC (Figure 3.16-a) and DH (Figure 3.16-c) coils showed relatively low B_1 SI at the anterior part as compared to the superior part of the human brain.

3.3.3 Mean SNR Measurement

The measurements of the mean SNR was compared for all CP coils in the phantom and human brain in terms of the axial GRE images, as shown in Table 3.2.

Table 3.2: Mean SNR measurement for the (a) phantom and (b) human brain.

CP Coils	Mean SNR			Mean signal						SD
	(a) Phantom	(b) Human brain		Human brain						
	ROI 6	ROI 1–5	ROI 6	ROI 1	ROI 2	ROI 3	ROI 4	ROI 5	ROI 6	σ_{Noise}
HBC	214.7	82.6	21.1	211.6	68.5	85.5	87.5	173.3	111.4	3.4
HSBC	233.7	85.2	20.8	216.2	77.6	94.8	88.1	169.6	113.9	3.6
DH	235.8	78.3	18.5	184.8	71.7	101.1	73.8	162.1	104.8	3.7
ST	212.8	104.5	29.4	259.7	115.4	120.1	122.9	173.8	142.1	3.1

The mean SNR measured in ROI 6 of the phantom (Table 3.2-a) was chosen to cover the entire image. The obtained values were 214.7 for the HBC coil, 233.7 for the HSBC coil, 235.8 for the DH coil, and 212.8 for the ST coil; these values were 8% higher for the HSBC coil, 9% higher for the DH coil, and 1% lower for the ST coil when compared to the HBC coil. To measure the mean SNR in the human brain (Table 3.2-b), ROI 6 was also chosen to cover the entire image. The obtained values were 21.1 for the HBC coil, 20.8 for the HSBC coil, 18.5 for the DH coil, and 29.4 for the ST coil; these values were 2% lower for the HSBC coil, 13% lower for the DH coil, and 39% higher for the ST coil when compared to the HBC coil.
In the human brain, five ROIs were additionally chosen to compare the mean SNR; these ROIs were circular in shape, and each contained 1100 pixels, as shown in Figure 3.11. The average mean SNR for the five ROIs was measured to be 82.6 for the HBC coil, 85.2 for the HSBC coil, 78.3 for the DH coil, and 104.5 for the ST coil. The relative SNR was 3% higher for the HSBC coil, 6% lower for the DH coil, and 23% higher for the ST coil when compared to the HBC coil.

3.3.4 Signal Intensity Profiles

For human brain imaging, the B_1 field homogeneity was compared using one-dimensional SI

profiles in axial slices along the L-R direction and sagittal slices along the superior-inferior (S-I) direction for the HBC coil (Figure 3.17-a), HSBC coil (Figure 3.17-b), DH coil (Figure 3.17-c), and ST coil (Figure 3.17-d) as shown in Figure 3.17.

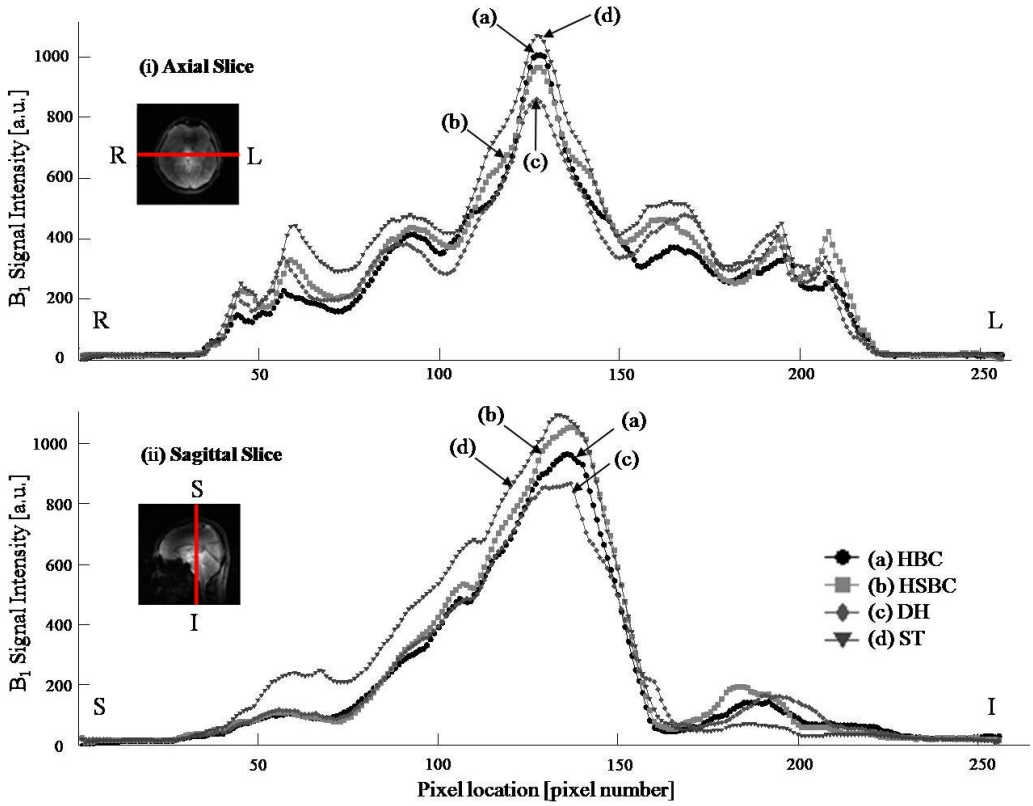

Figure 3.17: B_1 signal intensity profiles of human brain for four CP volume coils

On a central axial slice along the L-R direction, the ST coil had higher B_1 SI in the peripheral region when compared to the other coils, as shown in Figure 3.17-i. Furthermore, the DH coil had a low B_1 SI for the overall profile in the central as well as peripheral pixel locations. On a central sagittal slice along the S-I direction, all coils had a similar B_1 SI profile in the superior part of the human brain except for the ST coil, as shown in Figure 3.17-ii.

The B_1 homogeneity was express as distance between maximum and 66% location from the one-dimensional SI profile illustrated in Figure 3.17, and compared for four CP volume coils as shown in Table 3.3. On an axial slice along the L-R direction (Table 3.3-i), the homogeneity range was converted into distance and was 79.1 mm for the HBC coil, 113.2 mm for the HSBC coil, 121.0 mm for the DH coil, and 119.1 mm for the ST coil. The distance was 43% higher for the HSBC coil, 52% higher for the DH coil, and 50% higher for the ST coil relative to the HBC coil. On a central sagittal slice along the S-I direction (Table 3.3-ii), the distance was 3% higher for the HSBC coil, 5% higher for the DH coil, and 21% higher for the ST coil relative to the HBC coil. On a coronal image along the L-R direction (Table 3.3-iii),

the distance was 7% higher for the HSBC coil, 11% lower for the DH coil, and 10% higher for the ST coil relative to the HBC coil.

Table 3.3: B_1 field homogeneity converted to distances in the human brain

CP Coils	Distance [mm] (relative ratio to HBC)		
	Imaging Slice		
	(i) Axial	(ii) Sagittal	(iii) Coronal
HBC	79.1 (1.00)	98.6 (1.00)	139.6 (1.00)
HSBC	113.2 (1.43)	102.5 (1.03)	149.4 (1.07)
DH	121.0 (1.52)	104.4 (1.05)	125.0 (0.89)
ST	119.1 (1.50)	120.1 (1.21)	154.2 (1.10)

3.3.5 Signal Homogeneity in Two-Dimensional Image

For a quantitative comparison of the B_1 field homogeneity, the number of pixels between the maximum B_1 SI and 66.6% of the maximum was counted and compared on two-dimensional GRE images for the phantom and human brain in axial, sagittal, and coronal slices as shown in Figure 3.18.

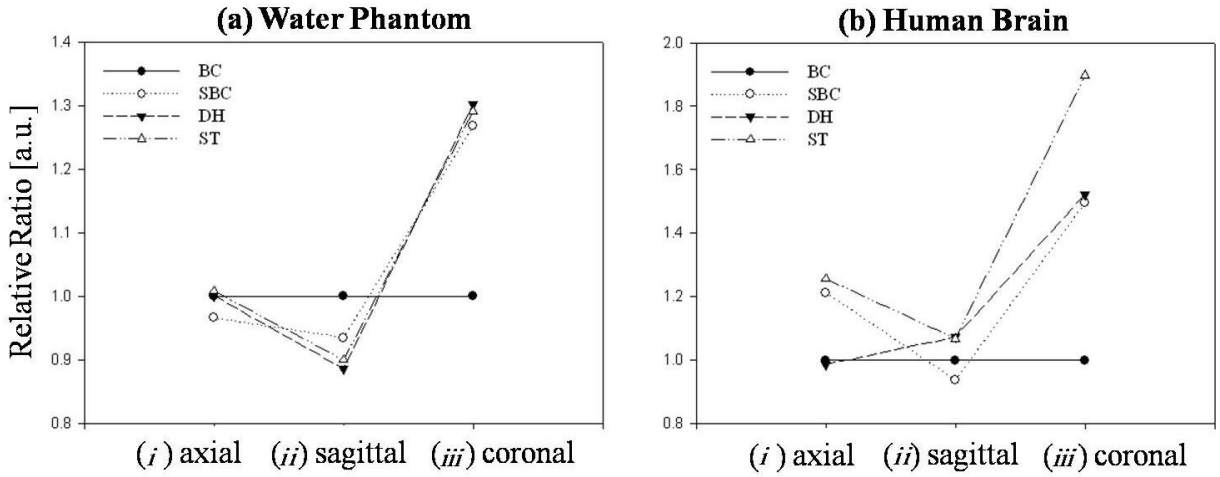

Figure 3.18: Relative ratio to the HBC coil for signal intensity

The relative ratio to the HBC (solid line) coil was expressed for the SBC (dotted line), DH (dashed line), and ST coils (dashed dotted line). The number of pixels corresponding to uniformity between the maximum B_1 SI and 66.6% on the axial GRE images for the phantom (Figure 3.18-a) out of a total of 65 536 pixels was 17 154 pixels for the HBC coil, 16 574

pixels for the HSBC coil, 17 174 pixels for the DH coil, and 17 299 pixels for the ST coil. The relative number of pixels was 4% lower for the HSBC coil when compared to the HBC coil. The counted numbers of pixels for the DH and ST coils were similar to that of the HBC coil (Figure 3.18-a, i). For sagittal GRE images of the phantom, the measured number of pixels was 7% lower for the HSBC coil, 12% lower for the DH coil, and 10% lower for the ST coil relative to the HBC coil (Figure 3.18-a, ii). All coils had a lower number of counted pixels when compared to the HBC coil. On a coronal GRE image of the phantom, a greater number of pixels was counted for all three coils: 26% higher for the HSBC coil, 30% higher for the DH coil, and 29% higher for the ST coil relative to the HBC coil (Figure 3.18-a, iii). On axial GRE images of the human brain (Figure 3.18-b), the counted number of pixels was 16 204 pixels for the HBC coil, 19 664 pixels for the HSBC coil, 15 992 pixels for the DH coil and 20 356 pixels for the ST coil out of a total of 65536 pixels. The relative ratio was 21% higher for the HSBC coil, 2% lower for the DH coil, and 25% higher for the ST coil when compared to the HBC coil (Figure 3.18-b, i). On sagittal GRE images of the human brain, the counted number of pixels was 13 946 pixels for the HBC coil, 13 081 pixels for the HSBC coil, 14 970 pixels for the DH coil, and 14 904 pixels for the ST coil. The relative ratio was 7% lower for the HSBC coil, 7% higher for the DH coil and 6% higher for the ST coil when compared to the HBC coil (Figure 3.18-b, ii). On coronal images of the human brain, the counted number of pixels was 6860 pixels for the HBC coil, 10 276 pixels for the HSBC coil, 10 451 pixels for the DH coil, and 13 025 pixels for the ST coil. The relative ratio was 49% higher for the HSBC coil, 52% higher for the DH coil, and 89% higher for the ST coil when compared to the HBC coil (Figure 3.18-b, iii).

3.3.6 Maps of Effective Flip Angle

The two-dimensional seven-pixel medial filtered effective FA α_{eff} maps for the given FA α_{giv} (= 50°) in the phantom (top row) and human brain (bottom row) are shown in Figure 3.19. The FA maps for all slices of the phantom (Figure 3.19-i) and human brain (Figure 3.19-ii) displayed a field pattern focused around the center compared to the peripheral region. For the human brain in particular, the FA map of the ST coil produced a symmetric distribution, and the B_1^+ homogeneity was more focused around the center for each slice compared to that of all of the other coils. When explored in more detail, the B_1^+ homogeneity was asymmetric on an axial slice along the L-R direction of the bottom for the HBC, HSBC, and DH coils when

compared to the ST coil.

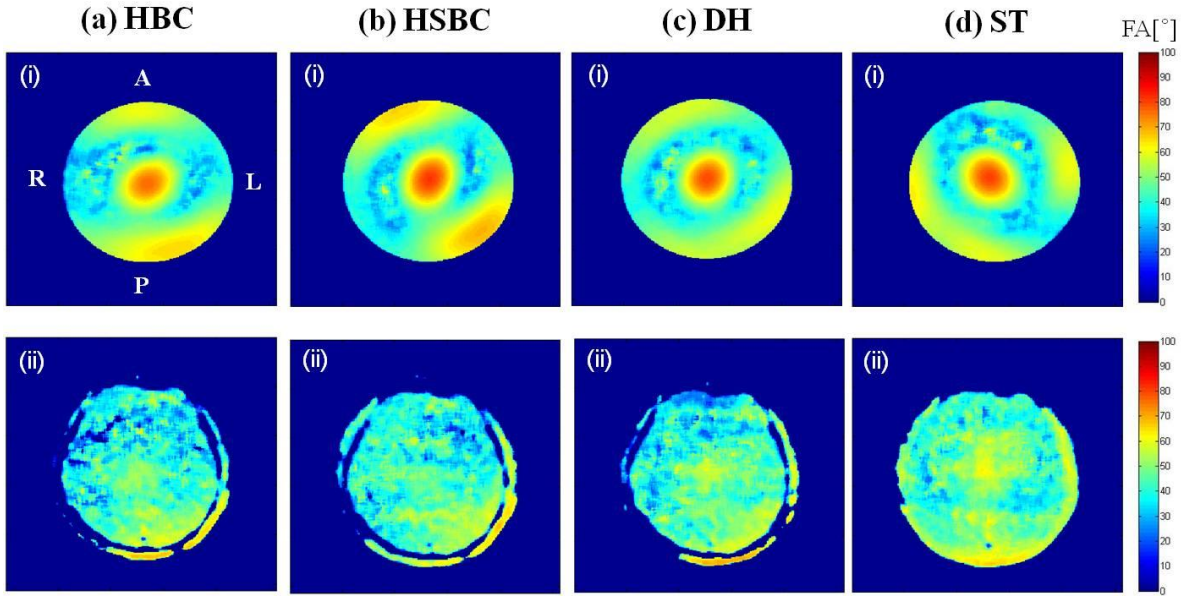

Figure 3.19: Effective FA maps for the α_{giv} (= 50°) in the (i) phantom and (ii) human brain

3.3.7 Measurement of Averaged Effective Flip Angle Value

The average α_{eff} obtained for the axial, sagittal, and coronal slices from the phantom and human brain was compared according to different ROIs (in Figure 3.10) and is described in Table 3.4. The number of total pixels was 66 536 and measured from an imaged FOV (256 × 256).

On an axial slice for the phantom (Table 3.4-a), approximately 1200 out of 65 536 pixels were chosen in ROI (Figure 3.10-a, i), which displayed a brighter image when compared to the other ROIs. In other regions, approximately 5000 pixels in ROI (Figure 3.10-a, ii), 10 000 pixels in ROI (Figure 3.10-a, iii), and 20 000 pixels in ROI (Figure 3.10-a, iv) were chosen for comparison.

The α_{eff} for α_{giv} (50°) in ROI (Table 3.4-a, i) was 18.8° higher for the HBC coil, 21.4° higher for the HSBC coil, and 19.9° higher for the DH and ST coils. The α_{eff} obtained average value was 37%–42% higher when compared to the FA for all coils. α_{eff} in ROI (Table 3.4-a, ii) was 4.36° higher for the HBC coil, 6.1° higher for the HSBC coil, 3.85° higher for the DH coil, and 4.97° higher for the ST coil. After verifying the slight variation for each coil, the difference in maximum α_{eff} among the four coils was found to be 1.8°. In contrast to ROI (Table 3.4-a, i) and ROI (Table 3.4-a, ii), α_{eff} for ROI (Table 3.4-a, iii) and ROI (Table 3.4-a,

iv) was measured to be -4.0° to -0.9° compared to the FA.

On an axial slice of the human brain (Table 3.4-b), approximately 1750 pixels in ROI (Table 3.4-b, i), 7000 pixels in ROI (Table 3.4-b, ii), 14 000 pixels in ROI (Table 3.4-b, iii), and 26 000 pixels in ROI (Table 3.4-b, iv) were chosen to compare α_{eff}. α_{eff} was 3.8° higher for the HBC coil, 8.5° higher for the HSBC coil, 5.8° higher for the DH coil, and 14.0° higher for the ST coil of ROI (Table 3.4-b, i). α_{eff} was 4.0° lower for the HBC coil, 0.5° lower for the HSBC coil, 4.1° lower for the DH coil and 0.2° higher for the ST coil of ROI (Table 3.4-b, ii). α_{eff} was 3.5° lower for the HBC coil, 2.0° lower for the HSBC coil, 6.3° lower for the DH coil, and 3.9° lower for the ST coil of ROI (Table 3.4-b, iii). α_{eff} for the ROI (Table 3.4-b, iv) region was contained in an error range of 2%.

Table 3.4: Measurement of averaged effective FA value according to different ROIs (*i–iv*) in the (a) phantom and (b) human brain

CP Coils	(a) Phantom											
	Axial				Sagittal				Coronal			
	i	ii	iii	iv	i	ii	iii	iv	i	ii	iii	iv
HBC	68.80	54.36	47.74	48.17	69.37	55.51	50.51	50.07	70.64	59.65	58.98	54.78
HSBC	71.44	56.10	47.68	49.07	74.77	62.43	53.70	50.62	73.99	64.29	56.16	52.47
DH	69.96	53.85	45.94	47.51	79.41	64.85	54.06	50.96	78.56	66.15	56.72	52.94
ST	69.90	54.97	46.58	47.40	75.72	60.49	54.31	51.29	74.90	63.92	53.11	51.13

CP Coils	(b) Human brain											
	Axial				Sagittal				Coronal			
	i	ii	iii	iv	i	ii	iii	iv	i	ii	iii	iv
HBC	53.88	45.98	46.45	51.36	53.73	49.40	52.45	54.50	50.74	45.78	51.66	53.11
HSBC	58.52	49.43	47.94	50.96	57.30	51.63	51.57	52.48	52.94	48.33	54.03	53.81
DH	55.89	45.81	43.66	49.06	58.26	49.35	50.67	53.87	58.51	52.10	55.01	55.64
ST	64.03	50.27	46.08	49.89	62.65	54.42	49.63	51.92	59.15	51.68	50.98	51.39

The variation of B_1 field, SI, and B_1 field shape in the center as well as the periphery region still remained, due to the interaction between different coil structures and object. Although the B_1 field for all CP coils was distributed irregularly and produced restricted B_1 homogeneity, ST coil was more symmetrically distributed from the center region on an axial slice of the human head.

4 7T MULTI-CHANNEL TRANSMIT ARRAYS

In this chapter, the developed 16-element head-array was evaluated and compared with the eight-element Tx/Rx head-array at 7T.

4.1 Motivation

Multiple-element receive-only coil arrays [16] are widely used in MRI because they have higher reception sensitivity in extended FOV [97, 98] from relatively small coil elements compared to volume coils [99]. These coils are used to reduce scan time through PI acquisition. Several techniques have been suggested for parallel PI; differences involve using the Fourier or spatial domains to acquire the central matrix inversion [42]. Multiple-element receive arrays consist of a mutually decoupled multiple surface coil; they independently and simultaneously receive MR signals. Each element is then connected to each preamplifier and independent receiver channel of the MRI system. The major technical issues in multiple coil arrays are in reducing the mutual coupling between surface coils. To overcome this problem, several approaches have suggested overlapping techniques [100, 101] for adjacent coils and connecting non-overlapping coils to the low input impedance preamplifier [102, 103]. If there is mutual coupling in the multiple arrays, this decreases the image sensitivity and causes a power loss due to the double resonance phenomenon. Multiple receive coils are used in a variety of configurations to cover the desired FOV in terms of the surface or volume. In UHF MRI system, they are particularly used in head-related studies such as fMRI and other applications [104], as well as animal MR imaging [105].

In UHF MRI systems, more complex wave behavior and interaction between the RF coil and subject pose a challenge to *in-vivo* brain imaging. Despite efforts to use the classic approach of a quadrature CP volume coil to improve B_1 uniformity as compared to the linear polarized (LP) coil, the problem of B_1^+ inhomogeneity still remains. Several methods have been proposed to mitigate B_1^+ inhomogeneity using adiabatic pulses [106], spiral-shaped birdcage volume coils [36], post-image processing [107], and spectral-spatial RF pulses [108] More recently, multiport transmit using the pTx system for birdcage-type coils was proposed to improve the B_1 homogeneity using flexible special and temporal modulated RF excitation [50, 109, 110]. A homogeneous B_1 field can be approximately achieved by adjusting the magnitude and phase on each transmit channel of the pTx system. An application for a multi-element

transmit coil array in a pTx MRI system using transmit sensitivity encoding (SENSE) was suggested [111]. This technique shortens the duration of RF pulses of TR and TE and produces a low specific absorption ratio (SAR) [112] and improved B_1 homogeneity. Using a multi-element transmit coil array with B_1^+ shimming techniques [113, 114] substantially improves B_1 homogeneity, especially the B_1 transmit field, compared to conventional CP volume coils and receive-only coil array. However, significant challenges for multiple transmit arrays still remain in terms of the design and implementation of RF coils for dedicated transmit channels and their integration into existing pTx systems. Most transmit coil head-arrays at 7T were designed as eight separate Tx/Rx elements under cylindrical geometries [115].

This study was thus based on electromagnetic (EM) simulations and focused on the design of a 16-element head-array for available combined eight-channel and individual 16-channel excitation to result in an RF coil with a total of eight channels in the pTx system. The FA maps of an oil and water sphere phantom were acquired by using this prototype. The 16 individual FA maps and eight combined FA maps using the designed 16-element head-array were evaluated and compared with the eight-element Tx/Rx head-array at 7T. In order to access different CP modes sequentially, 16 × 16 Butler matrix network [116] were used for excitation of the available phase modes of the 16-element transmit coil array.

4.2 Material and Methods

4.2.1 Performance of the Parallel Transmit using FDTD Simulations

To verify B_1 field homogeneity, a finite difference time domain (FDTD) method for simulation of electromagnetic field distributions (xFDTD v6.3, Remcom, State College, PA) was used to simulate the time dependent magnetic and electric fields. The FDTD analysis has the advantage of simplicity and efficiency and is widely used to examine MRI RF coil fields. It is based on a grid-based time-domain numerical techniques. Maxwell's equation is solved directly in the partial differential form of the equation.

The general structure of the eight-element transmit head-array was modeled with a diameter of 270 mm and length of 150 mm (dimension of one element: horizontal length/ vertical length/ conductor width = 85 mm/ 150 mm/ 5 mm). It was simulated with the FDTD simulation program at 7T at a resonance frequency of 297.2 MHz, as shown in Figure 4.1.

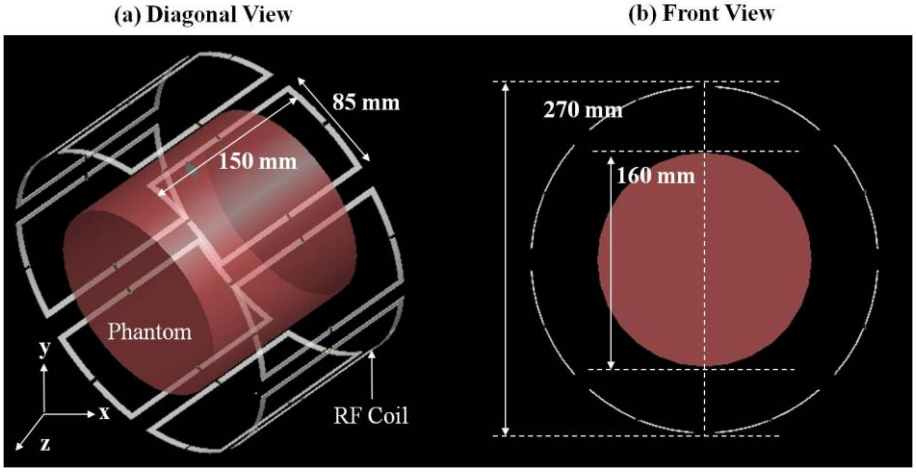

Figure 4.1: Eight-element transmit array modeled with FDTD

To explore the distribution resulting from excitation errors in amplitude and phase of each port, a cylindrical water phantom (diameter of 160 mm and length of 150 mm) was used. The electrical properties of phantom (σ = 0.55 *S/m* and ε_r = 51.89) based on the solution concentration of averaged gray (σ = 0.69 *S/m* and ε_r = 60.02) and white matter (σ = 0.41 *S/m* and ε_r = 43.77) in human brain. A three-dimensional mesh with 2.0 mm × 2.0 mm × 2.5 resolutions was created within a region of 60 × 60 × 60 cm^3. The calculation was performed with -60 dB convergence to ensure that the steady state was reached. The boundary condition using perfectly matched layer (PML) was used for the outer boundary truncation of the grid. Each coil element was modeled with infinitely thin perfect electrical conducting (PEC) wires, with four equally spaced lumped element capacitors and gap distance of 23 mm apart. The coil model was driven by 32 current sources at the location of the capacitors on each of the elements with a phase increment between elements of 45°.

Figure 4.2 shows that the B_1 maps had different distributions for amplitude errors only (Figure 4.2-b) or phase errors only (Figure 4.2-c) compared to the ideal case (Figure 4.2-a). Quantitative B_1^+ map (e.g. unit of μT/V in Figure 4.2-i), B_1^- map (in Figure 4.2-ii), signal distribution (in Figure 4.2-iii) was recalculated with home-built programs in MATLAB (The Mathworks, Natick, MA). The ideal case of phase and amplitude values (Figure 4.2-a) shows a symmetrical uniform B_1 signal distribution (Figure 4.2-a, iii) from the center to the peripheral region compared to cases of excitation errors. For the applied errors in amplitude (Figure 4.2-b) and phase (Figure 4.2-c), an inhomogeneous B_1 signal distribution is indicated. In other words, the inhomogeneous B_1 signal distribution was caused by improper amplitude and phase; the inhomogeneous B_1 distribution can be corrected by adjusting these two factors.

Therefore, a multi-element transmit array that allow independent adjustments of the phase and amplitude for individual ports will improve the RF homogeneity.

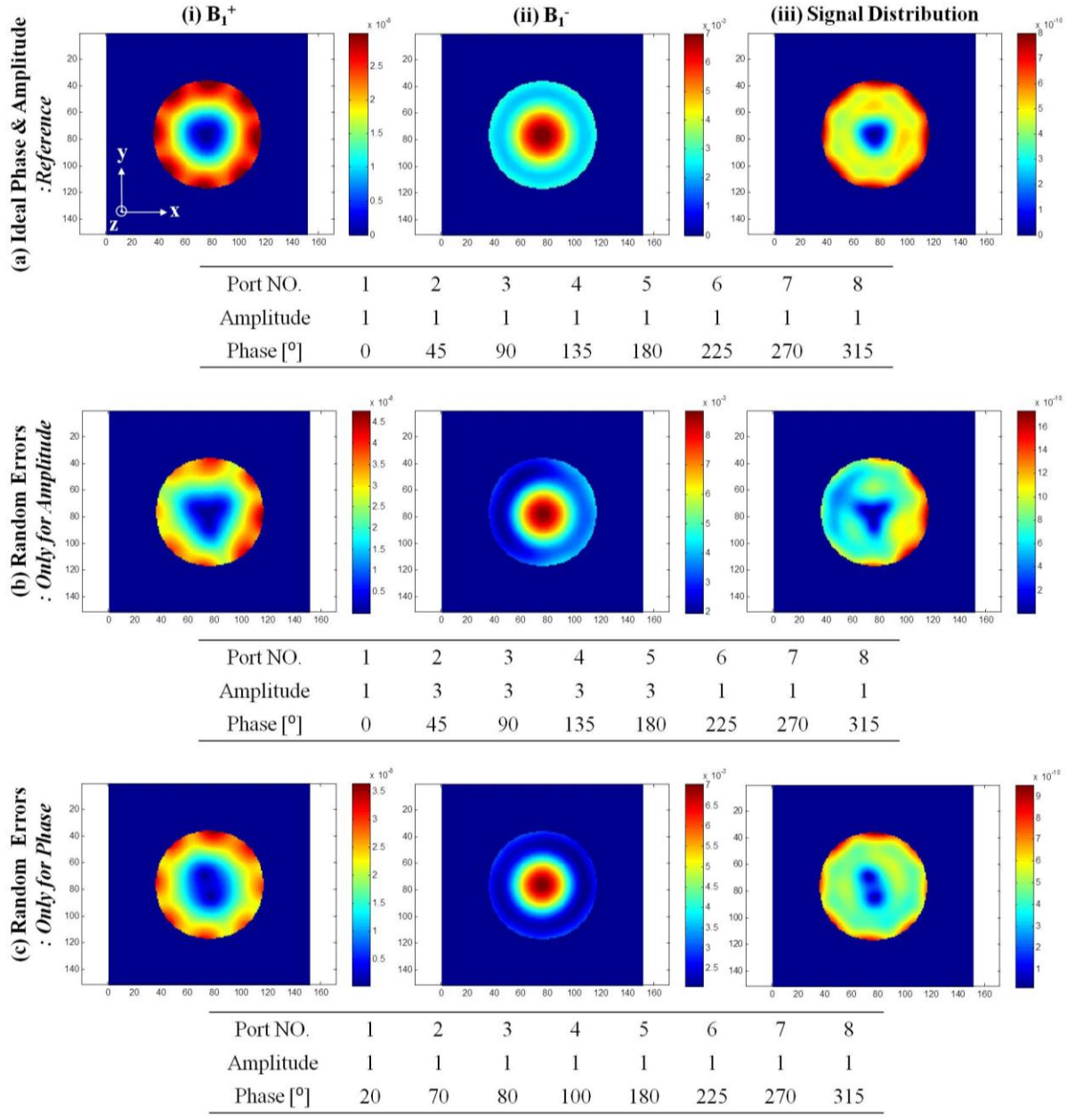

Port NO.	1	2	3	4	5	6	7	8
Amplitude	1	1	1	1	1	1	1	1
Phase [°]	0	45	90	135	180	225	270	315

Port NO.	1	2	3	4	5	6	7	8
Amplitude	1	3	3	3	3	1	1	1
Phase [°]	0	45	90	135	180	225	270	315

Port NO.	1	2	3	4	5	6	7	8
Amplitude	1	1	1	1	1	1	1	1
Phase [°]	20	70	80	100	180	225	270	315

Figure 4.2: B_1 field distribution according to errors in amplitude and phase excitation of eight-element transmit array

4.2.2 System Hardware

4.2.2.1 Configuration of Parallel Transmit System

The experiments were performed on a Siemens 7T whole-body system (Magnetom 7T, Siemens Healthcare, Erlangen, Germany) equipped with eight transmit (8 × 1 kW peak RF power) and 32 receive channels. The volume-shaped multiple element coil array consisted of eight independent elements, as shown in Figure 4.3.

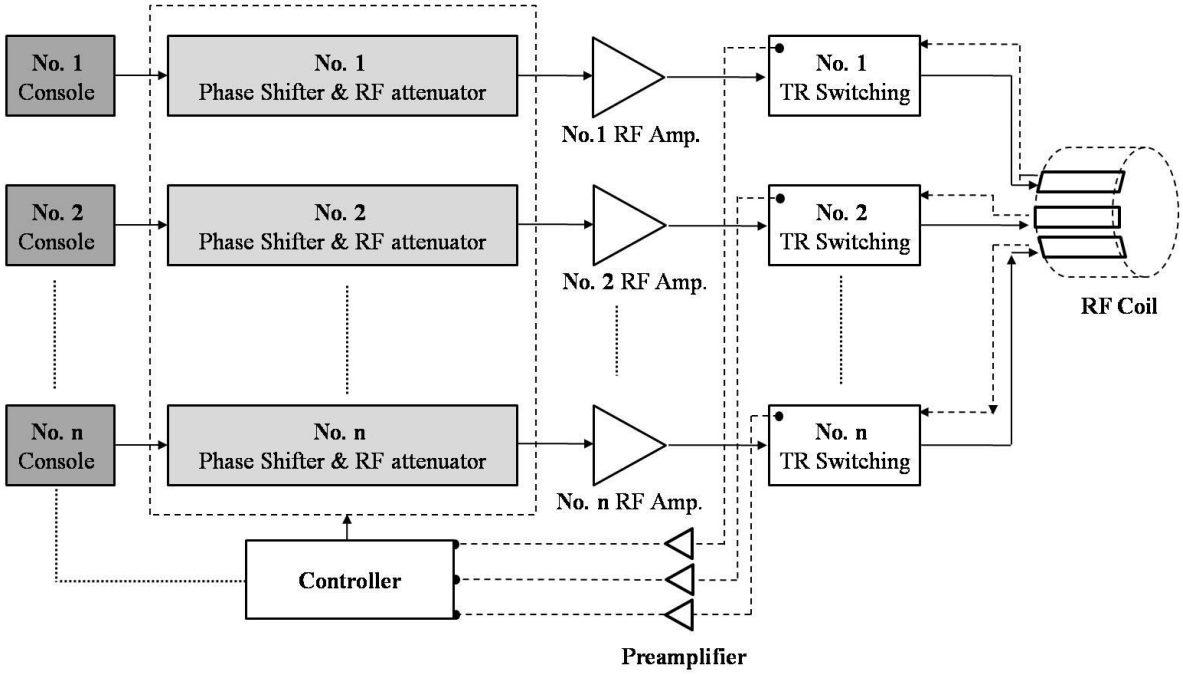

Figure 4.3: Configuration of the multi-channel parallel RF transmit system

The array was driven by eight independent RF current sources. The individually driven RF current sources (e.g., waveform, power, amplitude, and phase) make it possible to change and modify the amplitude as well as phase until a homogenous B_1 field is obtained. The initial excitation was applied and operated by each console to acquire the MR images. The MR image was reacquired with corrected factors using RF attenuation and phase shift calculated by the MR image obtained from the initial excitation. The RF surface coil using independent parallel sources can thus compensate the B_1 field non-uniformity.

4.2.2.2 **Variable Power Combiner using Butler Matrices**

A 16 × 16 Butler matrix network for the excitation of different phase modes was provided by working group of Solbach et al. [116]. The experimental 16 × 16 Butler matrix [54] is shown in Figure 4.4.

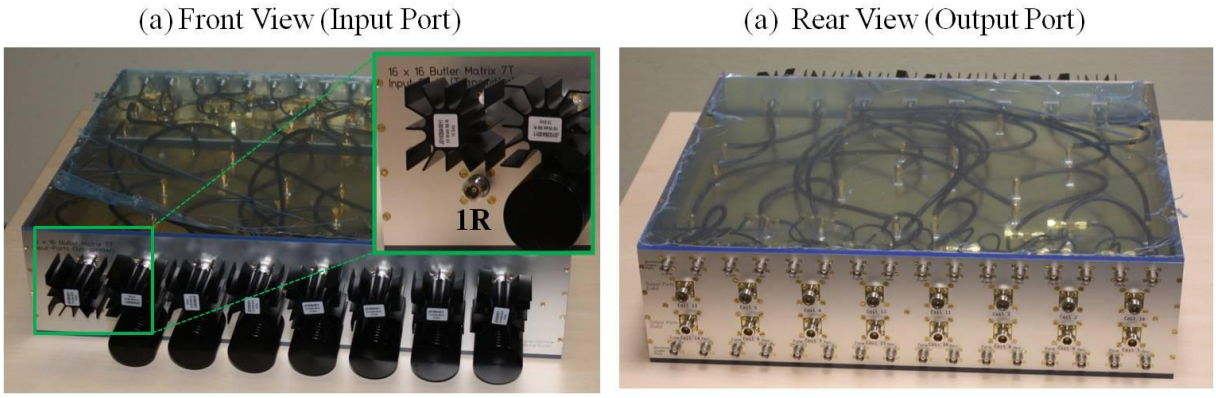

Figure 4.4: 16×16 Butler matrix for a 16-element transmit array

A 16 × 16 Butler matrix network was connected to the outputs of the 8×8 variable power combiner for pre-combination of the eight-driven power amplifiers [54], as shown in Figure 4.5.

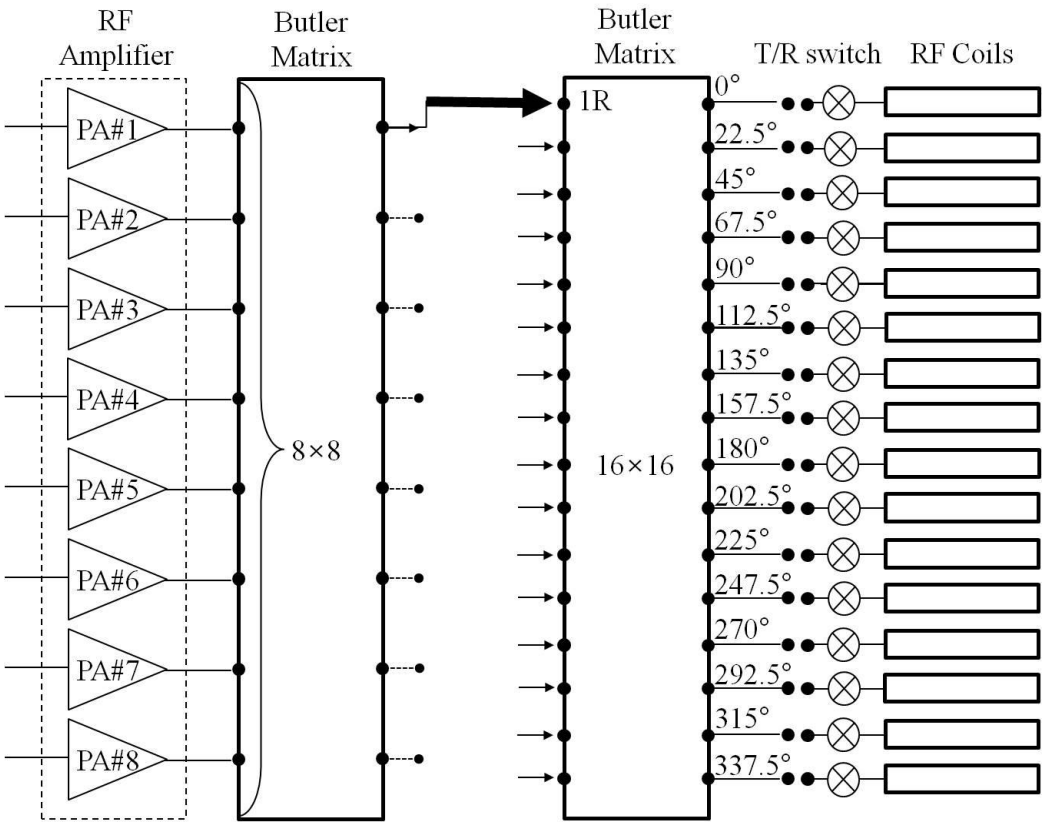

Figure 4.5: Block diagram of 8 × 8 and 16 × 16 Butler matrices for a 16-element array

The Butler matrix enables to access the general CP mode as well as higher-order CP modes with equal power ratios and different phases. Thus, 8 × 8 and 16 × 16 Butler matrices were implemented for operating the eight-driven pTx system and 16-element transmit array in a 7T MRI system. The Butler network consists of -3 dB hybrid couplers and variant phase shifters. Each input port produces a uniform-amplitude distribution on the outputs with a uniform phase difference across the output ports. To generate CP and another CP mode by using the 16-element transmit array, each element was connected to the output of the 16 × 16 Butler matrix. The output phase of a 16 × 16 Butler matrix with a linearly independent phase difference as shown in Figure 4.5.

4.2.3 Geometry Modeling and Magnetic Field Simulation

4.2.3.1 Eight-Element Array using the Biot–Savart approach

For visualization and analysis in free space of the magnetic field created by an eight-element square-shaped coil without loaded conditions, the Biot–Savart approach was adapted [117]. A square shape (vertical length/ variable horizontal length = 150 mm/ 10-100 mm) was centered at the origin of a coordinate system and was drawn for a geometry with 16 point divisions, as shown in Figure 4.6.

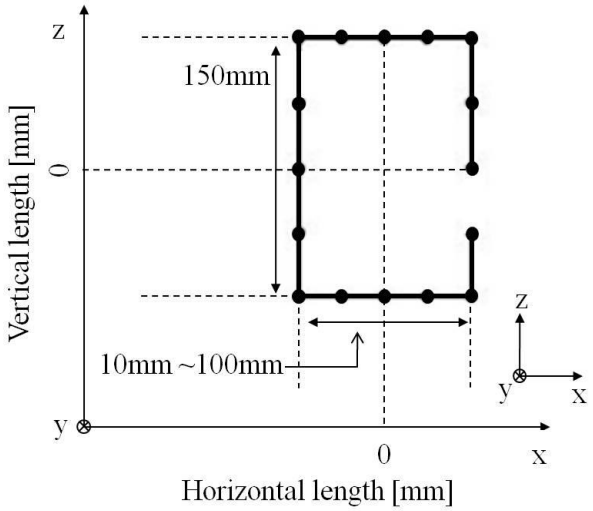

Figure 4.6: Single element coil consisting of 16-point functions

In other words, the eight-element array was modeled by a 128-point function. The current conductors were arranged in an eight-element array configuration with a cylindrical structure

having a diameter of 270 mm. The modeled geometry was a square shape with vertical length of 150 mm and variable horizontal length of 10-100 mm (intervals of 10 mm). The length along the *z*-direction of a single element coil was 150 mm to enable to cover the main parts of the human brain. The eight-element array coil was modeled as a non-overlapped geometry between each element.

In the given three-dimensional spatial distribution of the current on the RF array coil, Biot–Savart's law was used to calculate the magnetic field associated with the current distribution. The array coil simultaneously transmits and receives RF signals. The first element (element 1 in Figure 4.7) was positioned on the right side of the eight-element surface coil, as shown in Figure 4.7.

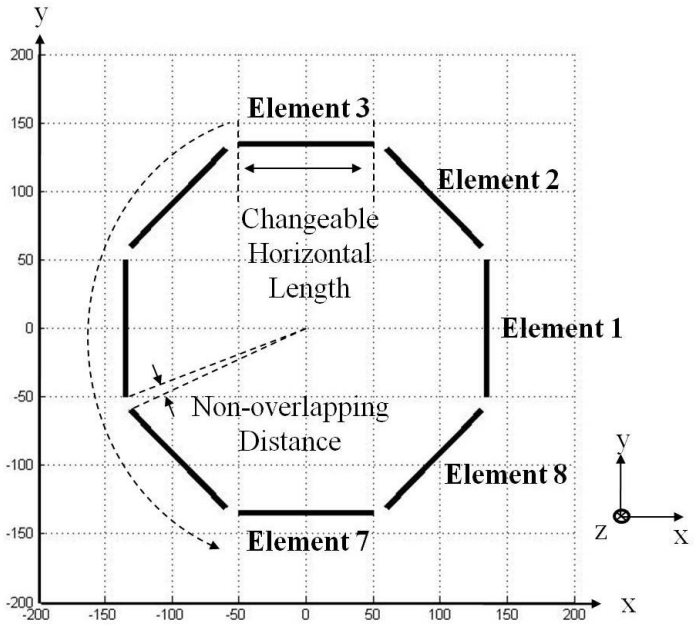

Figure 4.7: Top view of the counterclockwise eight-element transmit array

Figure 4.7 is the top view of the modeled eight-element array. As the horizontal width increases, the distance between each element decreases. The eight-element transmit array coil was positioned and rotated as circular shape. To determine the optimal geometry and evaluate B_1 sensitivity and homogeneity, the specific value was defined by using the maximum and mean signal divided by the SD value of the B_1 field created by variable horizontal widths.

4.2.3.2 **EM Simulation using CST MWS**

The multi-transmit array coils were modeled by using a computer simulation technology microwave studio (CST MWS, Darmstadt, Germany) tool. The simulation was performed in a joined project with J. Mallow. The array coils were designed using EM simulation software. CST MWS was used in conjunction with the water phantom (σ =0.99 *S/m* and ε_r =78) and the three-dimensional anatomical data set Hugo [118] to simulate the time-varying fields of an RF array; this array was loaded by a human section of the Hugo model. There is a difference in mesh cell sizes between eight-element and 16-element transmit array coils. The number of coil elements for a 16-element array is twice as large as that for an eight-element array; therefore, it was chosen for detail analysis as the cell size is greater. The eight-element and 16-element transmit array coils were simulated and compared under three conditions - free space, loaded water phantom, and Hugo head model - for a detailed investigation of B_1^+ field, and SAR distribution. Comparisons and evaluations were performed after tuning for the return loss below -30 dB. Two array coils were modeled without loaded conditions, as shown in Figure 4.8.

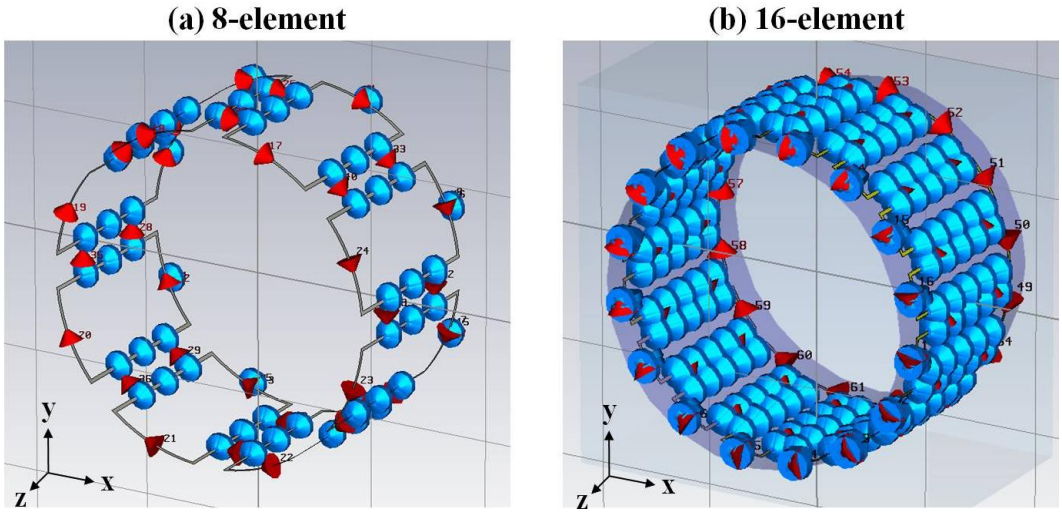

Figure 4.8: Geometric models of the (a) eight-element and (b) 16-element transmit arrays with CST MWS

The calculation volume was set to open boundaries with PML layers. For EM simulation using CST MWS, the mesh definition has a significant influence on the representation of areas including ports and lumped elements [119]. Eight and sixteen discrete RF ports were defined with adjustable impedance and lumped capacitance in parallel for better matching when loaded with the spherical water phantom (diameter of 160 mm) and Hugo brain model.

The water phantom was located in the iso-center inside the transmit array coils. Simulated total B_1 field raw data were extracted from CST MWS and recalculated to achieve positive B_1 component [120].

4.2.4 SAR Calculation using CST MWS

The design of the 16-element transmit array was evaluated for a static magnetic flux strength of 7T, In order to keep below the specified limit for SAR by the Food and Drug Administration (FDA). SAR calculation was conducted with a Hugo model using CST MWS. The absorbed RF energy in tissue from SAR is given by

$$SAR = \frac{\sigma \left| \overline{E} \right|^2}{2\rho'} \qquad [4.1]$$

where ρ' is the density of mass and σ is the electric conductivity. Excess absorbed energy and inhomogeneous RF can increase tissue temperature. The accumulation of high temperature in the tissue of subject can lead to RF burns. The energy was defined by the absorbed power and the mass of the subject. SAR depends on the strength of the external magnetic field, radius *r* of patient, and flip angle α as well as the duty cycle ΔD [121].

$$SAR \propto \sigma \cdot \alpha \cdot r^2 \cdot B_0^2 \cdot \Delta D \qquad [4.2]$$

The limitations for the mass-averaged SAR (typically 1 or 10 g) are defined by guidelines and standards specifying SAR safety limits (i.e., International Commission on Non-ionizing Radiation Protection (ICNIRP), Institute of Electrical and Electronics Engineers (IEEE), European Committee for Electrotechnical Standardization (Cenelec)) [122]. The maximum mass-averaged SAR is defined by each country as 1.6 W/kg averaged over 1 g of tissue and 2.0 W/kg averaged over 10 g of tissue. The simulated B_1 field using the Hugo brain model was evaluated through the RF power absorbed in 10 g of tissue for predicting and evaluating the SAR.

4.2.5 Design of RF Coils and Circuitry

4.2.5.1 Multi-channel Tx Arrays

Two versions of the transmit head-arrays were placed on acrylic formers with a diameter of 270 mm and length of 300 mm. The transmit array coils were made from polyimide PC board material and tuned *in-situ* to 297.2 MHz on the phantom. Each array was designed without overlap geometry, as shown in Table 4.1

Table 4.1: Dimensions of Tx-array coils

Dimensions of Tx-array Coil	(a) Eight-element [mm]	(b)16-element [mm]
Coil electrical diameter	270	270
Horizontal length	80	39
Vertical length	150	150
Distance between each elements	23	14

The non-overlapping distance between neighboring elements for reducing crosstalk was fixed as 14 mm for the 16-element array and 23 mm for the eight-element array. Figure 4.9 shows the configuration of the receive system from the surface coil to the preamplifier.

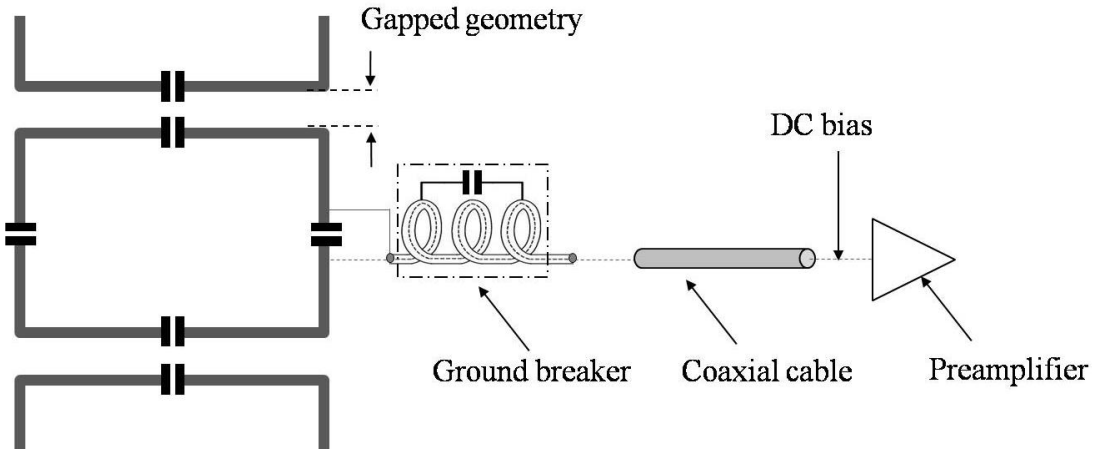

Figure 4.9: Configuration of RF receive system

All outputs of the receive coils were connected to low input impedance preamplifiers (1.5 T preamplifiers modified for use at 297.2 MHz, Siemens Medical Solutions, input impedance < 3 Ohm, noise figure < 0.5 dB, and gain of 26 dB) to reduce coupling between non-adjacent coils. The coaxial cable length for feeding was designed as the $\lambda/4$ transformation.

Figure 4.10 shows the optimized capacitance for each element at a resonance frequency of 297.2MHz.

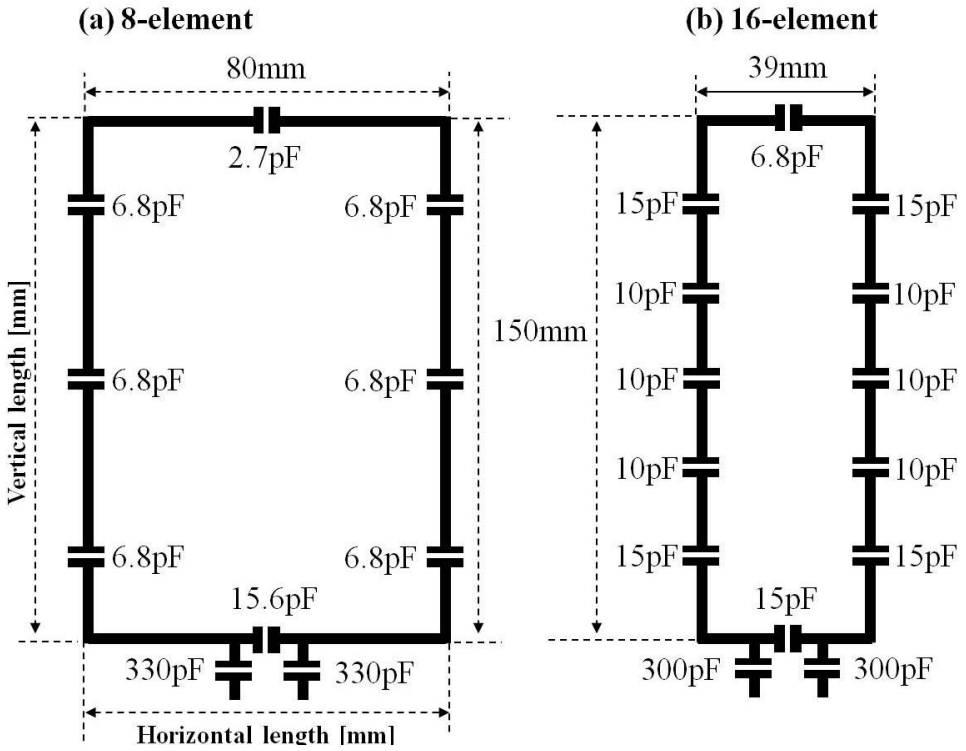

Figure 4.10: Capacitance of transmit arrays at 297.2 MHz

4.2.5.2 **Design of Power Divider, T/R Switches, and Phase Shifter**

Other RF circuits such as Tx/Rx switches and a phase shifter are needed for RF excitation and reception of the transmit array coils in a 7T MRI system. Especially for the 16-element array, a two-way power splitter has to be provided to match conditions between the number of applied eight-driven RF amplifiers and the output port of the 16-element array coil. The most important characteristics of a reciprocal power splitter are the split ratio, isolation, insertion loss, matching, and phase balance [123]. The efficiency of the power split ratio was optimized as the ratio of power in the output ports when all ports were terminated by 50 Ohm terminations to reduce reflection. Isolation was calculated as the ratio of power between the output ports (for divider) and input ports (for combiner). The isolation characteristic depends on the structure of the device, manufacture tolerances, and losses. The two-way Wilkinson power splitter was provided for a 16-element transmit coil array. It provides a -3 dB split with no phase shift. Figure 4.11 shows the lumped element versions of the Wilkinson power divider [124].

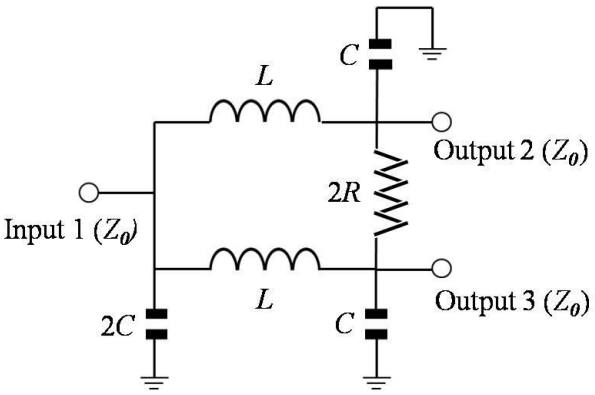

Figure 4.11: Schematic circuit of the Wilkinson power divider [124]

For lumped element Wilkinson power, the two output ports are connected with 2 × Z_0 (50 Ohm). The inductance L and capacitance C are given by

$$L = R/(\sqrt{2}\pi f) \quad [4.3]$$

$$C = 1/(2\sqrt{2}\pi fR) \quad [4.4]$$

From Equations [4.3] and [4.4], L and C were calculated to be 37.51 nH and 7.5 pF. Using these values, the Wilkinson power divider was modeled and optimized at a center frequency of 297.2 MHz and simulated using Ansoft Serenade v8.5, as shown in Figure 4.12.

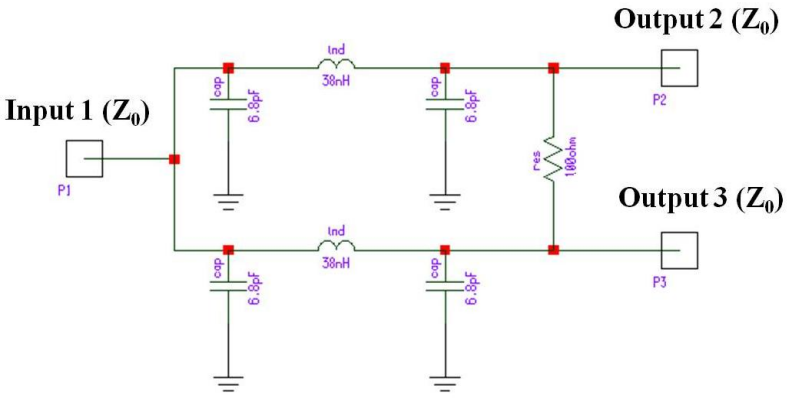

Figure 4.12: Lumped element version of the Wilkinson power divider for circuit simulation

The differences in values calculated from Equation [4.3] and [4.4] from the simulated data are shaded. The optimized values using the circuit simulation tool were 38 nH and 6.8 pF. Figure 4.13 shows the frequency response of an equal-split Wilkinson power divider.

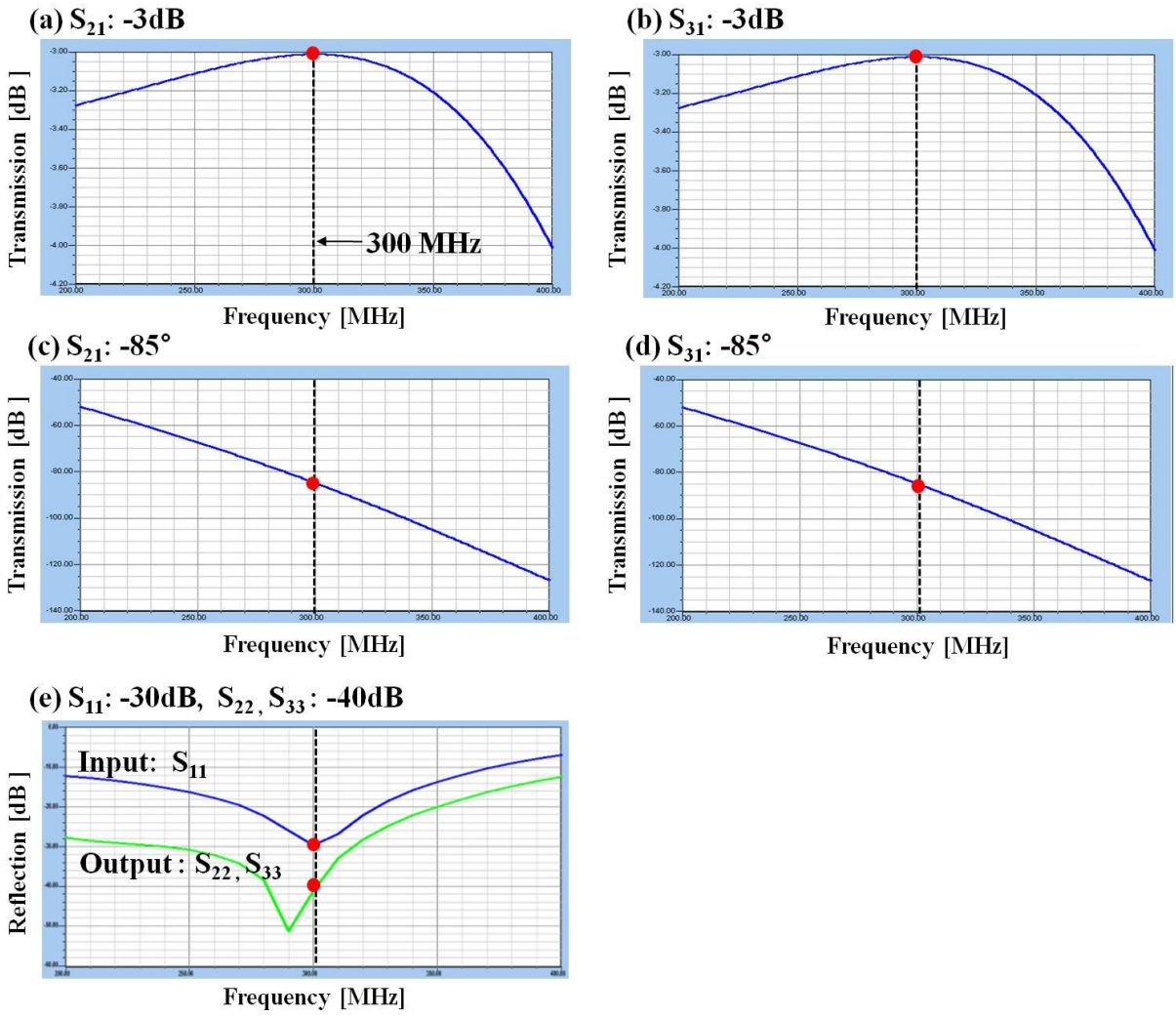

Figure 4.13: Frequency response of an equal-split Wilkinson power divider

The Wilkinson power splitter provided a -3 dB power split (Figure 4.13-a, -b) with no phase shift (Figure 4.13-c, -d). The phase shift S_{21} (-85° in Figure 4.13-c) was identical to S_{31} (-85° in Figure 4.13-d). Therefore, there was no phase difference between S_{21} and S_{31}. The reflection coefficients for the input (S_{11}) and output ports (S_{22}, S_{33}) were measured to be -31 and -42 dB (Figure 4.13-e), respectively.

For separate operations in the Tx and Rx states, Tx/Rx switches were designed with lumped elements. This should minimize the insertion loss inside the circuit as well as the phase difference for each Tx/Rx switch. The modeled Tx/Rx switches were controlled by the PIN diode, as shown in Figure 4.14.

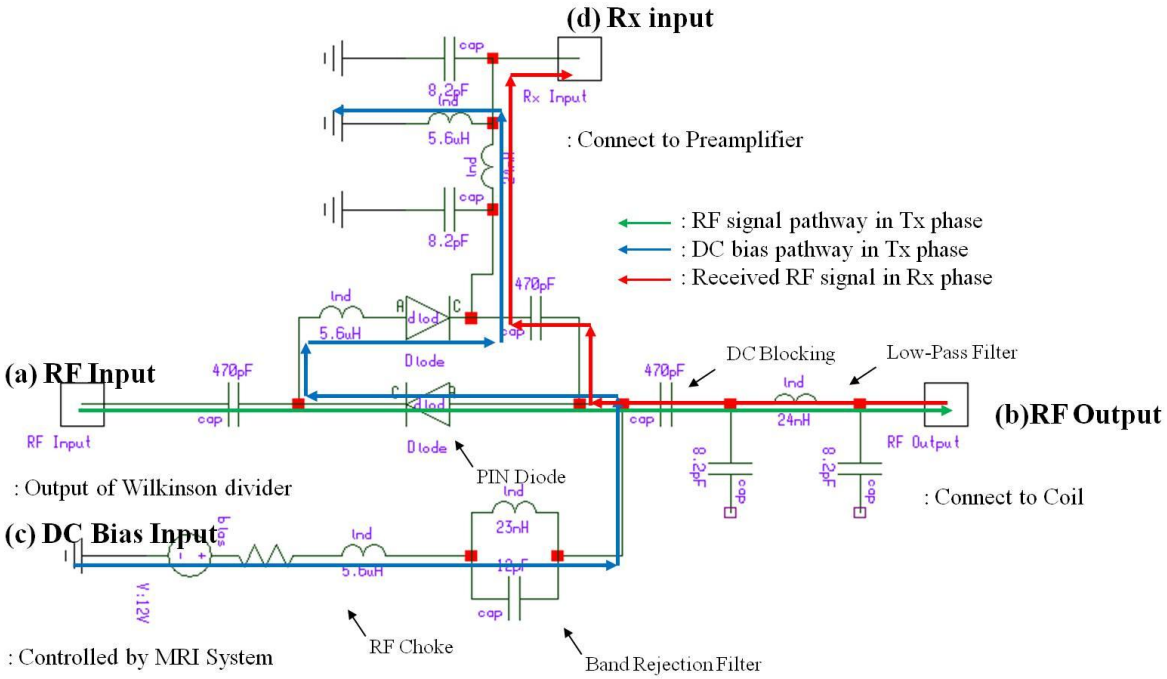

Figure 4.14: RF and DC signal pathways of the Tx/Rx switching circuit

In the Tx state, the external DC bias (+10V / 100mA) is controlled by selected MRI sequence (Figure 4.14-c) and turns on the PIN diode. As a result, the RF power signal comes from the linear power amplifier with the 1 kW continuous waveform (CW) of the pTx system and is delivered from (Figure 4.14-a) the output of the Wilkinson divider to (Figure 4.14Figure -b) each element of the transmit arrays. The final RF signal is supplied to create a B_1 field in each element of the transmit coil array. To suppress RF leakage, LPF and BRF were designed with insertion losses of -30 dB. The PIN diode (Macom MA4P4002B-402, Lowell, MA, USA) was used for high power capability.

In the Rx state, turning the PIN diode off is also controlled by DC bias (-30 V) of the MRI system. The received RF signal goes to Rx input port (Figure 4.14-d). It is connected to a low noise preamplifier (preamplifier's gain: ~30 dB). The crosstalk or isolation between RF input port (Figure 4.14-a) and Rx input port (Figure 4.14-d) is the critical parameter due to the very long recovery time of the pre-amplifier after input overload. Thus, the RF choke (i.e., 5.6 μH) is used to block the RF signal in the DC path. On the other hand, a high capacitance (i.e., 2700 pF) is used for DC blocking in the RF path.

For operation in CP mode, a phase-shifting method [125] was chosen with different lengths of RG 316 non-magnetic coaxial cable. Insertion of the external cable length (ℓ_{ext}) causes a phase change ($\Delta\phi$) in a signal as it propagates through a transmission line, as shown in Figure 4.15.

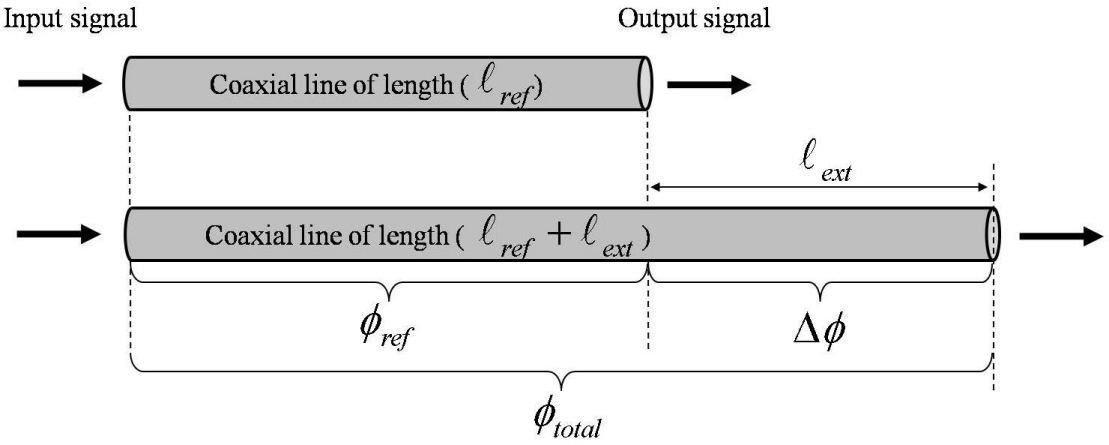

Figure 4.15: Phase difference through an external cable length [125]

The total expected phase change ($\Delta\phi$) is calculated by

$$\Delta\phi = \phi_{total} - \phi_{ref} = 3.6 \cdot 10^4 \cdot \frac{f \cdot \ell_{ext}}{c \cdot VF} \qquad [4.5]$$

where $\Delta\phi$ is the insertion phase change from the reference. ϕ_{ref} is the initial reference insertion phase. The f is the measured frequency in Hz, the c is the velocity of light in a vacuum ($3 \cdot 10^8$ m/sec), and VF is the velocity factor of the propagation in the coaxial cable.

$$VF = \frac{1}{\sqrt{\varepsilon_r}} \qquad [4.6]$$

The initial total insertion phase is used as a baseline phase reference for calculating the phase change. It is subtracted from subsequent measurements to obtain the phase change at each frequency. For an eight-element transmit array coil, the external cable length (ℓ_{ext}) for a 45° phase difference is 90.6 mm, and different cables are connected to each element, as shown in Figure 4.16. For the 16-element transmit array, the RG 316 coaxial cable was used, and 45.3 mm (half the length of 90.6 mm corresponding to 45°) was chosen for the 22.5° phase difference.

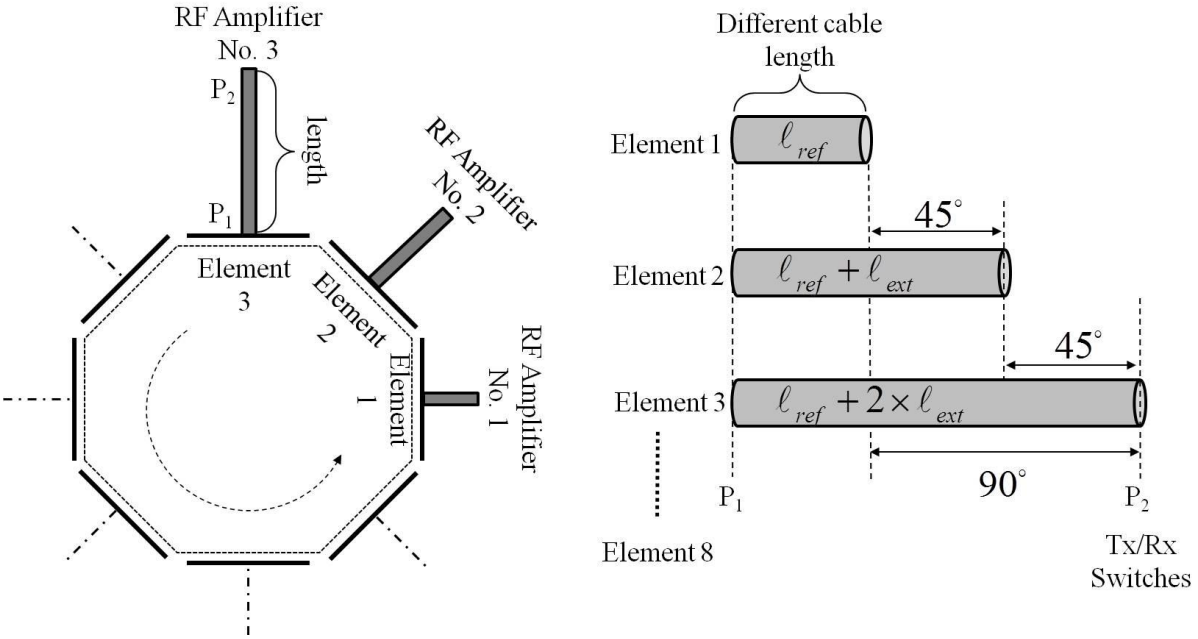

Figure 4.16: Different cable lengths of eight-element transmit array coil for CP mode

4.2.6 Phantom Studies

The experiments were performed on a 7T whole-body MRI system (Magnetom, Siemens Healthcare, Erlangen, Germany) equipped with an eight-driven pTx system and 32 receive channels. The 16-element and eight-element transmit head-array coil were compared by using a saturated turbo flash sequence (TR/TE = 1000 ms/1.9 ms and rectangular-shaped saturation pulse of 700-µs duration) to evaluate the FA map. FA maps for two transmit coil arrays were compared with an oil phantom (diameter of 170 mm, gadolinium), as shown in Figure 4.17-a, and a water phantom (diameter of 170 mm, distilled water solution consisting of 8.2 g $NaC_2H_3O_2$ and 6.9 g $C_3H_3O_3Li$ per 1000 g H_20), as shown in Figure 4.17-b, for individual and combined coil elements in the 7T eight-driven pTx MRI system.

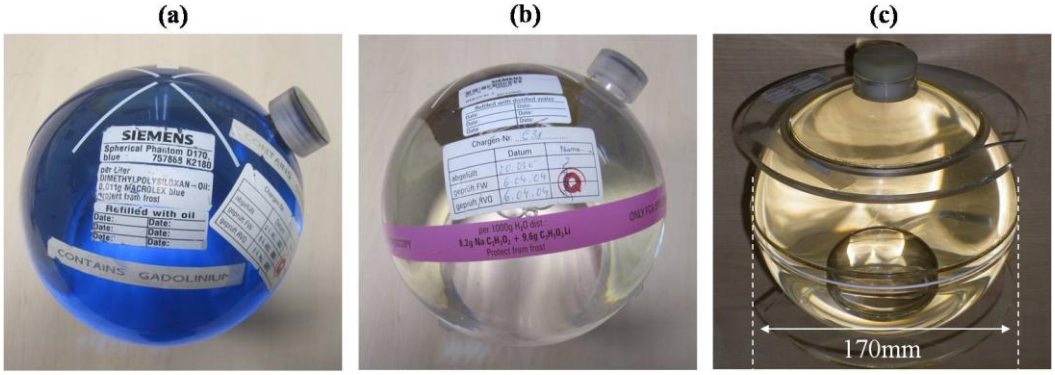

Figure 4.17: Spherical phantoms: (a) oil, (b) water, and (c) sugar dissolved in water

For higher B_1 homogeneity, a 16-element transmit array coil was examined by using a GRE image (TR/TE/α =100 ms/10 ms/25°) to compare the SNR and B_1 field of a spherical water phantom with that of a mixed sugar-water phantom (diameter of 170 mm, $\varepsilon_r = 45.20$, $\sigma = 0.87$: water 38.05%, sugar 56.05%, salt 5.9%); this phantom was chosen as its permittivity and conductivity are comparable to human brain tissue as shown in Figure 4.17 -c.

4.2.6.1 **Maps of Effective Flip Angle**

An approach to B_1^+ characterization of eight-element and 16-element transmit array coils involves 16 individual FA maps as well as eight combined FA maps; two elements are excited in order to compare FA maps. The B_1^+ maps of the oil and water sphere phantoms were obtained with the actual flip-angle imaging (AFI) sequences [126] including the spoiling improvements, provided by vendor (Siemens). The AFI pulse sequence consisted of two identical RF pulses using two delays of different durations ($TR_1 < TR_2$). After each pulse, a GRE signal was acquired as shown in Figure 4.18.

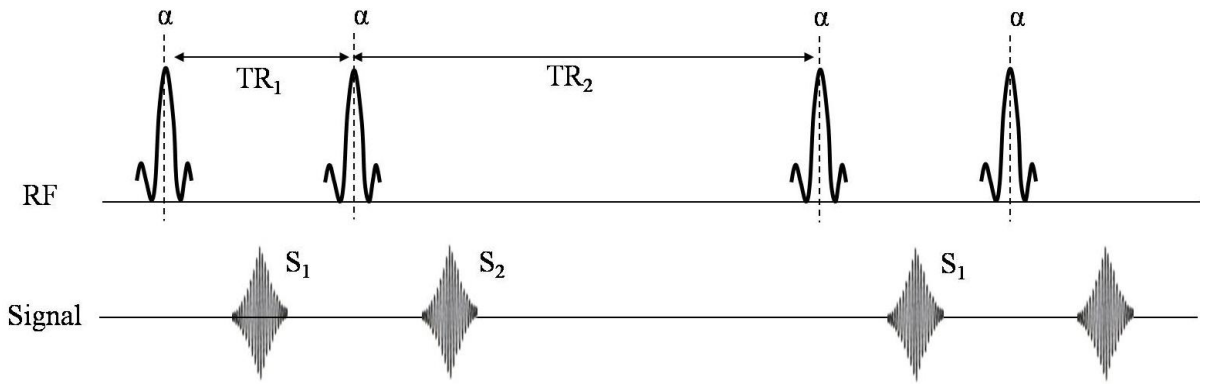

Figure 4.18: Timing diagram of the AFI sequence

The AFI sequence allows fast three-dimensional implementation and accurate B_1 measurement. The ratio (S_2/S_1) from signal intervals TR_1 and TR_2 was acquired:

$$\text{Ratio}= \quad S_2 / S_1 \approx \frac{1+n\cos\alpha}{n+\cos\alpha} \qquad [4.7]$$

where n is TR_2/TR_1. If delays between TR_1 and TR_2 are very short, transverse magnetization is perfectly spoiled. The FA α given by

$$\alpha \approx arc\cos\frac{(S_2/S_1)n-1}{n-(S_2/S_1)} \quad [4.8]$$

This is an advanced method for acquiring the FA maps because there are unnecessary long relaxation delays between sequence repetitions. The applied AFI sequence was applied with 2.56 ms sinc pulse, $TR_1/TR_2 = 50$ ms/150 ms, 6 mm isotropic resolution with a 64 × 64 × 32 matrix. Thus, the whole set of AFI acquisitions took 6 min for each element. The FA maps for combined eight-element and individual 16-element using 16-element transmit array coil were compared with general structure of eight-element array coil. FA maps were calculated in terms of the magnitude through the least squares method.

4.2.6.2 **SNR Maps and Mean SNR measurement**

The 16-element transmit head-array was connected to an 8 × 8 variable pre-power combiner and 16 × 16 Butler matrix network for acquiring GRE images. SNR maps were derived from the GRE image for the CP^+_1 mode (first-order clockwise CP) and other clockwise CP modes (CP^+_2–CP^+_8). In addition, the agreement between the FA maps and GRE image for all modes was compared. The mean SNR measurement of GRE axial image obtained by CP^+_1 mode and other clockwise CP modes was compared (Figure 3.9).

4.2.6.3 **Signal Intensity Profiles**

The GRE images obtained by several clockwise CP modes for the 16-element transmit array were compared by using one-dimensional SI profiles of the axial slices along the L-R direction. An SI profile was performed by using SNR maps acquired from the mixed sugar-water phantom.

4.3 Results

4.3.1 Simulation of Magnetic Field

4.3.1.1 Magnetic Field Creation Using Biot–Savart's Law

The eight-element transmit array (i.e., dimension of single element: vertical/horizontal length = 150 mm/80 mm) were simulated using Biot–Savart's law. In a dedicated ROI of 270 mm × 270 mm, the B_1 field distribution in free space without the loaded condition was created according to each element as shown in Figure 4.19.

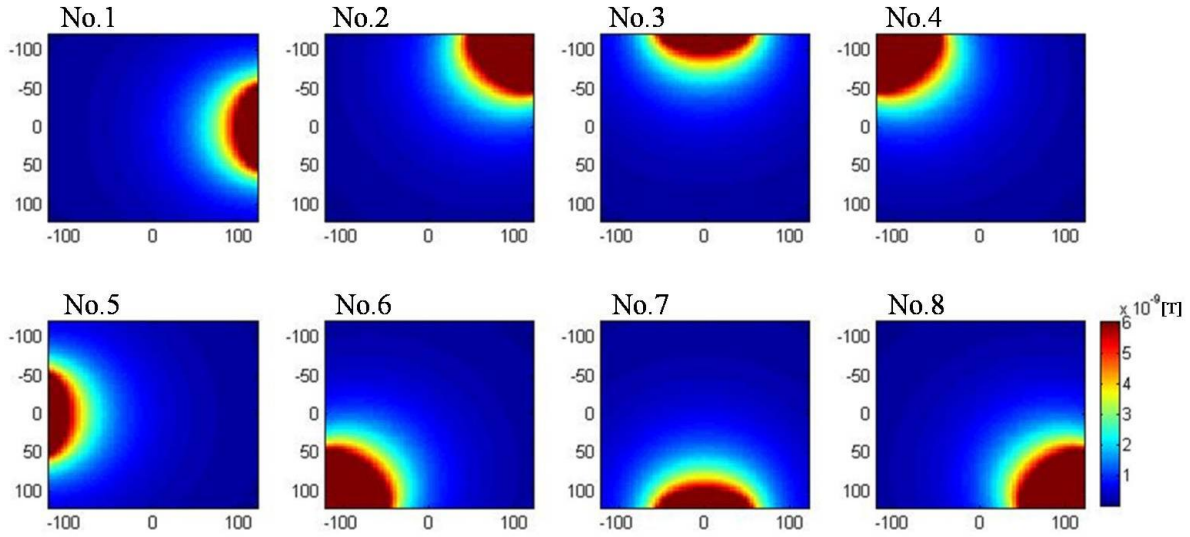

Figure 4.19: Individual B_1 field pattern of the eight-element transmit array

The ROI was determined by region for only the inside of the coil dimension as vertical and horizontal lengths of 270 mm. All color maps were obtained by all magnitude images, and the differences were illustrated on a color scale for comparison; the maximum B_1 SI is represented in red and the minimum in blue. For odd elements (i.e., Nos. 1, 3, 5, and 7 in Figure 4.19) and even elements (i.e., Nos. 2, 4, 6, and 8 in Figure 4.19), the B_1 field patterns were distributed identically to each other. The B_1 field pattern for each element was clearly rotated 45° from the center of the image. The B_1 field for each element was created by the *x*- and *y*-components of B_1 as shown in Figure 4.20. For instance, the No. 1 element showed that the B_1 field (Figure 4.20-a) was distinguished through each *x*- component (Figure 4.20-b) and *y*-component (Figure 4.20-c) of B_1.

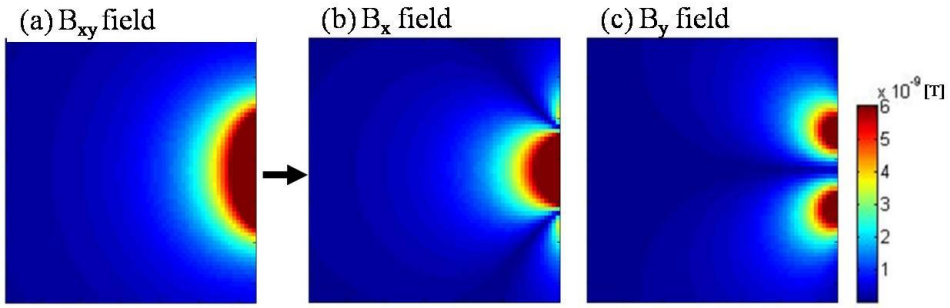

Figure 4.20: B_1 field pattern of a single element (No.1)

The individual B_1 field magnitude distributions for each element were combined (added) as shown in Figure 4.21-a.

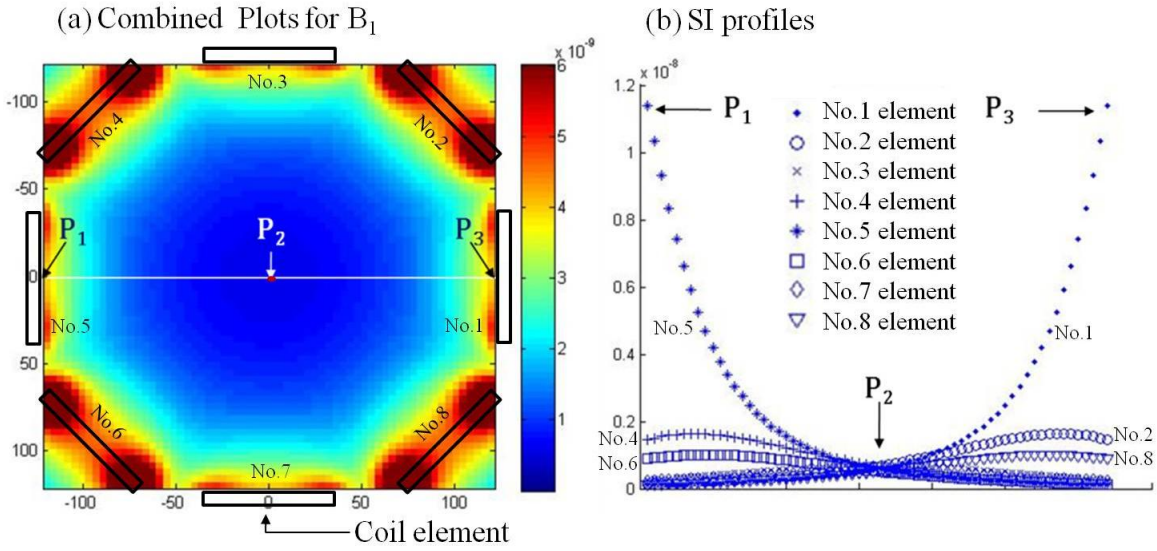

Figure 4.21: (a) Combined B_1 field distribution and (b) SI profiles of the eight-element transmit array

Combined B_1 field was distributed uniformly over the entire ROI from the peripheral region (P_1, P_3 in Figure 4.21-a) to the center region (P_2 in Figure 4.21-a). Figure 4.21-b shows the one-dimensional SI as a white line, which is the central line along the P_1-P_3 direction of Figure 4.21-a. For the No. 1 element, the B_1 SI decreased from the peripheral region (P_3 in Figure 4.21-b) to the center region (P_2 in Figure 4.21-b). The response of SI for each element was nonlinear with depth, resulting in an SI drop-off into the center region (indicated by P_2 in Figure 4.21-b) of the image. The high SI in peripheral regions such as P_1 and P_3 was attributed to being located around the conducting current of the eight-element array. B_1 field homogeneity using a variable horizontal length width of 10-100 mm and vertical length of 150 mm was created and compared for a single element, as shown in Figure 4.22.

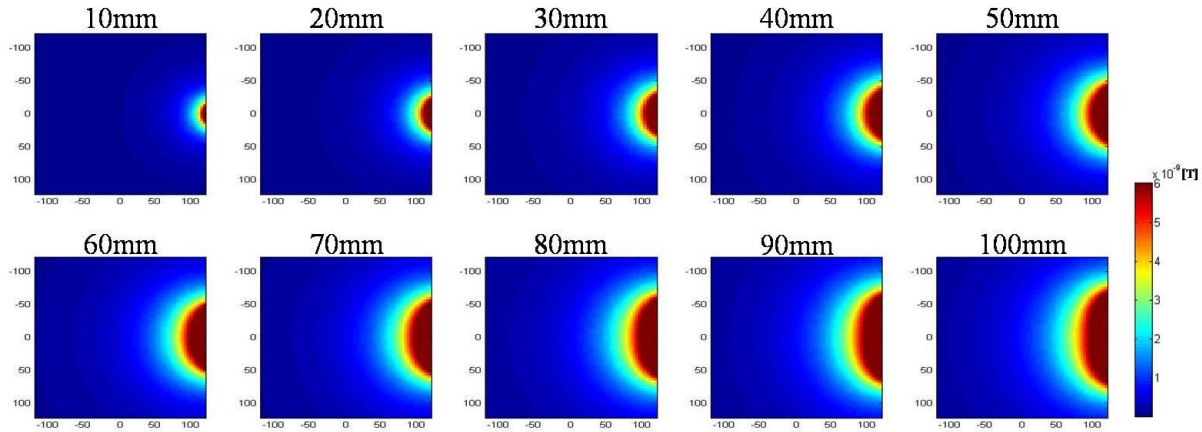

Figure 4.22: B_1 field distribution according to variable horizontal length of 10-100 mm for single element (No.1)

B_1 field pattern depended on the width of the single element. The *B_1* field for a width of 100 mm was widely distributed compared to other elements with a smaller width. For a more details, the SI profiles for each width were compared, as shown in Figure 4.23.

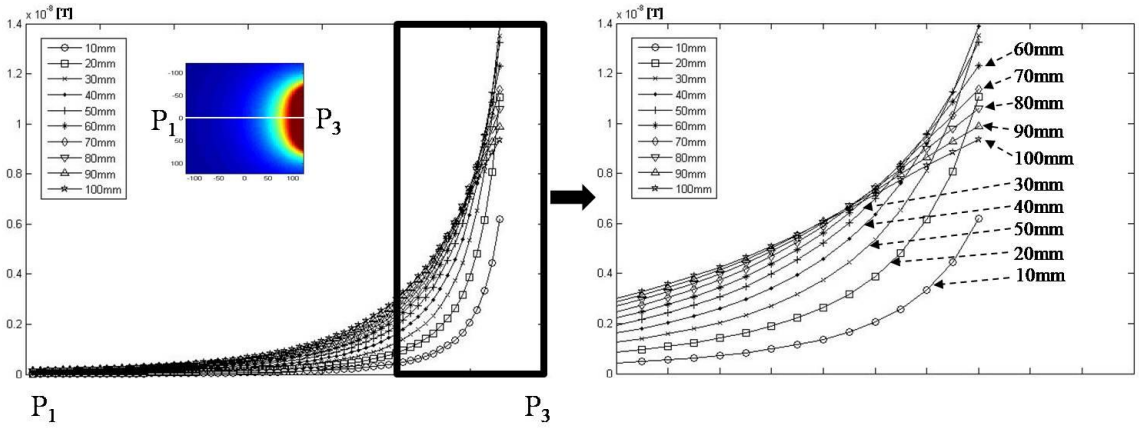

Figure 4.23: SI profiles according to variable width for a single element

SI was profiled from P_1 to P_3. SI was lower in the region of P_1 and very close to a zero value. In the right picture of Figure 4.23, the slopes for SI at widths of 70-100 mm width were closer to each other and higher than those at widths of 10–60 mm. The eight combined *B_1* field plots for a single element were compared for different widths of 10-100 mm, as shown in Figure 4.23.

Figure 4.24 shows that the *B_1* field homogeneity can be attributed to the width of the element for a dedicated coil diameter. The *B_1* field generated for widths of 80–100 mm was distributed uniformly. The *B_1* field pattern for widths of 70 mm and lower was inhomogeneous and showed the location of coil elements as an octagonal shape.

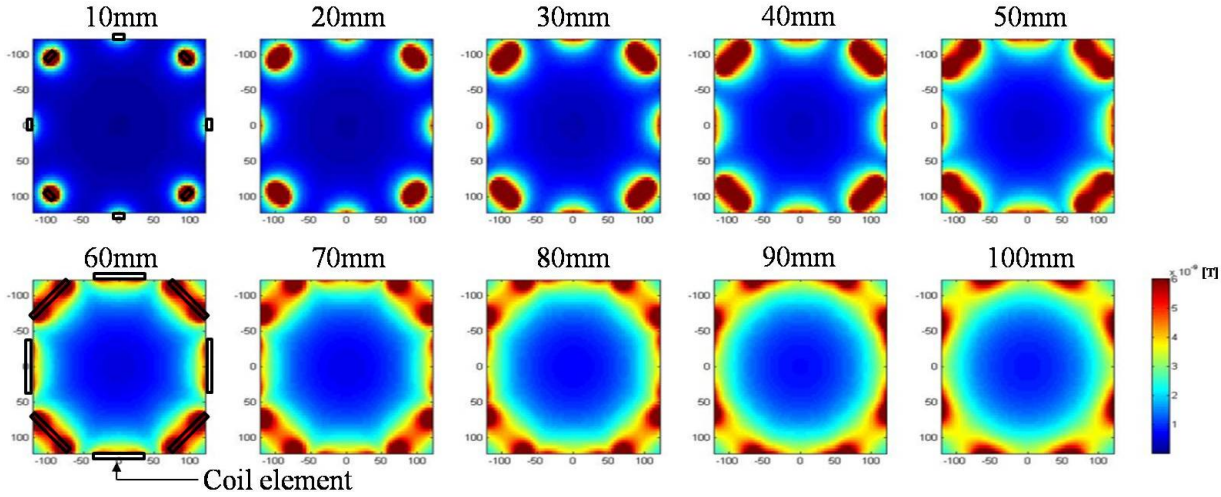

Figure 4.24: B_1 field distribution according to variable width of the element

The B_1 homogeneity and sensitivity were defined by the specific value using the maximum and mean signal divided by SD value of the B_1 field. Table 4.2 shows the maximum values and SD values of the B_1 field according to different horizontal widths of 10 - 100 mm and a vertical length of 150 mm.

Table 4.2: Maximum, mean signal, and standard deviation according to different horizontal widths of 10–100 mm and vertical length of 150 mm

Width [mm]	Maximum B_1 [$\times 10^{-8}$ T]	Mean B_1 [$\times 10^{-8}$ T]	SD [$\times 10^{-8}$]
10 mm	0.0819	0.0404	0.0363
20 mm	0.1524	0.0762	0.0668
30 mm	0.2050	0.1047	0.0884
40 mm	0.2396	0.1256	0.1013
50 mm	0.2597	0.1400	0.1076
60 mm	0.2697	0.1496	0.1096
70 mm	0.2739	0.1561	0.1096
80 mm	0.2762	0.1609	0.1095
90 mm	0.2766	0.1643	0.1091
100 mm	0.2874	0.1705	0.1145

Figure 4.25-a show the plot for dividing the value of the maximum value divided by SD value of the B_1 field created by a variable horizontal width. These results indicate that the value of the eight-element array using the horizontal length of 90 mm was better than when the array used horizontal lengths of 100 and 70 mm by 10% and 14%, respectively. However, for a horizontal length of 80 mm, the value decreased by 0.5% compared with the horizontal length

of 90 mm. Figure 4.25-b also shows mean value divided by SD value of the B_1 field created by variable horizontal lengths.

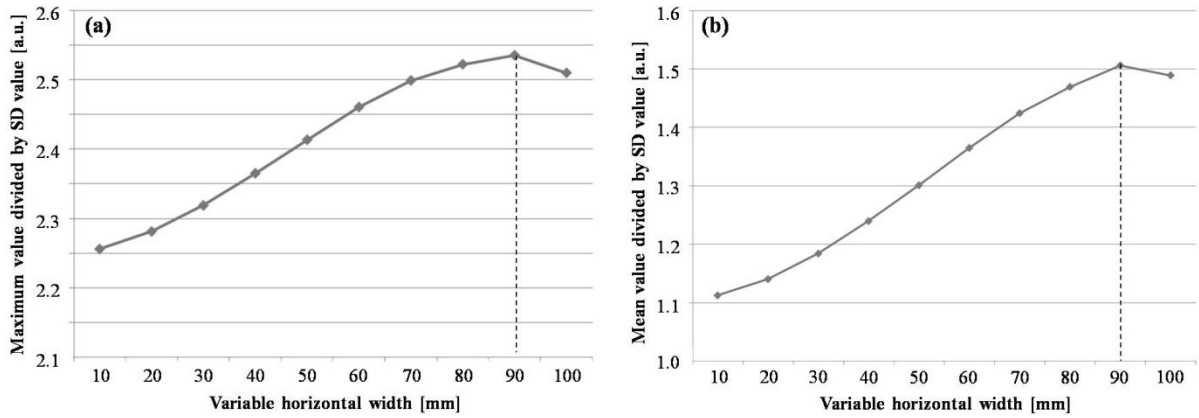

Figure 4.25: (a) maximum value and (b) mean value divided by SD value of the B_1 field created by variable horizontal width

The specific dividing the value when using a horizontal width of 90 mm was much better than that for the other horizontal widths. In an eight-element transmit coil array, the horizontal width of 90 mm and vertical length of 150 mm achieved a higher B_1 sensitivity and homogeneity as compared to the other variable horizontal widths.

4.3.1.2 **EM Simulation using CST MWS**

The eight-element and 16-element transmit coil arrays were simulated to compare B_1 field distributions for CP_1^+ excitation, especially that of the B_1^+. Two transmit coil arrays were found to have more than -25 dB for the return loss and isolation between adjacent coils. Each element of the investigated resonators was numerically tuned to the proton frequency at 7T (297.2 MHz) and matched to 50 Ohm. Figure 4.26 shows the recalculated central axial maps of the B_1^+ in eight-element (Figure 4.26-a) and 16-element transmit coil arrays (Figure 4.26-b) for spherical oil (Figure 4.26-i), a water phantom (Figure 4.26-ii), and a Hugo brain (Figure 4.26-iii). The maximum B_1^+ was normalized to the arbitrary value of 1.5 and compared through different color scales from red (maximum SI) to blue (minimum SI). The currents excitation in the coils was kept equal for 8- and 16-elements, leading to approximately double the power delivered by the 16-element array.

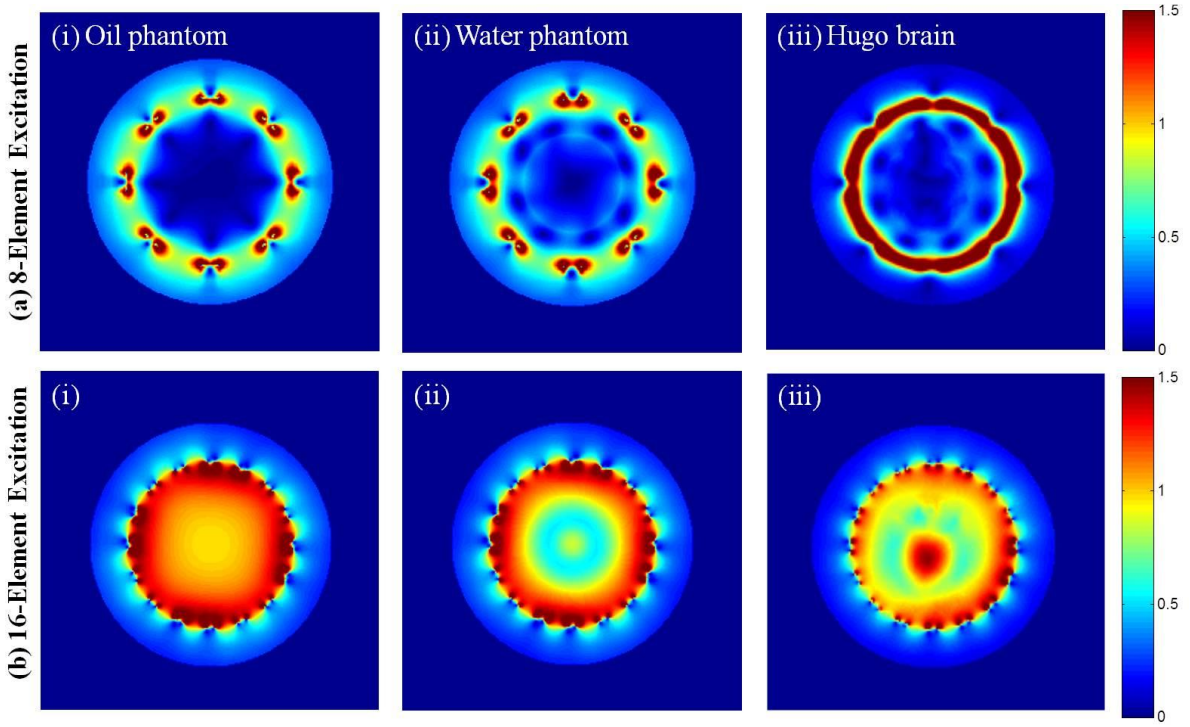

Figure 4.26: Recalculated central axial B_1^+ maps of (a) eight-element and (b) 16-element transmit arrays

The average strength of the B_1^+ for the 16-element array (Figure 4.26-b) was much better than that for the eight-element array (Figure 4.26-a). The results indicate that the relative mean value (eight-element/16-element: 0.49/0.71) was increased by 45% in the water phantom and (8-element/16-element: 0.50/ 0.78) by 56% in the oil phantom for the 16-element array as compared to the standard eight-element coil array. However, the relative SD value in the water phantom (eight-element/16-element: 0.40/ 0.43) for the 16-element coil array was 3% lower than that for the eight-transmit array. Although the SD value of each array was measured to a difference of ±3% in the region of interest (ROI) (i.e., the real imaging area existing inside the RF coil), the 16-element coil array was more symmetrically distributed from the peripheral region to the center region. In particular, the water phantom image of the eight-element coil array had a more asymmetric B_1^+ distribution as compared to the 16-element coil array. In the Hugo brain model (Figure 4.26-iii), the relative mean value (eight-element/16-element: 0.60/ 0.66) was increased by 10% for the 16-element coil, and the SD value (eight-element/16-element: 0.90/ 0.39) had a lower value as compared to the eight-element transmit array. The 16-element array led to a more homogeneous B_1^+ that is much higher than that of the eight-element transmit array, especially at the center of the phantom.

4.3.1.3 SAR Calculation Using CST MWS

To predict the RF power absorption behavior of the eight-element and 16-element arrays, SAR values were simulated together with J. Mallow in a two-dimensional plane inside the Hugo brain model, as shown in Figure 4.27.

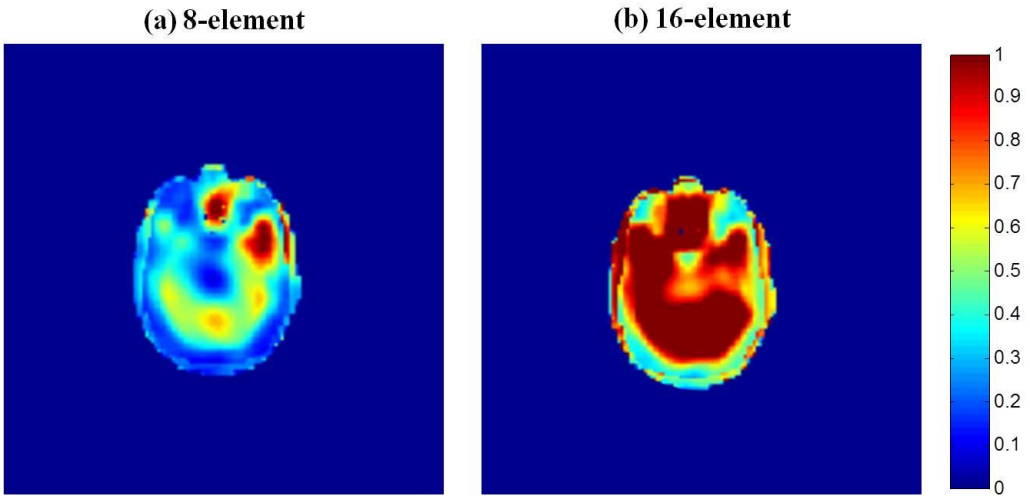

Figure 4.27: SAR distributions using transmit head-array coils

The corresponding color bars represent the normalized SAR values for every 10 g of tissue. Figure 4.27 shows the normalized SAR distribution for an axial slice of the head at 7T assuming a 1 W CW input. The SAR limitations [122] under the average over 10 g of tissue were considered to evaluate new coil designs and excitation techniques. The proposed 16-element coil array demonstrated a significant higher peak SAR distribution in the brain compared to the eight-element excitation coil (16-element/eight-element = 3.6813/1.7659 [W/kg]).These result indicate that the peak SAR for the 16-element excitation coil over the human brain region was twofold increased.

4.3.2 Electrical Characteristics

4.3.2.1 Multiple Transmit Coil Arrays

All coils were manufactured on a 270 mm diameter cylindrical acryl case and matched to 50 Ohm while loaded with a phantom. Two transmit coil arrays made up of rectangular elements were placed on a cylinder and designed to be non-overlapping (Figure 4.28) using the same

dimensions as those shown in Figure 4.10.

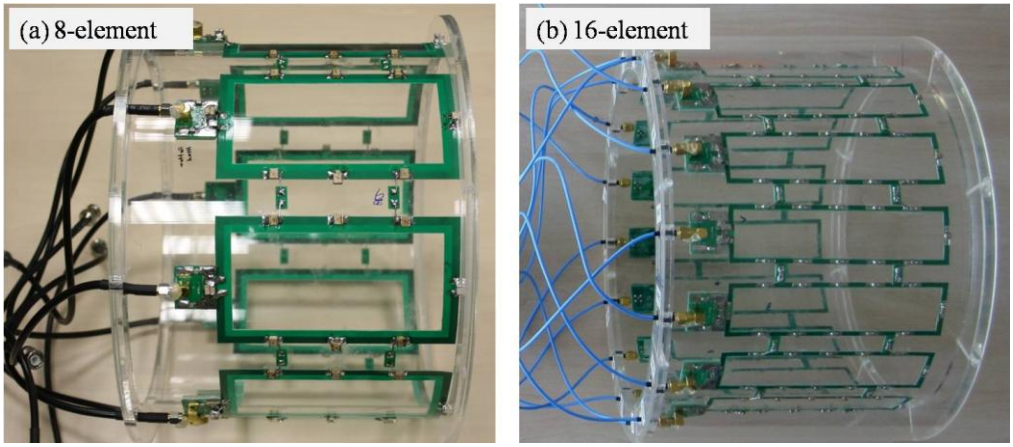

Figure 4.28: Geometry of transmit head array coils

Tuning and matching for all elements were optimized at 297.2 MHz. In particular, mutual coupling between neighboring elements for two transmit arrays ranged between -18 and -24 dB. The return loss was also measured to be better than -25 dB for each element.

4.3.2.2 **RF Circuitry for Transmit Coil Arrays**

The Wilkinson power splitter using lumped elements (Figure 4.29) was developed based on a simulation of the electrical circuit (Figure 4.12). The according designed element was measured (Table 4.3) using a vector network analyzer (N.A.).

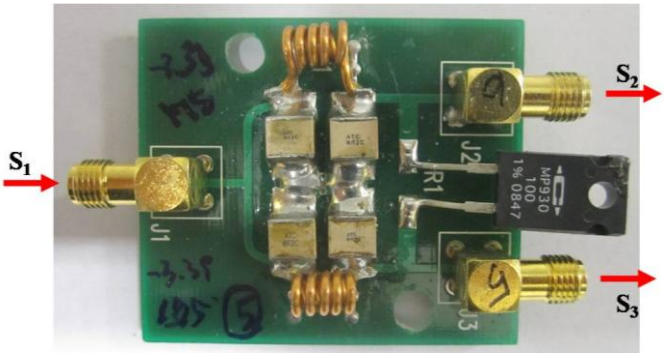

Figure 4.29: Image of the Wilkinson power splitter

The observed transmission loss ($S_{21,}$ S_{31}) was approximately -3.35 dB. The phase difference (S_{21} and S_{31}) of two outputs for the transmission loss (S_{21}) was within 1°. For RF transmission,

power was split from port S_1 equally, and no phase difference was distributed between the 2nd and 3rd ports. The isolation and directivity was very high at a center frequency of 297.2 MHz.

Table 4.3: S-parameters for transmission of Wilkinson power splitter (in Figure 4.29)

Power Splitter	S-parameter	Transmission Loss [dB]	Transmission Phase [°]	Difference Loss [dB] (S_{21} and S_{31})	Difference Phase [°] (S_{21} and S_{31})
No.1	S_{21}	-3.36	176.3	0.02	0.1
	S_{31}	-3.38	176.5		
No.2	S_{21}	-3.38	175.4	0.06	0.3
	S_{31}	-3.32	175.1		
No.3	S_{21}	3.38	174.2	0.03	1.0
	S_{31}	3.35	175.2		
No.4	S_{21}	3.35	175.5	0.00	0.9
	S_{31}	3.35	174.6		
No.5	S_{21}	3.42	176.6	0.07	0.5
	S_{31}	3.35	176.1		
No.6	S_{21}	3.36	175.3	0.02	0.2
	S_{31}	3.38	175.1		
No.7	S_{21}	3.34	174.2	0.02	0.9
	S_{31}	3.36	175.1		
No.8	S_{21}	3.37	175.2	0.09	0.3
	S_{31}	3.46	174.9		

The Tx/Rx switches were designed as shown in Figure 4.30.

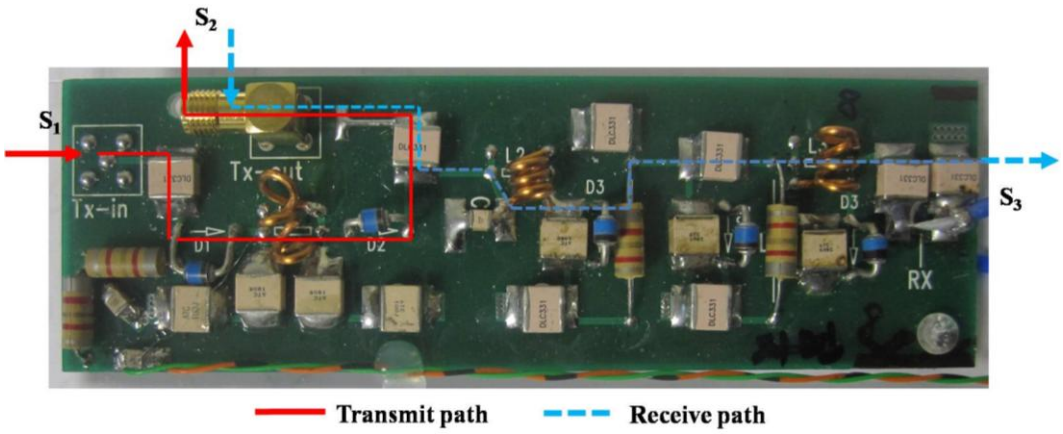

Figure 4.30: Image of the lumped element Tx/Rx switches

For Tx timing, each amplified RF signal in the pTx system is delivered to the S_1 port (input of

transmit power). Tx power then goes to the S_2 port, which is connected to one element of the transmit-head head-array. For Rx timing, the RF signal comes from the head-array. This signal goes from S_2 (output of transmit power) to S_3 (output of RF signal and connected to preamplifiers). The characteristics of the Tx/Rx switches were measured (Table 4.3).

Table 4.3: S-parameters of Tx/Rx switches (in Figure 4.30)

Power Splitter	S-Parameter			
	Reflection Coefficient [dB]	Reflection Coefficient [dB]	Transmission Phase [°]	Transmission Loss [dB]
	S_{11}	S_{22}	S_{21}	S_{32}
No.1	-19.3	-14.9	29.4	-0.70
No.2	-18.9	-19.6	31.0	-0.69
No.3	-21.3	-19.4	30.0	-0.60
No.4	-22.3	-23.5	31.0	-0.64
No.5	-24.3	-22.3	31.1	-0.66
No.6	-18.0	-21.0	30.7	-0.71
No.7	-22.5	-20.5	30.0	-0.63
No.8	-21.9	-22.8	30.2	-0.71
No.9	-22.5	-22.1	31.9	-0.60
No.10	-25.5	-26.0	30.9	-0.68
No.11	-28.0	-19.7	31.2	-0.68
No.12	-23.6	-21.8	30.0	-0.60
No.13	-28.0	-18.4	30.4	-0.61
No.14	-19.1	-23.0	31.0	-0.71
No.15	-22.6	-27.0	30.5	-0.63
No.16	-23.1	-21.1	29.7	-0.72

Phase shifters of 45° and 22.5° for the eight-element and 16-element transmit array, respectively, were used with different lengths of RG 316 coaxial cable. The phase differences according to different lengths of the cable were measured with N.A at the center frequency of 297.2 MHz, as shown in Figure 4.31. This ranged from 247.2 MHz to 347.2 MHz and was measured accurately as 45° for the eight-element array (Figure 4.31-a) and 22.5° for the 16-element array (Figure 4.31-b). Phase differences are recorded in Table 4.5.

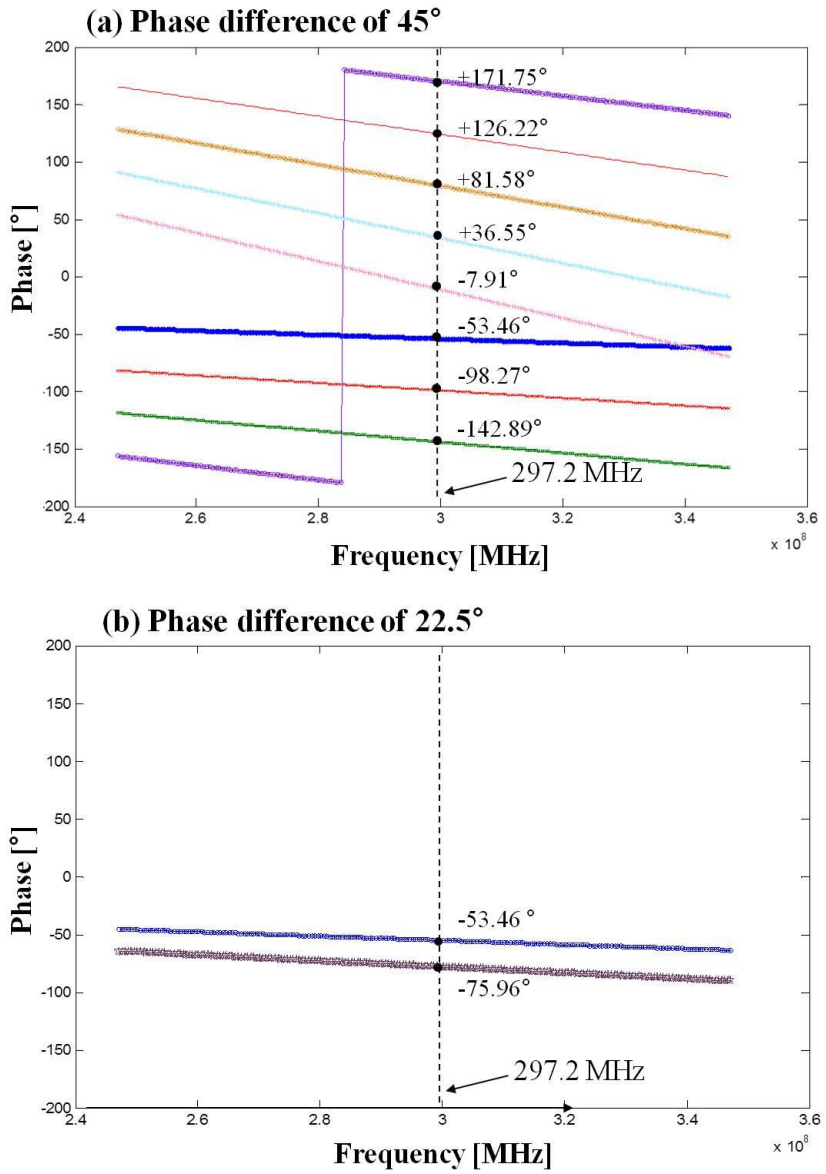

Figure 4.31: Phase difference according to different lengths of the cable

Table 4.4: Phase differences according to different lengths of RG 316 cable

Phase Difference for 45° (at 297.2 MHz)								
Reference	0°	-45°	-90°	-135°	-180°	-225°	-270°	-315°
Measurement	-53.46°	-98.27°	-142.89°	+171.75°	+126.22°	+81.58°	+36.55°	-7.91°

Phase Difference for 22.5° (at 297.2 MHz)		
Reference	0°	-22.5°
Measurement	-53.46°	-75.96°

4.3.3 Assembled RF Coil and Circuitry

All measurements were performed on a whole-body 7T scanner with an eight-channel transmit array feeding eight 1 kW peak RF power amplifiers (Siemens Medical Solutions, Erlangen, Germany). For the eight-element transmit coil array, each output of the RF amplifier was connected to the input of the phase shifter. Each RF signal with a difference in phase of 45° went to the input of the Tx/Rx switches, as shown in Figure 4.32-a.

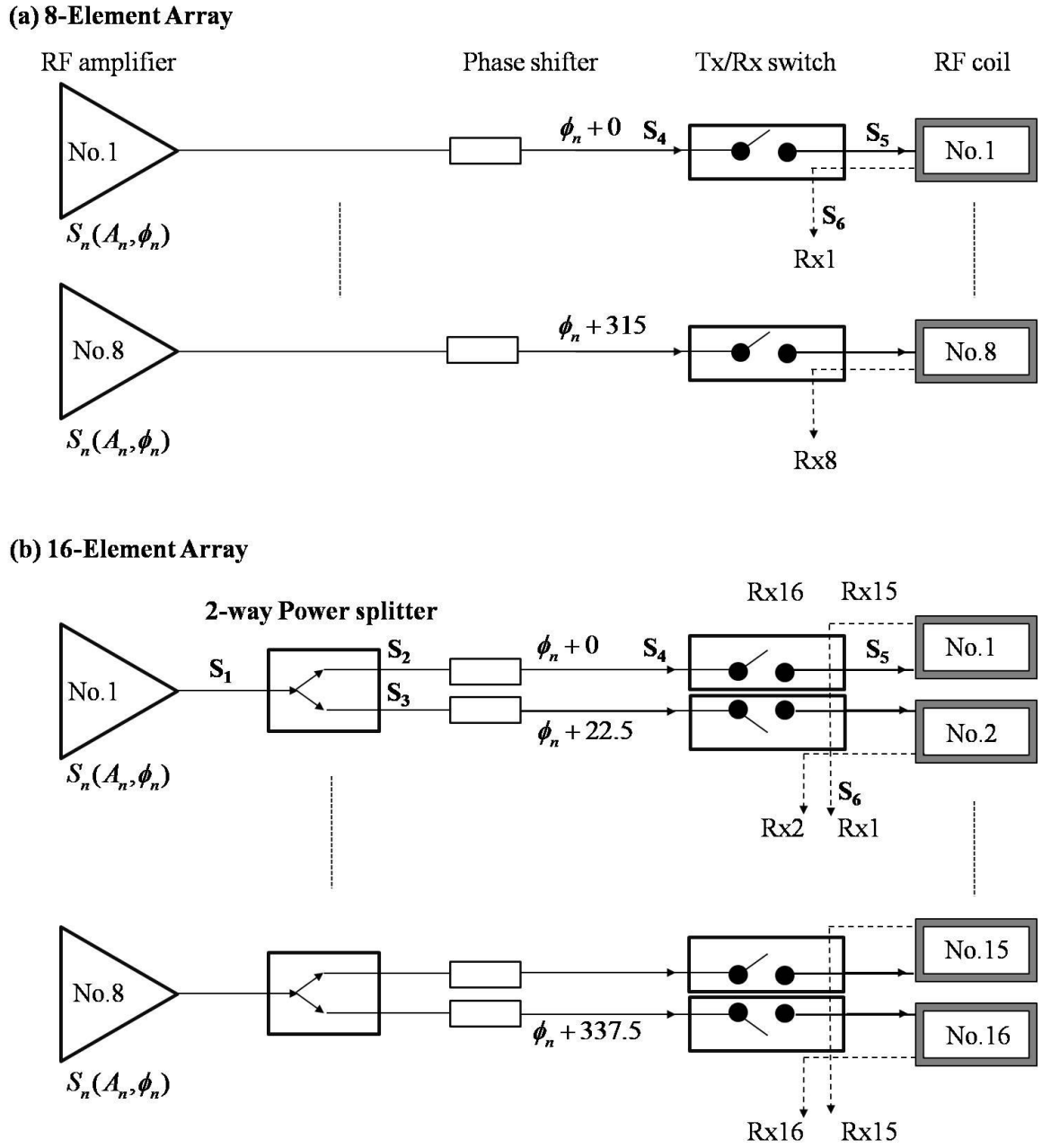

Figure 4.32: Schematics of RF excitation with dedicated eight-driven pTx system for (a) eight-element and (b) 16-element transmit head-arrays

$S_n(A_n, \phi_n)$ is the RF signal (amplitude, phase) number of the n^{th} element. ϕ_n is the phase of the n^{th} element. For 16 RF excitations of the 16-element array, eight Wilkinson power dividers were used, and the phase shifted out of phase by 22.5° through an extra cable length, as shown in Figure 4.32-b. Tx/Rx switches, preamplifiers, a phase shifter, and two-way power dividers were assembled for the 16-element transmit array, as shown in Figure 4.33, using the abovementioned schematics (Figure 4.32-b).

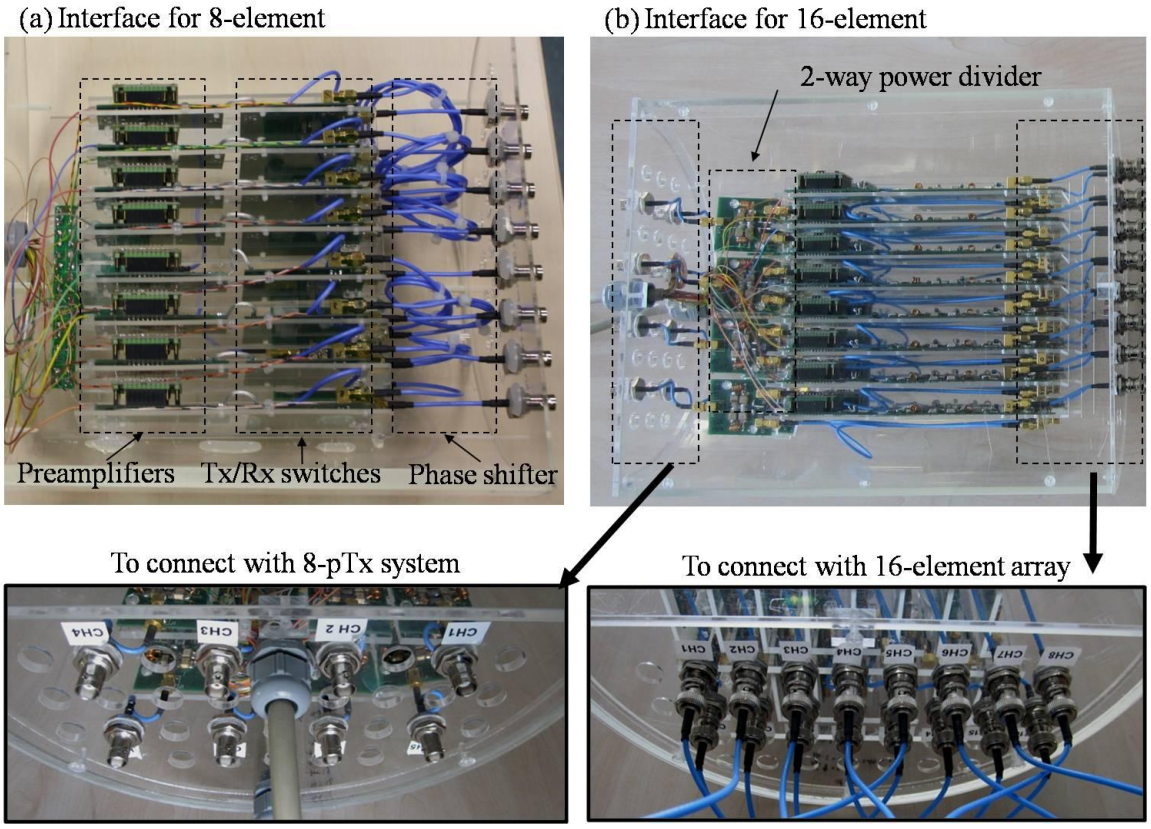

Figure 4.33: RF circuitry for (a) eight-element and (b) 16-element transmit head-arrays and enlarged parts of (b) are shown in the lower row

4.3.4 Maps of Effective Flip Angle

The difference in FA for the RF array was evaluated as the effective FA for the given FA (α_{giv} = 90°). The FA maps of 16 individual elements (E.1 – E.16) on the central axial slice of the oil phantom are shown in Figure 4.34.

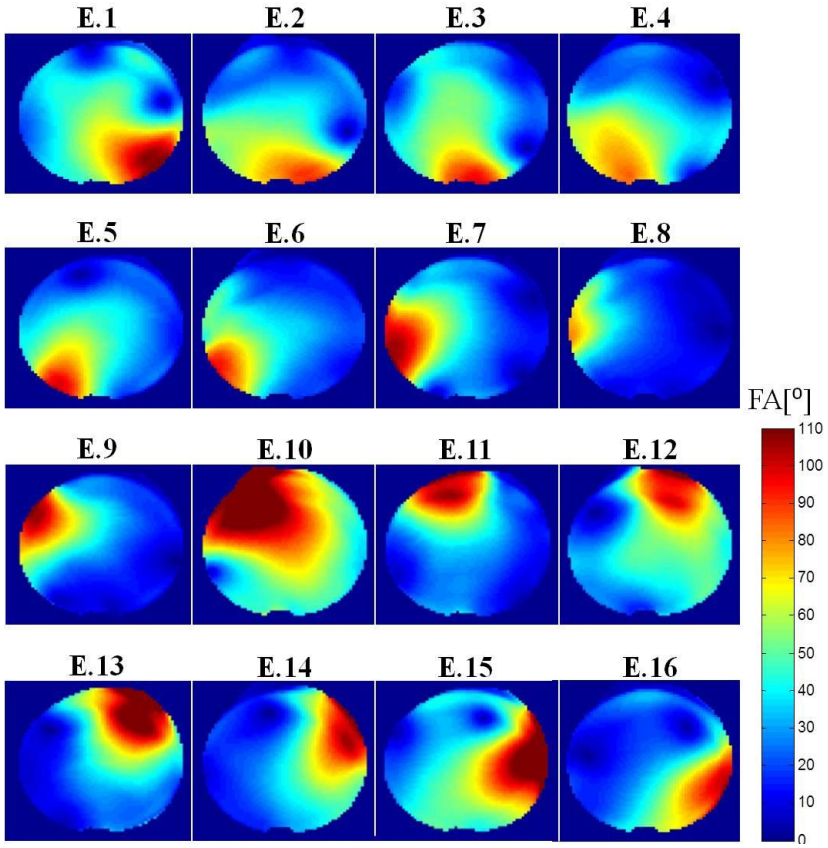

Figure 4.34: Sixteen individual FA maps for an oil phantom

Sixteen normalized FA maps were acquired for odd-even elements of a 16-element head-array using a dedicated eight-channel driven pTx system. In Figure 4.34, we see reduced FA (i.e. E.4 and E.8) and increased FA (i.e. E.10) in elements which both can be explained by the fact that the array elements had been tuned and matched to a non-symmetric load (human head). Eight individual FA maps from the combined excitation of two elements were measured, as shown in Figure 4.35.

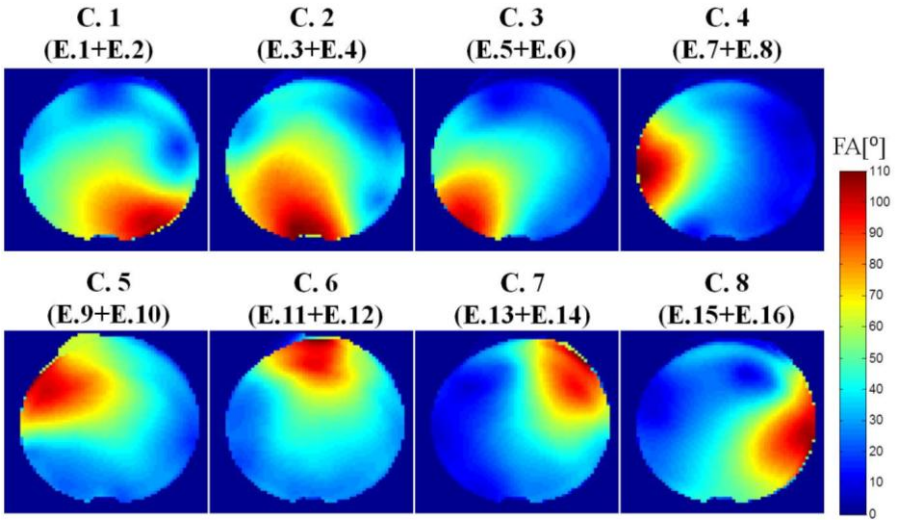

Figure 4.35: Eight individual FA maps of oil phantom from the combined excitation of two elements using a 16-element transmit array

A quantitative comparison for the combined FA maps of the 16 and 8 individual FA maps from the combined excitation of two elements using a 16-element transmit array were acquired as shown in Figure 4.36.

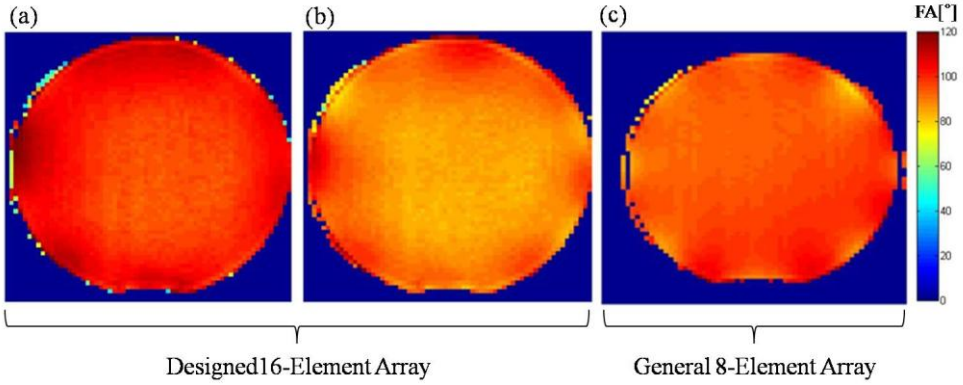

Figure 4.36: Combined FA maps of (a) 16-element transmit array, (b) eight-combined element transmit array, and (c) eight-element transmit array in the oil phantom

Both measurements were acquired with identical FA and on the same oil phantom. In Figure 4.36, all of the FA maps showed good B_1^+ fields. The distribution of FA maps in the 16-element transmit array (a) was more homogeneous than for the other two transmit coil arrays. The SD of the 16-element transmit coil array was 3.2 of the effective FA for the chosen FA ($\alpha = 90°$). On the other hand, the eight-element transmit array has a factor of 4.3, and the eight-element combined transmit array has 5.4. Therefore, the FA difference for the 16-element excitation channels decreased by 59% compared to the eight excitation channels of the general structure of eight-channel Tx/Rx transmit arrays. The FA maps of 16 individual

elements on the central axial slice of the water phantom are shown in Figure 4.37.

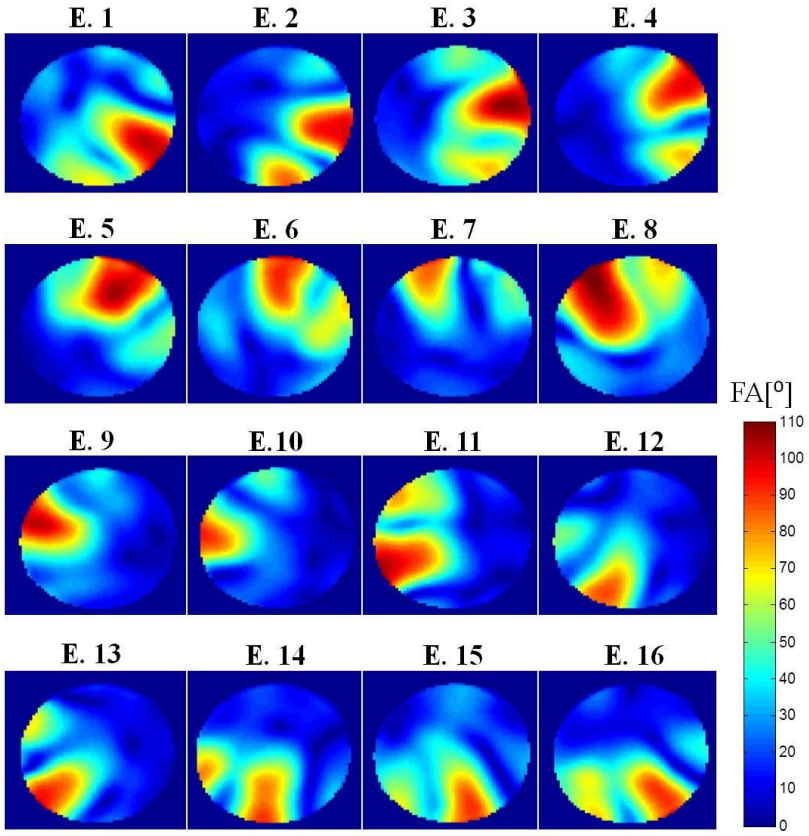

Figure 4.37: Sixteen individual FA maps of the water phantom

For comparison of the B_1^+ field, FA maps were compared with the water phantom, as shown in Figure 4.38. The FA distribution of the 16-element transmit array (Figure 4.38-a) had a more homogeneous transmit field than the standard eight-channel transmit array (Figure 4.38-b). The SD difference between given and effective FA for the 16-element transmit array was 43% and 26% higher than that of the eight-element combined transmit array and general structure of eight-element transmit array (16 channels/ eight-combined element/ eight element = 10.19/ 14.66/ 12.92).

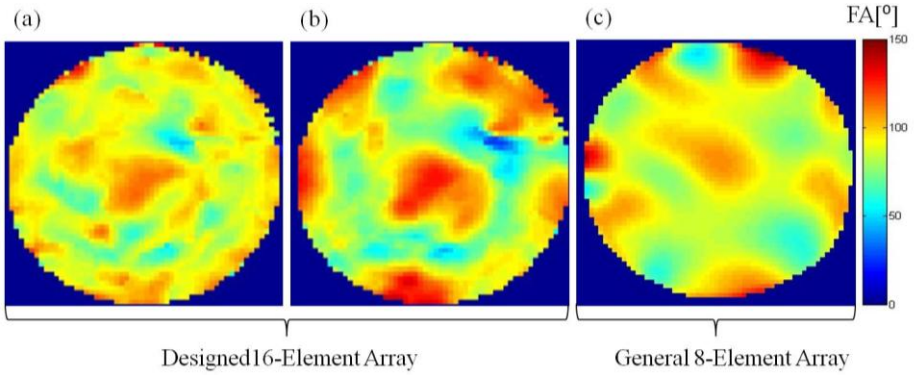

Figure 4.38: Combined FA maps of (a) 16-element transmit array, (b) eight-combined element transmit array, and (c) eight-element transmit array in the water phantom

4.3.5 SNR Maps

GRE images according to difference modes such as the CP mode (CP_1^+) and other clockwise CP modes (CP_2^+-CP_8^+) of the 16-element array were acquired by using a spherical mixed sugar-water phantom, as shown in Figure 4.39.

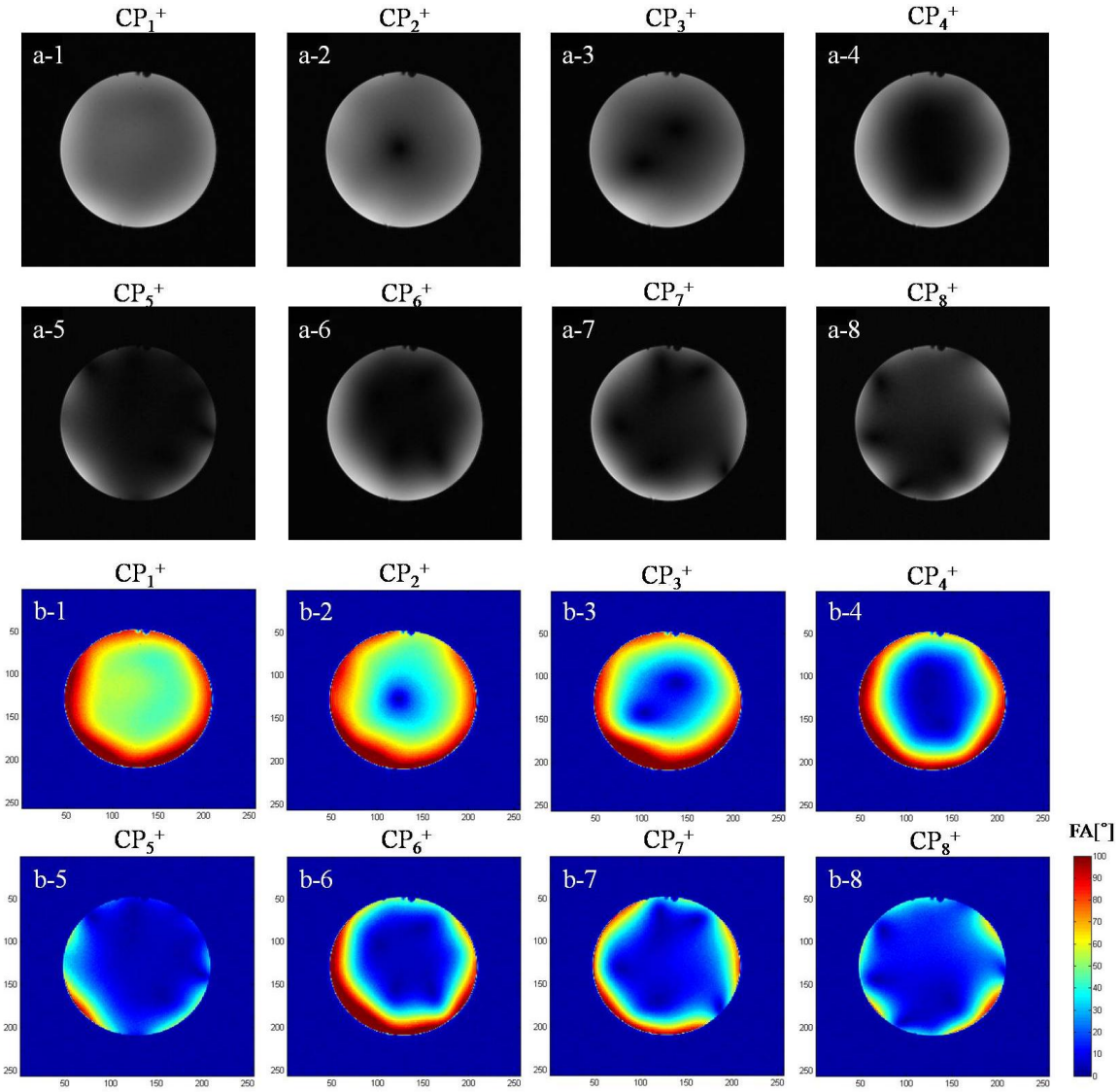

Figure 4.39: (a) GRE image and (b) FA maps for clockwise CP modes

Figure 4.39 shows GRE images according to different modes (upper row of Figure 4.39, indicating from a-1 to a-8). Good agreement was achieved between FA maps (for α_{giv} of 90°) and the GRE image for all modes. The GRE image and FA maps of Figure 4.39-a-1 show a more homogeneous distribution compared to the other modes. The FA differentiation was measured for α_{giv} of 90°, as shown in Figure 4.40.

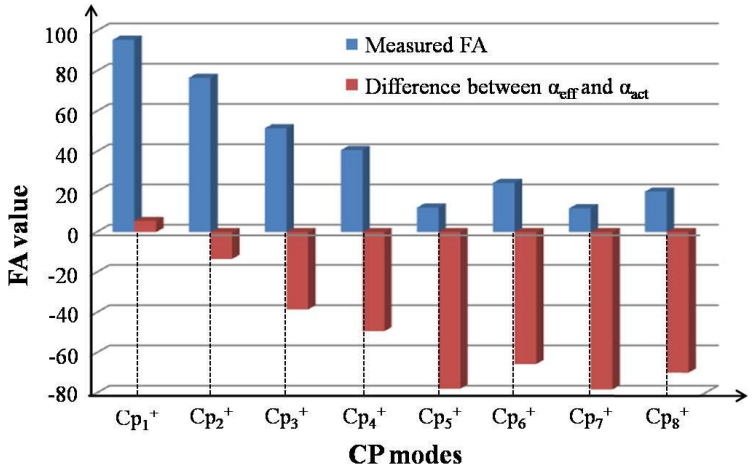

Figure 4.40: FA measurement for clockwise CP modes

The differentiation was smallest for CP_1^+ mode and largest for CP_5^+. In particular, only CP_1^+ had a positive differentiation (i.e., over flip) for the entire image.

4.3.6 Signal Intensity Profiles

To compare the B_1^+ field homogeneity on the central axial GRE slice along the L-R direction, SI profiles for several modes (upper row of Figure 4.39) are shown in Figure 4.41. The SI of CP_1^+ mode had a higher homogeneity compared to the other modes despite some variance across the center of the image with lower SI. In particular, SI of the CP^+_2 mode represented the deepest drop away from the peripheral region to the central region compared to other modes.

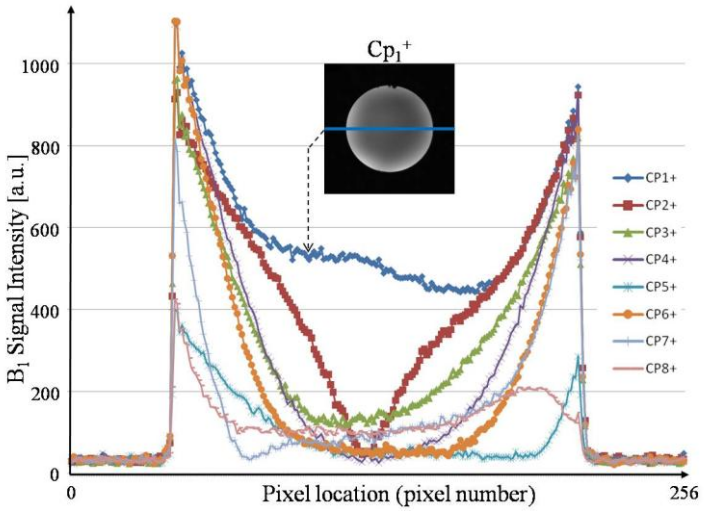

Figure 4.41: Signal Intensity Profiles for clockwise CP modes

4.3.7 Mean SNR Measurement and Specific Ratio

The mean SNR for various clockwise CP modes was measured from the GRE image (Figure 4.39) and is presented in Table 4.6.

Table 4.6: Mean SNR measurement for a mixed sugar-water phantom

Mode	CP_1^+	CP_2^+	CP_3^+	CP_4^+	CP_5^+	CP_6^+	CP_7^+	CP_8^+
SNR	131.7	124.2	112.4	94.6	31.2	78.7	60.1	43.1

The highest mean SNR value for the entire ROI was 131.7 in CP_1^+ mode; the mean SNR was 31.2 for CP_5^+ mode, which is 4.2 times lower than that for CP_1^+. To evaluate the homogeneity and sensitivity of the B_1 field, the mean signal, SD, and their ratio (mean signal/SD) in the ROI were acquired from the GRE image and are presented in Table 4.7.

Table 4.7: Signal measurement for a mixed sugar-water phantom

Mode	CP_1^+	CP_2^+	CP_3^+	CP_4^+	CP_5^+	CP_6^+	CP_7^+	CP_8^+
Mean	646.7	578.4	513.0	426.8	147.3	368.4	273.4	199.6
SD	193.4	229.2	286.8	310.2	147.6	332.7	229.8	142.5
Mean/SD	3.34	2.51	1.78	1.37	0.99	1.10	1.18	1.39

Table 4.7 shows that the mean signal values of the axial B_1 field for CP_1^+ was measured to be larger by a minimum of 11% using CP_2^+ mode to a maximum of 78% using CP_5^+ mode. However, the SD values for the GRE image of CP_1+ were measured from a minimum of 27% using CP_8^+ mode to a maximum of 72% using CP_6^+ mode. The specific ratio between the mean value and SD value were compared to evaluate the performance of the RF coil with regard to B_1 sensitivity and homogeneity. The results indicate that the ratio had a minimum of 25% using CP_2^+ mode to a maximum of 71% using CP_5^+ mode when compared to the ratio acquired with CP_1^+ mode.

5 CONCLUSIONS AND FUTURE WORK

5.1 Conclusion and Discussion

5.1.1 7T Single-channel Tx/Rx Coils

In this study, well characterized CP volume coils were evaluated and compared in terms of SNR and B_1 field homogeneity, including B_1^+ homogeneity by using SNR maps, mean SNR measurement, one-dimensional SI profiles, and pixel counting according to SI, FA maps to assist in CP volume coil selection at 7T using a single RF transmission system.

The variations in the B_1 field distribution in the center and peripheral regions still remained (Figure 3.15 and Figure 3.16). Although the B_1 field for all CP coils was distributed irregularly, and the B_1 field produced restricted B_1 homogeneity, SI of the ST coil was more symmetrically and widely distributed from the center region on an axial slice of the human brain (Figure 3.16-d). In addition, ST coil had a relatively higher SI profile (Figure 3.17-ii) in superior part of human brain for all pixel locations, due to the higher B_1 field strength over the entire image. The FA maps (Figure 3.19) and difference (Table 3.4) in acquired FA value for a given FA was compared for all CP volume coils. Explicitly, for an average FA covering the entire image, the difference from a given FA was lower for the ST coil compared to the other coils.

For all CP coils, the central region had high SI compared to the peripheral region, which is due to constructive and destructive interference from the RF wave [85, 127]. The homogeneity of the B_1 field and source currents in the RF coil are strongly perturbed by sample loading [128]. Therefore, all CP volume coils in the UHF intrinsically generate an inhomogeneous B_1 field attributed to the dielectric effect rather than the RF coil geometry.

The simulation-based comparison for the performance of the RF coil at 7T for the same dimensions was performed. In a study of Wang CS et al [86], the microstrip coil had the best performance in terms of SAR and SNR followed by birdcage coil and TEM coils. The ISMRM proceeding [129] of DeMeester et al. shows an EM simulation based comparison study for TEM Tx/Rx head coil and shielded birdcage coil at 7T under the same physical size. In this proceeding, the B_1 field uniformity of the birdcage coil was comparable or better than the similarly sized TEM head coil. Four 7T CP volume coils and one eight-channel array coil were constructed and compared by Wald et al. [18]. Their results indicated that birdcage coil

has similar SNR profiles through an axial GRE image with a high-pass birdcage and small TEM coil. However, they used different coil diameters and lengths for each coil. In UHF MRI, a map of the B_1^+ field strength (i.e., a B_1^+ map) should be considered in particular. Several MRI-based B_1 mapping methods have been proposed: acquisition of an SE and STE sequence allowing for FA calculation from the signal quotient [130], a double-angle method using different nominal FA images [92], actual flip angle imaging (AFI) based on fast low angle shot (FLASH) imaging [131], and so on. The method proposed in this work is based on acquisition using SE, and an STE was chosen to quantify a certain RF excitation angle. The experimental results validated the FA accuracy for the nominal angle chosen on the MRI scanner. This finding was supported by the corresponding FA maps and difference in acquired FA value for a given FA.

The scope of this thesis was to provide only the experimental data for coils having the same dimensions to compare performances. The RF coil and circuitry design presented here were limited to 297.2 MHz in association with a 7T MRI system. For comparisons to previous Tx/Rx volume designs, the coil geometry was mostly used and adapted to an HF environment (1.5 or 3 T). In this study, coil geometry of 16 legs (each 10 mm wide) was chosen for both the HBC and HSBC coils. The DH coil had eight legs (each 10 mm wide). For the ST coil, the chosen geometry had four legs (each 104 mm wide). These extensions were required as an aid for coil selection at 7T for loading, *in vivo* the human head. It remains to determine the various copper shielding on the outside of the coil structure [132] for the proposed CP coil to acquire the maximum B_1 amplitude and best homogenous B_1 field. Therefore, in future work, the efficiency of CP volume coils in a 7T MRI needs to be quantitatively evaluated after manufacture of the CP coil.

To summarize, four well characterized CP volume coils were compared experimentally concerning their SNR and B_1 field homogeneity, including B_1^+ homogeneity, at 7T. For the experimental B_1 distributions of the well characterized CP coils, SI and the B_1 field shapes still varied because of the interaction between the subject and different coil structures. Although the B_1 field for all CP coils was distributed irregularly and produced limited B_1 homogeneity, the B_1 SI of the ST coil was more symmetrically and widely distributed from the central region in an axial slice of the human brain.

5.1.2 7T Multi-channel Transmit Arrays

This study represents the first experimental investigation for combined eight-element and individual 16 FA maps of 16-element transmit array surface coils compared to the eight-element array. Unique criteria were identified, and the coil was designed for human brain imaging applications. Moreover, the study compared several evaluation factors as SNR maps, mean SNR measurements, FA measurements, and signal homogeneity. In this study, eight-element and 16-element transmit coil arrays and RF circuits were designed, simulated, evaluated, and experimentally compared in terms of B_1 field distribution, SNR maps, and FA maps, in particular. The designed 16-channel transmit array and RF-interface showed different FA maps in comparison to the eight-element combined excitation and eight-element Tx/Rx head-array. The B_1^+ homogeneity generated by the 16-element transmit array was more uniform compared to the eight-channel combined excitation and eight-element Tx/Rx coil head-array (Figure 4.36 and Figure 4.38). Higher B_1^+ homogeneity was achieved by using more transmit channels. The experimental results showed that increasing the number of transmit channels improved the B_1 field [48]. However, increasing the number of transmit channels by using 16 elements instead of eight elements did not significantly improve B_1 homogeneity any further.

This study assumed a perfect RF coil and perfect coil circuitry for the Tx/Rx switches, power splitter, and phase shifter. Non-optimized RF coils and circuitry can also generate different MR images, resulting in signal losses and an inhomogeneous B_1 field. The performance of the RF device for this study relied on only the S-parameter as a bench test. Finally, the performance of the RF receive chain of the MRI system was ignored because the resultant signal loss from the RF coil and circuitry affecting the MR image is the same; thus, all designs and MR imaging were affected equally.

For transmit coil arrays in UHF MRI system, EM simulation and other coil geometry using helmets [133] or concentrically shielded transceiver arrays [134] were shown and compared in other literature. Although the circumferential coil geometry on cylindrically shaped cases was compared and evaluated by simply using more elements in this study, further exploitation of these phenomena will hopefully lead to further improvements for the B_1^+ field.

5.2 Suggestion for Future Work

The mean SNR measurement was compared for each of the four volume coils and multi-transmit coil array; it were strongly dependent on the properties and shape of the subject, orientation, and slice. In this study, the mean values had different values mainly due to the different matrix sizes rather than other factors. For accurate comparison, the matrix size, applied FA, chosen FOV, and other imaging parameters should be identical.

The current research used a 7T MRI system with an eight-driven parallel transmit and 32-channel receiver. To extend the project to a larger scale, the element number has to be evaluated closely for acquiring the human brain in an UHF MRI system. RF coil and circuitry have diverse options, such as various channel excitations, shapes for coil geometry, and number of coil elements, as well as the combination of techniques for receives circuitry.

RF coil and circuitry should be explored for acquiring signal sensitivity, B_1 homogeneity, and B_1^+ homogeneity. As an example, FA acquired from 16-element excitation is a more homogeneous B_1^+ field than that from eight-element or eight-combined excitation. Therefore, in a dedicated eight-driven pTx system, more optimized RF circuitry or another approach has to be considered and evaluated. Also, RF signal combining techniques can be modified with additional combiner circuitry. The output of the RF signal in the coil has another pathway before connection to the preamplifiers. The divided or combined signal by arbitrary factors can be implemented for exploring other results.

Coil dimension as function of imaging depth should also be considered. Increasing the coil element decreases imaging depth but produces a highly efficient parallel imaging performance. It is also accompanied by more strongly mutual inductive coupling. More importantly, a dedicated MRI system with a number of transmit and receive channels must be considered when designing the RF coil and circuitry.

Bibliography

1. Bloembergen N, Purcell EM, Pound RV, "*Relaxation effects in nuclear magnetic resonance absorption*", Phys. Rev., 1948; 73: 679-712.
2. Carr HY, Purcell EM, "*Effects of diffusion on free precession in nuclear magnetic resonance experiments*", Phys. Rev., 1954; 94: 630-638.
3. Bloch F, "*Nuclear induction*", Phys. Rev., 1946; 70: 460-474.
4. Lauterbur PC, "*Imaging formation by induced local iteration: examples employing nuclear magnetic resonance*", Nature, 1973; 242: 190.
5. Mansfield P, Morris PG, "*NMR imaging in biomedicine*", New York: Academic Press, 1982.
6. Damadian R, "*Tumor detection by nuclear magnetic resonance*", Science, 1971; 171: 1151-1153.
7. Damadian R, Zaner K, Hor D, "*Nuclear magnetic resonance as a new tool in cancer research: human tomors by NMR*", Ann. N.Y. Acad. Sci., 1973; 222: 1048-1076.
8. Haake EM, Brown RW, Thompson MR, and Venkatesan R, "*Magnetic resonance imaging: physical principles and sequence design*", 1st ed. Wiley-Liss, 1999.
9. Hoult DI, Richards RE, "*The signal to noise ratio of the nuclear magnetic resonance experiment*", J. Magn. Reson., 1976; 24: 71-85.
10. Abduljalil AM, Robitaille PM, "*Macroscopic susceptibility in ultra high field MRI*", Comput. Assist. Tomogr., 1999; 23:832-841.
11. Abduljalil AM, Kangarlu A, Yu Y, Robitaile P-ML, "*Macroscopic susceptibility in ultra high field MRI-II: acquisition of spin echo images from the human head*", Comput. Assist. Tomogr., 1999; 23: 842-844.
12. Li TQ, van Gelderen P, Merkle H, Talagala L, Koretsky AP, Duyn J, "*Extensive hetrogeneity in white matter intensity in high-resolution T2*-weighted MRI of the human brain at 7.0 T*", Neuroimage, 2006; 32:1032-1040.
13. Roschmann P, "*Radiofrequency penetration and absorption in the human body: limitation to high-field whole-body nuclear magnetic resonance imaging*", Med. Phys., 1987; 14: 922-931.
14. Singerman RW, Denison TJ, Wen H, Balaban RS, "*Simulation of B1 field distribution and intrinsic signal-to-noise in cardiac MRI as a function of static magnetic field*", J. Magn.Reson., 1997; 125:72-83.
15. Hayes CE, Edesltein WA, Schenk JF, Mueller OM, Each ME, "*An efficient, highly*

homogeneous radiofrequency coil for whole body NMR imaging at 1.5T", J. Magn. Reson., 1985; 63: 622-628.

16. Roemer PB, Edelstin WA, Hayes CE, Souza SP, Mueller OM, "*The NMR array*", Magn. Reson. Med., 1990; 16: 192-225.
17. Lin FH, Kwong KK, Huang IJ, Belliveau JW, Wald LL, "*Degenerate mode birdcage volume coil for sensitivity encoded imaging*", Magn. Reson. Med., 2003; 50: 1107-1111.
18. Wald LL, Wiggins GC, Potthast A, Wiggins J, Triantafyllou C, "*Design considerations and coil comparisons for 7 T brain imaging*", Appl. Magn. Reson., 2004; 29: 19-37.
19. Peterson DM, Duensing GR, Caserta J, Fitzsimmons JR, "*An MR transceive phased array designed for spinal cord imaging at 3 tesla: preliminary investigations of spinal cord imaging at 3 T*", Invest. Radiol., 2003; 38: 428-435.
20. Schmitt M, Potthast A, Sosnovik DE, Wiggins GC, Triantafyllou C, Wald LL, "*A 128 channel receive-only cardiac coil for 3T*", Proc. Intl. Soc. Mag. Reson. Med. 15, 2007.
21. Hardy CJ, Giaquinto RO, Piel JE, Rohling KW, Marinelli L, Blezek DJ, Fiveland EW, Darrow RD, Foo TK, "*128-channel body MRI with a flexible high-density receiver-coil array*", J. Magn. Reson. Imgag., 2008; 28: 1219-1225.
22. Wiggins GC, Triantafyllou C, Potthast A, Reykowski A, Mittka M, Wald LL, "*32-channel 3 tesla receive-only phased-array head coil with soccer-ball element geometry*", Magn.Reson. Med., 2006; 56: 216-223.
23. Liu W, Yang QX, Collins CM, Smith MB, "*Numerical evaluation of power radiated and dissipated by a loaded surface coil at high field*", Proc. Intl. Soc. Mag. Reson. Med. 10, 2002.
24. Wiggins GC, Potthast A, Triantafyllou C, Wiggins CJ, Wald LL, "*Eight-channel phased array coil and detunable TEM volume coil for 7 T brain imaging*", Magn. Reson. Med., 2005; 54: 235-240.
25. Cho ZH, Kim YB, Kim KN, Hong SM, "*MRI system rf coil assembly with a birdcage transmit only coil and a pseudo-chain-link receive only coil array*", US 7,733,088 B2. 2010.
26. Lee RF, Westgate CR, Weiss RG, Newman DC, Bottomley PA, "*Planar strip array (PSA) for MRI*", Magn. Reson. Med., 2001; 45: 673-683.
27. Vaughan JT, Garwood M, Collins CM, Liu W, DelaBarre L, Adriany G, Andersen P, Merkle H, Goebel R, Smith MB, Ugurbil K, "*7T vs. 4T: RF power, homogeneity, and signal-to-noise comparison in head images*", Magn. Reson. Med., 2001; 46: 24-30.
28. Alecci M, Collins CM, Wilson J, Liu W, Smith MB, Jezzard P, "*Theoretical and*

experimental evaluation of detached endcaps for 3 T birdcage coils", Magn. Reson. Med., 2003; 49: 363-370.

29. Kang CK, Hong SM, Han JY, Kim KN, Kim SH, Kim YB, Cho ZH, "*Evaluation of MR angiography at 7.0 tesla MRI using birdcage radio frequency coils with end caps*", Magn. Reson. Med., 2008; 60: 330-338.
30. Hiratsuka Y, Miki H, Kikuchi K, Kiriyama I, Mochizuki T, Takahashi S, Sadamoto K, "*Sensitivity of an eight-element phased array coil in 3 tesla MR imaging: a basic analysis*", Magn. Reson. Med., 2007; 6: 177-181.
31. Metcalf M, Xu D, Okuda DT, Carvajal L, Srivivasan R, Kelley DA, Mukherjee P, Nelson SJ, Vigneron DB, Pelletier D, "*High-resolution phased-array MRI of the human brain at 7 tesla: initial experience in muliple sclerosis patients*", J. Neuroimaging, 2010; 20: 141-147.
32. Katscher U, Borner P, Leussler C, Van de Brink J, "*Transmit SENSE*", Magn. Reson. Med., 2003; 49: 144-150.
33. Adriany G, Auerbach EJ, Snyder CJ, Gözübüyük A, Moeller S, Ritter J, Van de Moortele PF, Vaughan T, Ugurbil K, "*A 32-channel lattice transmission line array for parallel transmit and receive MRI at 7 tesla*", Magn. Reson. Med., 2010; 63: 1478-1485.
34. Barfuss H, Fischer H, Hentschel D, Ladebeck R, Oppelt A, Witting R, Duerr W, Oppelt R, "*In vivo magnetic resonance imaging and spectroscopy of humans with a 4 T whole-body magnet*", NMR in Biomed., 1990; 3:31-45.
35. Jin JM, Chen J, Chew WC, Gan H, Magin RL, Dimbylow PJ, "*Computation of electromagnetic fields for high-frequency magnetic resonance imaging applicatinos*", Phys. Med. Biol., 1996; 41: 2719-2738.
36. Alsop DC, Connick TJ, Mizsei G, "*A spiral volume coil for improved RF field homogeneity at high static magnetic field strength*", Magn. Reson. Med., 1998; 40: 49-54.
37. Ginsberg DM, Melchner MJ, "*Optimum geometry of saddle coils for generating a uniform magnetic field*", Rev. Sci. Inst., 1970; 41: 122-123.
38. Alderman DW, Grant DM, "*An efficient decoupler coil design which reduces heating in conductive samples in superconducting spectrometers*", J. Magn. Reson., 1979; 36: 447-451.
39. Sodickson DK, Manning WJ, "*Simultaneous acquisition of spatial harmonics (SMASH): fast imaging with radiofrequency coil arrays*", Magn. Reson. Med., 1997; 38: 591-603.
40. Pruessmann KP, Weiger M, Scheidegger WM, Boesiger P, "*SENSE: sensitivity encoding for fast MRI*", Magn. Reson. Med., 1999; 42: 952-962.

41. Griswold MA, Jakob PM, Heidemann RM, Nittka M, Jellus V, Wang J, Kiefer B, Hasse A, "*Generalized autocalibrating partially parallel acquisitions (GRAPPA)*", Magn. Reson. Med., 2002; 47: 1202-1210.
42. Blaimer M, Breuer F, Mueller M, Heidemann RM, Grisowld MA, Jakob PM, "*SMASH, SENSE, PILS, GRAPPA*", Magn. Reson. Imagaging, 2004; 15: 223-236.
43. Mareyam A, Polimeni JR, Alggappan V, Fischl B, Wald LL, "*A 30 channel receive-only 7T array for ex vivo brain hemisphere imaging*", Proc. Intl. Soc. Mag. Reson. Med. 17, 2009.
44. Keil B, Triantafyllou C, Hamm M, Wald LL, "*Design optimization of a 32-channel head coil at 7T*", Proc. Intl. Soc. Mag. Reson. Med. 18, 2010.
45. Ledden PJ, Mareyam A, Wang S, Gelderen PV, Duyn JH, "*Twenty-four channel receive-only array for brain imaging at 7T*", Proc. Intl. Soc. Mag. Reson. Med. 14, 2006.
46. Zhu Y, "*Parallel excitation with an array of transmit coils*", Magn. Reson. Med., 2004; 51:775-784.
47. Kim KN, Darji N, Herrmann T, Mallow J, Cho ZH, Speck O, Bernarding J, "*Improved B1+ field using 16-channel transmit head array and an 8-channel pTx system at 7T*", Proc. Intl. Soc. Mag. Reson. Med. 19, 2011.
48. Darji N, Kim KN, Patel G, Fautz HP, Bernarding J, Speck O, "*Evaluating further benefits of B1+ homogeneity when more transmit channels are used*", Proc. Intl. Soc. Mag. Reson. Med. 19, 2011.
49. Weisser A, Lanz T, "*A volume head array with 8 transmit / receive channels for 7 T*", Proc. Intl. Soc. Mag. Reson. Med. 14, 2006.
50. Adriany G, Van de Moortele PF, Wiesinger F, Moeller S, Strupp JP, Andersen P, Snyder C, Zhang X, Chen W, Pruessmann KP, Boesinger P, Vaughan T, Ugurbil K, "*Transmit and receive transmission line arrays for 7 tesla parallel imaging*", Magn. Reson. Med., 2005; 53: 434-445.
51. Wu B, Zhang X, Qu P, Shen GX, "*Capacitively decoupled tunable loop microstrip (TLM) array at 7 T*", Magn. Reson. Imagaging, 2007; 25: 418–424.
52. Wu B, Wang C, Kelley D, Xu D, Vigneron DB, Nelson SJ, Zhang X, "*Shielded microstrip array for 7T human MR imaging*", IEEE Trans. Med. Imag., 2010; 29: 179-184.
53. Paska J, Leussler C, "*Hybrid TEM/loop coil aray for parallel high field MRI*", Proc. Intl. Soc. Mag. Reson. Med. 16, 2008.
54. Yazdanbakhsh P, Fester M, Oppelt R, Bitz A, Kraff O, Orzada S, Ladd ME, Solbach K,

"*Variable power combiner for a 7T butler matrix coil array*", Proc. Intl. Soc. Mag. Reson. Med. 17, 2009.

55. Alagappan V, Setsompop K, Nistler J, Potthast A, Schmitt F, Adalsteinsson E, Wald LL, "*A simplified 16-channel butler matrix for parallel excitation with the birdcage modes at 7T*", Proc. Intl. Soc. Mag. Reson. Med. 16, 2008.
56. Alagappan V, Setsompop K, Polimeni R, Potthast A, Zelinski AC, Wiggins GC, Fontius UJ, Schmitt F, Adalsteinsson E, Wald LL, "*Mode compression of transmit and receive arrays for parallel imaging at 7T*", Proc. Intl. Soc. Mag. Reson. Med. 16, 2008.
57. Hoult DI, "*The principle of reciprocity in signal strength calculations: a mathematical guide*", Concepts in Magn. Reson., 2000; 12: 173-187.
58. Liang ZP, Lauterbur PC, "*Principles of magnetic resonance imaging*", IEEE Press New York, 2000; p 59.
59. Ruhr University Bochum, "*Wie funktioniert eine MR-Untersuchung?*", 2010, Available at: http://www.ruhr-uni-bochum.de/neuropsy/methoden/kernspinn/fMRI.html, Accessed March 20, 2010.
60. RWTH Radiology, "*Summary of the imaging process*", 2010, Available at: http://www.rad.rwth-aachen.de/lernprogramm/bild.htm, Accessed April 1, 2010.
61. Ernst RR, Anderson WA, "*Application of Fourier transform spectroscopy to magnetic resonance*", Rev. Sci. Instrum., 1966; 37: 93-102.
62. ReviseMRI.com, "*Questions*", Available at: http://www.revisemri.com/questions/basicphysics/t1contrast, Accessed April 2, 2010.
63. ReviseMRI.com, "*Questions*", Available at: http://www.revisemri.com/questions/basicphysics/t2contrast, Accessed April 2, 2010.
64. Nishimura D, "*Principles of magnetic resonance imaging*", Stanford University. 1996.
65. Hoult DI, Richards RE, "*The signal-to-noise ratio of the nuclear magnetic resonance experiment*", J. Magn. Reson., 1976; 24: 71-85.
66. Maxwell JC, "*A dynamical theory of the electromagnetic field*", Phil. Trans. Roy. Soc London, 1865; 155: 459-512.
67. Pozar DM, "*Microwave engineering*", Third Edition, John Wiley & Sons Inc., ISBN 0-471-44878-8, 2005; p7.
68. Jackson JD, "*Classical Electrodynamics (3rd ed. ed.)*", New York: Wiley. Chapter 5. ISBN 0-13-805326-x.
69. Haacke EM, Brown RW, Thompson MR, Venkatesan R, "*Magnetic resonance imaging: physical principles and sequence design*", John Wiley & Sons, New York,

ISBN 0-471-35128-8, 1999; p828.

70. Physical Hawaii educational handbook, "*Polarization*", Available at: http://www.phys.hawaii.edu/~anita/new/papers/militaryHandbook/polariza.pdf, Accessed April 2, 2010.
71. Chen CN, Hoult DI, Sank VJ, "*Quadrature detection coils - a further sqrt(2) improvement in sensitivity*", J. Magn. Reson., 1983; 54: 324-327.
72. Sank VJ, Chen CN, Hoult DI, "*A quadrature coil for the adult human head*", J. Magn. Reson., 1986; 69: 236-242.
73. Doty FD, Gntzminger G, Kulkarni J, Pamarthy K, Staab JP, "*RF coil technology for small-animal MRI*", NMR in Biomed., 2007; 20: 304-325.
74. Cho ZH, YI JH, "*Planar surface gradient coil*", Concepts in Magn. Reson., 1995; 7: 95-114.
75. Mispelter J, Lupu M, Briguet A, "*NMR probeheads for biophysical and biomedical experiments: Theoretical principles & practical guidelines*", Imperial College, London, 2006.
76. Darzinski BJ, Li S, Collins CM, Williams GD, Smith MB, "*A birdcage coil tuned by RF shielding for application at 9.4T*", J. Magn. Reson., 1998; 131: 32-38.
77. Vaughan JT, Hetherington HP, Otu JO, Pan JW, Pohost GM, "*High frequency volume coils for clinical NMR imaging and spectroscopy*", Magn. Reson. Med., 1994; 32: 206-218.
78. Wald LL, Garvajal L, Moyher SE, Nelson SJ, Grant PE, Barkovich AJ, Vigneron DB, "*Phased array detectors and an automated intensity correction algorithm for high-resolution MR imaging of teh human brain*", Magn. Reson. Med., 1995; 34: 433-439.
79. Edelstein WA, Glover GH, Hardy CJ, Redington RW, "*The intrinsic signal-to-noise ratio in NMR imaging*", Magn. Reson. Med., 1986; 3: 604-618.
80. Celik H, Eryaman Y, Altmtas A, Abdel-Hafez IA, Atalar E, "*Evaluation of intrinsic MRI coils using ultimate intrinsic SNR*", Magn. Reson. Med., 2004; 52: 640-649.
81. Gruetter R, Weisdorf SA, Rajanayangan V, Terpstra M, Merkle H, Truwit CL, Garwood M, Nyberg SL, Ugurbil K, "*Resolution improvements in in vivo 1H NMR spectra with increased magnetic field strength*", J. Magn. Reson., 1998; 135: 260-264.
82. Johnson CC, Guy AW, "*Nonionizing electromagnetic wave effects in biological materials and systems*", Proceeding of the IEEE, 1972; 60: 692-718.
83. Kim HS, Kim YS, Cho ZH, Hilal SK, "*Phase delay and attenuation corrections in Fourier transform NMR tomographic imaging*", IEEE Nuclear Science, 1981; 28: 142-

147.

84. Yang QX, Wang J, Zhang X, Collins CM, Smith MB, Liu H, Zhu XH, Vaughan JT, Ugrubil K, Chen W, "*Analysis of wave behavior in lossy dielectric samples at high field*", Magn. Reson. Med., 2002; 47: 982-989.
85. Collins CM, Liu W, Schreiber W, Yang QX, Smith MB, "*Central brightening due to constructive interference with, without, and despite dielectric resonance*", J. Magn. Reson. Imaging, 2005; 21:192-196.
86. Kim KN, Hong SM, Han JY, Yoon HW, Chung JY, Kim JH, Cho ZH, "*Experiments and Quantification of lumped elements volume coil for B_1^+ excitation at 7T*", Proc. Intl. Soc. Mag. Reson. Med. 17, 2009.
87. Wang C, Shen GX, "*B1 field, SAR, and SNR comparisons for birdcage, TEM, and micro strip coils at 7T*", J. Magn. Reson. Imaging, 2006; 24: 439-443.
88. Cho ZH, Kim YB, Kim KN, Hong SM, "*Magnetic resonance imaging system*", US patent 7,7746,073 B2, 2010
89. NEMA standards publication MS-2001
90. McRobbie, DW, Moore EA, Graves MJ, Prince MR, "*MRI-from picture to proton*", Cambridge University Press, 2003, pp205.
91. Hornak JP, Szumowski J, "*Magnetic field mapping*", Magn. Reson. Med., 1988; 6: 158-163.
92. Wang J, Qiu M, Yang QX, Smith MB, Constable RT, "*Measurement and correction of transmitter and receiver induced nonuniformities in vivo*", Magn. Reson. Med., 2005; 53: 408-417.
93. Akoka S, Frankoni F, Seguin F, Pape AL, "*Radiofrequency map of an NMR coil by imaging*", Magn. Reson. Imaging, 1993; 11: 437-441.
94. Cunningham CH, Pauly JM, Nayak KS, "*Saturated double-angle method for rapid B1+ mapping*", Magn. Reson. Med., 2006; 55: 1326-1333.
95. Franconi F, Sonier CB, Seguin F, Pape AL, Akoka S, "*Acquisition of spin echo and stimulated echo by a single sequence: application to MRI of diffusion*", Magn. Reson. Imaging, 1994; 12: 605-611.
96. Mekle R, Zwaag W.van der, Joosten A, Gruetter R, "*Comparison of three commercially available radio frequency coils for human brain imaging at 3 Tesla*", Magn. Reson. Mater. Phys. Biol. Med., 2008; 21: 53-61.
97. Hardy CJ, Darrow RD, Saranathan M, Giaquinto RO, Zhu Y, Dumoulin CL, Bottomley PA, "*Large field-of-view real-time MRI with a 32-channel system*", Magn. Reson. Med.,

2004; 52: 878-884.

98. Hardy CJ, Giaquinto RO, Piel JE, Rohling KW, Marinelli L, Blezek DJ, Fiveland EW, Darrow RD, Foo TK, "*128-channel body MRI with a flexible high-density receiver-coil array*", J. Magn. Reson. Imaging, 2008; 28: 1219-1225.
99. King SB, Duensing R, Peterson D, Varosi S, Molyneaux DA, "*A comparison of 1, 4 and 8 channel phased array head coils at 1.5T*", Proc. Intl. Soc. Mag. Reson. Med. 9, 2001.
100. Wald LL, Carvajal L, Moyher SE, Nelson SJ, Grant E, Barkovich AJ, Vigneron DB, "*Phased array detectors and an automated intensity correction algorithm for high-resolution MR imaging of the human brain*", Magn. Reson. Med.," 1995; 34: 433-439.
101. Bottomley PA, Lugo Olivieri CH, Giaquinto R, "*What is the optimum phased array coil design for cardiac and torso magnetic resonance?*", Magn. Reson. Med., 1997; 37: 591-599.
102. King SB, Varosi S, Molyneaux DA, Duensing GR, "*The effects of ultra low input impedance preamplifiers on phased array coil design*", Proc. Intl. Soc. Mag. Reson. Med. 10, 2002.
103. Guclu CC, Boskamp Ed, Zheng T, Becerra R, Blawat L, "*A method for preamplfier-decoupling improvement in quadrature phased-array coils*", J. Magn. Reson. Imaging, 2004; 19: 255-258.
104. Chang G, Friedrich KM, Wang L, Vieira RL, Schweitzer ME, Recht MP, Wigging GC, Regatte RR, "*MRI of the wrist at 7 tesla using an eight-channel array coil combined with parallel imaging: preliminary results*", J. Magn. Reson. Imaging, 2010; 31: 740-746.
105. Rengle A, Armenean M, Bolbos R, Goebel JC, Pinzano-Watrin A, Saint-Jalmes H, Gillet P, Beuf O, "*A dedicated two-element phased array receiver coil for high resolution MRI of rat knee cartilage at 7T*", International Conference of the IEEE Engineering in Medicine & Biology Society, 2009; 56: 2891-2897.
106. Staewen RS, Johnson AJ, Ross BD. Parrish T, Merkle H, Garwood M, "*3D flash imaging using a single surface coil and a new adiabatic pulse*", Investigative Radiololgy, 1990; 25: 559-567.
107. Cohen MS, DuBois RM, Zeineh MM, "*Rapid and effective correction of RF inhomogeneity for high field magnetic resonance imaging*", Human Brain Mapping, 2000; 10: 204-211.
108. Yang C, Deng W, Alagappan V, Wald LL, Stenger VA, "*Four-dimensional spectral-spatial RF pulses for simultaneous correction of B1+ inhomogeneity and susceptibility artifacts in T2*-weighted MRI*", Magn. Reson. Med., 2010; 64: 1-8.

109. Clare S, Alecci M, Jezzard P, "*Compensating for B1 inhomogeneity using active transmit power modulation*", Magn. Reson. Imaging, 2001; 19: 1349-1352.
110. Adriany G, Van de Moortele PF, Ritter J, Moeller S, Auerbach EJ, Akgun C, Snyder CJ, Vaughan T, Ugurbil K, "*A geometrically adjustable 16-channel transmit/receive transmission line array for improved RF efficiency and parallel imaging performance at 7 tesla*", Magn. Reson. Med., 2008; 59: 590-597.
111. Katscher U, Bornert P, "*Parallel RF transmission in MRI*", NMR in Biomed., 2006; 19: 393-400.
112. Graesslin I, Falaggis K, Biederer S, Glaesel D, Vernickel P, Roeschmann P, Leussler C, Thran A, Zhail Z, Morich M, Katscher U, "*SAR simulations and experiments for parallel transmission*", Proc. Intl. Soc. Mag. Reson. Med. 15, 2007.
113. Metzger GJ, Snyder C, Akgun C, Vaughan T, Ugurbil K, Van de Moortele PF, "*Local B1+ shimming for prostate imaging with transceiver arrays at 7T based on subject-dependent transmit phase measurements*", Magn. Reson. Med., 2008; 59: 396-409.
114. Gilbert KM, Curtis AT, Gati JS, Klassen LM, Menon RS, "*A radiofrequency coil to facilitate B1+ shimming and parallel imaging acceleration in three dimensions at 7 T*", NMR in Biomed., 2010.
115. Setsompop K, Alagappan V, Zelinski AC, Potthast A, Fontius U, Hebrank F, Schmitt F, Wald LL, Adalsteinsson E, "*High-flip-angle slice-selective parallel RF transmission with 8 channels at 7 T*", J. Magn. Reson., 2008; 195: 76-84.
116. Yazdanbakhsh P, Solbach K, "*Microstrip butler matrix design and realization for 7 T MRI*", Magn. Reson. Med., 2011; 66:270-280.
117. In MGH, Martinos Center, Retrieved from http://maki.bme.ntu.edu.tw/tool_b1.html.
118. In CST MWS (Darmstadt, Germany), Retrived from http://www.cst.com/Content/Applications/Article/165.
119. Kozlov M, Turner R, "*A comparison of Ansoft HFSS and CST microwave studio simulation software for multi-channel coil design and SAR estimation at 7 T MRI*", PIERS ONLINE, 2010; 6: 4.
120. Wang J, Yang QX, Zhang X, Collins CM, Smith MB, Zhu XH, Adriany G, Ugurbil K, Chen W, "*Polarization of the RF field in a human head at high field: A study with a quadrature surface coil at 7.0 T*", Magn. Reson. Med., 2002; 48: 362-369.
121. ReviseMRI.com, "*Questions*", Available at: http://www.revisemri.com/questions/safety/sar, Accessed April 2, 2010.
122. In CST MWS, SAR limitation, Retrieved from http://www.cst.com/Content/Documents/

Events/UGM2007/05-Wittig.pdf.

123. In Directional Couplers. Retrieved from http://www.download-it.org/free_files/filePages from Chapter 7. Directional Couplers.pdf.
124. In Mobile Devdesign. Retrieved from http://mobiledevdesign.com/tutorials/radio_ designing_lc_wilkinson/.
125. Dole C.W, "*Coaxial cable insertion phase measurement and analysis*", Product Engineer. Belden Electronics Division, Richmond, Indiana.
126. Yarnykh VL, "*Actual flip-angle imaging in the pulsed steady state: A method for rapid three-dimensional mapping of the transmitted radiofrequency field*", Magn. Reson. Med., 2007; 57: 192-200.
127. Vaughan JT, Snyder CJ, DelaBarre LJ, Bolan PJ, Tian J, Bolinger L, Adriany G, Andersen P, Strupp J, Ugurbil K, "*7 T Whole body imaging: Preliminary Results*", Magn. Reson. Med., 2009; 61: 244-248.
128. Liang ZP, Lauterbur PC, "*Principles of magnetic resonance imaging: A signal processing perspective*", Wiley-IEEE Press. 2000.
129. DeMeester GD, Zhai Z, Morich MA, Leussler C, ,Findeklee C, "*Numerical comparison between TEM head coil and birdcage head coil at 7T*", Proc. Intl. Soc. Mag. Reson. Med. 11, 2004.
130. Akoka S, Franconi F, Seguin F, Lepape A, "*Radiofrequency map of an NMR coil by imaging*", Magn. Reson. Imaging, 1993; 11: 437-441.
131. Hasse A, "*Snapshot FLASH MRI. Applications to T1, T2, and chemical-shift imaging*", Magn. Reson. Med., 1990; 13: 77-89.
132. Liu W, Zhang S, Collins CM, Wang J, Smith MB, "*Comparison of four different shields of birdcage-type coils with experiments and numerical calculations*", Concepts in Magn. Reson., 2006; 29: 176-184.
133. Wiggins GC, Mareyam A, Setsompop K, Alagappan V, Potthast A, Wald LL, "*A close-fitting 7 tesla 8 channel transmit/receive helmet array with dodecahedral symmetry and B1 variation along Z*", Proc. Intl. Soc. Mag. Reson. Med. 16, 2008.
134. Alagappan V, Setsompop K, Fontius U, Schmitt F, Adalsteinsson E, Wald LL, "*A concentrically shielded transceive array coil optimized for B1+ inhomogeneity correction at 7T*", Proc. Intl. Soc. Mag. Reson. Med. 17, 2009.